Lead-free metal halide (halogenidometallate) semiconductors for optoelectronic applications

Biplab Ghosh[1, a], Darrell Jun Jie Tay[2,3], Maarten B. J. Roeffaers[1], Nripan Mathews[2,4, b]

Affiliations

[1] cMACS, Department of Microbial and Molecular Systems, KU Leuven, Leuven, 3001 Belgium

[2] School of Materials Science and Engineering, Nanyang Technological University, Singapore 639798, Singapore

[3] Interdisciplinary Graduate Programme (IGP), Graduate College, Nanyang Technological University, Singapore 637460, Singapore

[4] Energy Research Institute @ NTU, Nanyang Technological University, Research Techno Plaza, 50 Nanyang Drive, Singapore 637553, Singapore

Author to whom correspondence should be addressed:

[a] biplab@nus.edu.sg

[b] nripan@ntu.edu.sg

Abstract

The electronic age demands the development of high-performing thin-film semiconductors that are low-cost and scalable. Lead (Pb)-based halide perovskites (LHPs) have proven to be successful in this regard, but their use is limited by environmental and health concerns related to lead toxicity. Lead-free halide compounds offer a promising alternative, with vast compositional space for fine-tuning properties to meet specific application requirements. These materials also offer opportunities for the deliberate introduction of functional properties, providing unparalleled control over their targeted applications.

While the call for lead-free halide materials as alternatives to LHPs is echoed several times, the performance of these compounds remains modest as compared to the exponential growth of LHPs. Nevertheless, the compositional space of lead-free halide

materials is huge, even bigger than LHPs as they are not restricted by the structural constrains of perovskite structure. This brings their huge potential in future technologies which are remains untapped as of now. As a meta-analysis, we compare and combine the findings of previously published studies, to assess the optoelectronic properties of ternary and quaternary halide materials and their applications in devices. It details the structures of the various lead-free halide materials including perovskites, perovskite-derivative, and non-perovskites structures and describes the role of dimensionality and composition on their optoelectronic properties. To end, the challenges and perspectives of lead-free materials and devices are given. We hope this review will provide new insights for designing metal halide materials from the viewpoint of the modulation of the basic building blocks metal halide coordination. The future of electronics lies in the hands of lead-free halide materials, and we hope this review will inspire further research in this field.

Table of Contents

1 INTRODUCTION

Metal halide semiconductors, in general, have experienced a meteoric rise in recent years due to the exceptional semiconducting properties of lead-based halide perovskites (LHPs), which offer unprecedented tunability of optoelectronic properties simply through elemental substitution and structural malleability. Contrary to prototypical elemental semiconductors such as Si and Ge, or compound semiconductors including GaAs, GaP, and GaN, heavier halide-based semiconductors are expected to take a dominant position in future, offering promise of high-performance and low-cost optoelectronic devices due to the ease of high-quality bulk crystals fabrication and thin-film growth techniques that do not require expensive equipment. These advantages have fuelled their widespread adaptation in various optoelectronic devices including but not limited to photovoltaics, light emitting diodes (LEDs), transistors, memristors, and other photonic devices.

While the recent sharp rise of halide-based semiconductors is due to the emergence of Pb-based halide perovskites (LHPs), halide-based semiconductors have been well-known since the last century and played an important role in materials chemistry, especially organometallics and coordination complexes[1-4]. Later, the development flourished further in the late 80s, driven by their rich structural diversity and phase transformations between ferroelectric, ferrielectric and ferroelastic phases[5-8]. During this time, a plethora of organo-halides were introduced within metal halide network to establish one of its most interesting features, - the polyanionic structure of metal halide tetrahedra/octahedra which is formed via connection by corners, edges, or faces. These polyanionic structures were found to be most influential in determining final optoelectronic properties of the compounds. For example, the alkylammonium halogenantimonates and bismuthates were shown to crystallize in different stoichiometries determined by the anionic sublattice that behave either as natural quantum-dots, -wires, or -wells. Unfortunately, the optoelectronic properties of these materials were mostly overshadowed by the uniqueness of their crystal structures which comprise electrostatic, covalent, and hydrogen-bonding and, most of the earlier studies were limited to

the crystal structure, phase transitions, nonlinear optical properties, and spectroscopic characterizations[9, 10]. Except for a few mentions of their photoluminescence properties (such as halide compounds based on mercury-like cations) in solutions, semiconducting and optoelectronic properties remained largely unnoticed.

The recent re-emergence of halide-based semiconductors took place after the development of thin-film semiconductor device architectures in the early 1990s along with the massive breakthrough in LHPs in the last decade. While the performance of LHP-based optoelectronic devices has improved dramatically over the past decade[11, 12], the easy-to-fabricate LHPs also face the grandest challenge in commercialization as they easily degrade, and due to the inherent toxicity associated with water soluble Pb^{2+} cations. Lead (Pb^{2+}) is one of the few toxic chemicals known to have no safe threshold of exposure and it affects nearly all organs in the human body, resulting in stringent environmental regulations in most of countries[13]. Extensive investigations have reported the calamitous effect of only a few micrograms of Pb accumulating in the human body, especially in children[14]. Even in the last century, leaded gasoline was heavily advocated by the automotive industry, which resulted in widespread lead poisoning. While lead in LHPs is less dangerous as compared to tetraethyl lead (major component of leaded gasoline) due to the volatile nature of the latter, public perception of lead-based compounds remains negative. These concerns have forced researchers to search for alternative non-toxic halide compounds with similar chemical and optoelectronic properties. As the electronic structure dictates the optoelectronic properties of a semiconductor, mimicking the electronic structure of LHPs seems to be the most logical step for the development of Pb-free halide compounds. Theoretical calculations revealed that the uniqueness of the electronic structure of LHPs mainly arises from a hybridization of ns^2 electrons from heavy metals and np^6 electrons from the heavier halides. Unfortunately, homovalent substitution of Pb^{2+} with the same group of elements (Sn^{2+} and Ge^{2+}) resulted in a different kind of challenge as Sn- and Ge-based halide perovskites were found to be even more unstable when compared to LHPs.

As such, the chemical space and crystal structures were further explored with heterovalent substitution (such as Bi^{3+} and Sb^{3+}) that are not strictly confined to the perovskite crystal structure. The application of these strategies have revealed the inimitable importance of corner-shared octahedral networks in tuning optoelectronic properties. For example, the electronic structures of Bi-based and Pb-based ternary halides differ widely despite having isoelectronic structures in their excited states. Consequently, the optoelectronic properties of Pb-based and Bi-based ternary halides differ massively. The role of crystal structure became increasingly important thereafter. As far as electronic properties are concerned, corner-sharing of the metal octahedra seems to be essential for producing direct-band-gap semiconductors, which are the most desirable for optoelectronic applications. The corner-sharing architecture promotes destabilization of the ns^2 lone pair in the B^{2+} sites, leading to a very dispersive valence and conduction bands and high mobility of the charge carriers. On the other hand, the octahedral network in edge- or face-sharing configurations lead to flat electronic bands and wide band gaps, as the lone pair is lowered in energy. Unfortunately, successive investigations have shown that even corner-shared octahedral networks may not be a sufficient condition for generating direct bandgap in semiconductors. For example, one of the most famous double perovskites, $Cs_2AgBiBr_6$ possess an indirect bandgap despite having nearly ideal perovskite crystal structure. Furthermore, inspired by the LHPs, a wide variety of halide compounds having different crystal structures have been (re-)discovered with some unique optoelectronic properties which were not known earlier. These halide compounds can be easily fabricated from low-cost precursor solutions, a feature that makes LHPs so popular. These halide compounds, which started their journey as lead-free photovoltaic absorber materials, currently find use in numerous other applications such as light-emitting diodes, photodetectors, sensors, and radiation detectors, as well as in more emerging fields such as lasing and neuromorphic computation. Many physical/optoelectronic properties of these compounds can be further modulated by doping, alloying, and exposure to external forces such as moisture and pressure, which further widens their application area.

This review seeks to examine recent developments and new structural concepts in lead-free halide compounds or halogenidometallates. In contrast to current literature which sometimes classifies non-related structures as perovskites, we intend to provide a universal classification for the class of compounds as octahedrally coordinated perovskite (exclusively corner-shared), perovskite-derivative (perovskite-related structure) compounds, and non-perovskite structures (discussed later). We first systematize the crystal structures of these lead-free halide compounds, covering both perovskite and non-perovskite halide compounds. We then discuss how the crystal structures of such compounds impact the optoelectronic properties. Later, we review recent advances in the emerging field of these lead-free optoelectronic devices, outlining their challenges, prospects, and strategies to further boost performance. As one overarching goal for the broader structural family, we highlight the idea of a specialized material system having greater/comparable functionality than/with LHPs for specific applications rather than one-system-for-all. We envision that many of these materials will hold promise for a variety of optoelectronic applications, including micro- and nanoelectronics, conversion of solar energy into electrical or chemical, light and radiation detection, and more. While a huge materials space exists for the lead-free system, we have only focused on ternary and quaternary compounds, containing heavier halides (Cl, Br, and I), owing to their similar chemical characteristics and ease of processability. The review is arranged by topological criteria: the introduction is followed by the classification of different compounds into perovskite, perovskite-derivative and non-perovskite structures, which are subdivided according to the connectivity of the building blocks involved (dimensionality). Each section is devoted to a description of their crystal structure and optoelectronic properties related to the unique crystal structures.

2 CLASSIFICATION OF HALIDE COMPOUNDS

At this point, we must set the rules to categorize perovskite, perovskite-derivative (perovskite related), and perovskite-inspired non-perovskite compounds. Owing to polytypism of perovskite crystal structure and the discovery of many variants, we note that the definition of

perovskite structure has been somewhat diluted from the original definition of aristotype $SrTiO_3$ (space group $Pm\bar{3}m$). Consequently, a wide variety of nomenclature has been used to describe the structures such as hexagonal polytypes[15], zero-dimensional or dot perovskite, face-sharing or edge sharing polytypes, perovskitoids[16], zigzag[17], quasi-dimensional perovskite[18] etc. In this review, we use the term "perovskite" exclusively for the compounds showing corner (vertex)-sharing octahedral networks in at least one direction. All other structures which show face-sharing, or edge-sharing or mixed octahedral networks are grouped as perovskite-derivative compounds. This is illustrated in **Figure 1**. We argue that without the corner-shared octahedral network, the stacking of metal octahedral layers cannot form the idealized ABX_3 perovskite structure. On the other hand, corner-shared chains or planes preserve fragments of the perovskite structure and with increasing numbers of layers, corner-shared octahedral networks become stepwise thicker until the endpoint ABX_3 structure is reached. We have also restricted isolated octahedral structures (0D) under perovskite structures as they can also be considered octahedra deficient (defect-assisted) structures. It is a side effect of this classification as the borders are still fuzzy. Due to their close resemblance of the face-shared and edge-shared octahedral networks to the perovskite structures with composition and local coordination, we classify them as perovskite-derivative compounds. Apart from these structures, there are several interesting metal halide compounds having non-perovskite structure (either tetrahedral networks or having totally different stoichiometric compositions) which have risen in prominence recently. We group them together into non-perovskite compounds. This simple classification allows us to subdivide them into different subgroups for the analysis of the influence of various inorganic lattice conformations on their optoelectronic properties such as bandgaps. Additionally, the corner-shared octahedral network corresponds to the maximum number of degrees of freedom for various distortions and makes it possible to directly correlate with the optoelectronic properties. Below, we discuss the structural and electronic characteristics of these classes of compounds and explain the origin of their optoelectronic differences.

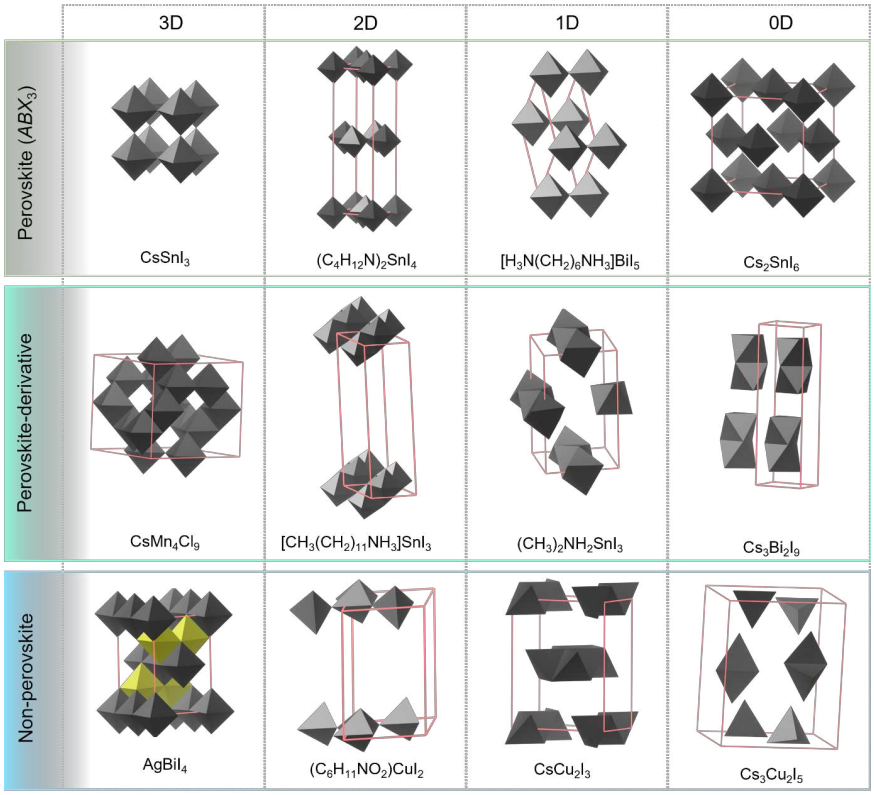

Figure 1: *Polyhedral representation of perovskite, perovskite-derivative, and non-perovskite crystal structure as discussed in the text. Across the row, the degree of octahedral/tetrahedral connectivity decreases. (A-site/Organic cations are omitted, only the polyhedral models are shown for clarity. Unit cells are denoted as red boxes.)*

Dimensionality and description of structure: The idealized halide perovskite structure can be represented by the general formula ABX_3, where *A* and *B* are monovalent and divalent cations respectively, and *X* are the halide anions. In LHPs, the divalent cation is Pb^{2+}. From the atomic packing, the perovskite structure can be described as a closed-packed lattice structure formed by the monovalent cations and halide anions with divalent cations occupying the octahedral voids. In other words, the divalent metal halide octahedra form a three-dimensional network

and the monovalent cations occupy the twelve-fold cavities formed between the $[PbX_6]^{4-}$ polyhedral network. Without a doubt, the optoelectronic properties of LHPs are exceptional with unique defect tolerant properties, i.e., defects are either difficult to form or they have no active role in worsening the optoelectronic properties. The origin of these exceptional properties in LHPs can be summarized by two unique structural characteristics: (1) the corner-shared octahedral network which is responsible for dispersive valence band maxima (VBM) and conduction band minima (CBM)[19], and (2) the presence of antibonding VBM which is associated with defect tolerant behaviour[20, 21]. While the former is governed by the tolerance factor, the latter originates from the electronic properties of the constituent ions and their hybridization chemistry. From the periodic table of elements, only heavy elements in groups 13, 14, and 15 possess the ns^2 electron in their monovalent, divalent, and trivalent oxidation states respectively. As for the first criterion of perovskite structure formation, the *B*-site cation must be able to form octahedral building blocks (6-coordination) with halides. **Figure 2** illustrates the range of the cation radii which are known to form octahedral coordination and tetrahedral coordination with heavier halides (Cl, Br, I). Tolerance factor, or more specifically the Goldschimdt's tolerance factor (*t*)[22], assesses whether an *A*-site cation can fit within $[BX_6]^{4-}$ octahedral voids and indicates the formability of perovskite crystal structures based on the ionic radii of the constituent elements and is given by the following empirical equation:

$$t = \frac{r_A + r_X}{\sqrt{2}(r_B + r_X)} \quad \text{..... Eq. 1}$$

Where, r_i denotes the ionic radius of i ion. Thus, to form a stable 3D perovskite structure, the *t* should be within a specified range (0.8-1.1)[22, 23]. For the case of LHPs, only a few *A*-site cations (such as Cs^+, $CH_3NH_3^+$ (methylammonium, MA), $CH_6N_2^+$ (Formamidinium, FA)) can occupy the cavity between $[PbX_6]^{4-}$ polyhedral network due to size restrictions defined by the tolerance factor. For a smaller *A*-site cation (t < 0.8), the stoichiometric composition crystallizes into a perovskite-derivative structure (e.g., $RbPbI_3$), while a large *A*-site cation (t > 1.1) usually breaks the polyhedral network to form a low-dimensional variant of the perovskite structure (*e.g.*, phenylethyl ammonium lead iodide). Further increases in the radius of the *A*-

site cation drastically change the corner-sharing perovskite structure to a low-dimensional hexagonal structure involving edge- and face-sharing octahedra.

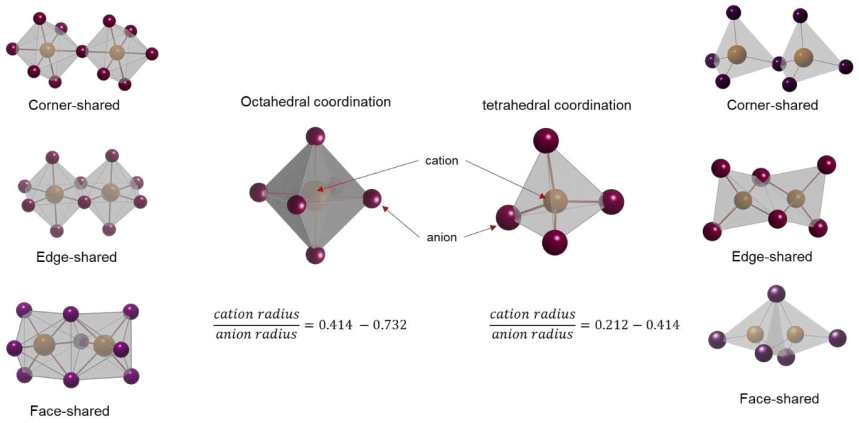

***Figure 2**. Octahedral and tetrahedral coordination in metal-halide compounds. Both octahedral and tetrahedral coordination can form an infinite network via sharing corner, face, or edge (left side and right side of the panel, respectively). The central panel illustrate the range of cation-to-anion radius ratio for octahedral and tetrahedral coordination, considering rigid sphere model.*

In addition, all of these structures can also be classified based on the dimensionality of the crystal structure, i.e., degree of connectivity across 3D space. In contrast to the "dimensionality" of nano-structured materials - such as quantum dots which are physically confined in space - crystal structure dimensionality refers to dielectric confinement within a three-dimensional single lattice. The concept of crystal structure dimensionality was developed by Kitaigorodskii for describing packing density in organic crystals[24]. He defined molecular crystals as the groups of atoms in which the interatomic distance within the group is significantly shorter than the interatomic distance to an atom of a different group. While the concept is based on geometry, it can also be extended to define the dimensionality based on the bonding environment. One may refer to an excellent review by Tulsky and Long [25] on the

crystal structure dimensionality. For halide compounds, the dimensionality can be visualized based on the degree of connectivity between metal-halide octahedral or tetrahedral network which are predominantly covalent bonding. Other weaker interactions such as ionic or hydrogen bonding can be considered non-bonding entities. This is illustrated in **Figure 1** for describing perovskite, perovskite-derivative, and non-perovskite compounds. For example, in $CsSnI_3$ structure, Cs^+ cations fit well within the voids between $[SnI_6]^{4-}$ octahedral network which are connected in all three directions. We can state accordingly that the dimensionality of $CsSnI_3$ extends across all three dimensions. In the case of butylammonium tin iodide ($[CH_3(CH_2)_3NH_3]_2SnI_4$), octahedral voids cannot accommodate large butylammonium cations, resulting in large separation of $[SnI_6]^{4-}$ octahedral network along (001) direction. While butylammonium cations still fill the voids and are connected via hydrogen bonding, this results in large dielectric differences between the organic layer and the inorganic network. Accordingly, we call this structure as 2D crystal structure, extended only in the *a* and *b* crystallographic direction. Furthermore, by changing the organic cation to dimethylammonium, we can obtain 1D chain network of $[SnI_6]^{4-}$ octahedra. The 1D structure can be face-shared, edge-shared, corner-shared, or a combination of both of those[26]. Zero-dimensional structure forms when the octahedra/tetrahedra are not connected to each other anymore, as in the case of Cs_2SnI_6. This connection mode of the inorganic octahedra heavily influences the orbital overlap between metals and halogens, thus affecting their optoelectronic properties. For example, bandgaps of halide perovskites of same composition usually follow face-sharing>edge-sharing>corner-sharing structure.

Pb-free halide compounds (ternary and above) span a broad range of compositions, crystal structures, and stoichiometries, yielding a commensurate breadth of properties. This compositional and structural diversity can be traced to the unique chemical characteristics of metal halide coordination. In the following section, we present the design rules and structure-property relationship of these lead-free halide compounds. We begin with perovskite structure, followed by perovskite-derived and non-perovskite halide compounds.

3 PEROVSKITE STRUCTURE

The crystal structure of halide perovskites which are exclusively corner-shared in our discussion, can be further classified as 3D, 2D, 1D, and 0D structures based on the degree of octahedral connectivity (Figure 1). When the octahedral networks are connected in all three directions, a 3D structure is formed, whereas in the 2D structure, the network of one or multiple inorganic metal halide octahedra layers propagate only in two directions, being sandwiched between the large organic molecules/inorganic cations in other direction. In 1D structures, the octahedral units are connected to each other only in one-direction, thus mimicking the nanowire or nanorod structure within the crystal lattice. Similar analogies can be drawn for the perovskite-derivative and non-perovskite structures as well. Furthermore, the low-dimensional structures can be envisioned as composite materials, formed by periodic stacking of inorganic metal halide layers and large *A*-site cations, having contrasting properties. For example, inorganic layers are associated with excellent charge transport and generation of free carriers, whereas the organic layers reduce the charge transport across the dimension and induce Coulombically bound electron-hole pairs. However, the low-dimensional structures have fewer geometric restrictions, consequently a huge number of low-dimensional structures can be conceived by employing different organic cations, many of which have already been synthesized. Interested readers may refer to these excellent review articles by Mao and co-workers[27], as well as by Pitaro and co-workers[28] on low-dimensional structures for structural description[27-29]. In the following sections, we explore the tunability of the structure-property relationships in various perovskite structures.

3.1 3D perovskite structure

The formability of the 3D perovskite structure (ABX_3) with different divalent cations (B^{2+}) can be empirically predicted based on the octahedral and Goldschimdt's tolerance factor. Kieslich et al[30] calculated the tolerance factors for 21 divalent cations with 13 protonated amines (as *A*-site cation) and 8 anionic species and found only 180 compositions with heavier halides, exhibit a tolerance factor between 0.8 to 1, the range which defines the formability of halide perovskites. However, the most promising candidates to replace Pb were found to be from

group 14 elements (i.e. tin and germanium)[31] which is expected considering similar electronic structures. Similar conclusions have also been reached by other independent research groups, from both theoretical calculations and experimental studies[32]. Consequently, homovalent substitution of Pb^{2+} with Sn^{2+} received the most attention till now, and we therefore devote a considerable portion of this review to illustrate their unique optoelectronic properties.

3.1.1 Sn-based halide perovskite:

Having comparable ionic radii (Pb^{2+}: 1.19 Å, Sn^{2+}: 1.15 Å), the structural variability in Sn-based halide perovskites (THPs) are nearly identical to LHPs. In their purest form, only FA^+, MA^+, and Cs^+ cations have been experimentally demonstrated to form 3D perovskite structures, whereas the possibility of multiple *A*-site cations as dopant/alloy to form 3D structure remains limitless (bound by tolerance factor). The tolerance factor also predicts stable perovskite structure for $RbSnX_3$, however $RbSnI_3$ (or $RbPbI_3$) is known to crystallize into face-shared 1D perovskite-derivative structure[33] (**Figure 3a**). THPs usually demonstrate highly symmetric cubic crystal structure at high temperatures and gradually lose their symmetry with reduced temperature to crystallize into tetragonal and orthorhombic structures (**Figure 3b**). These phase transition temperatures depends on the exact chemical compositions such as all inorganic compositions ($CsSnX_3$) usually show higher transition temperature as compared to the organic inorganic hybrid compositions [34, 35]. This is illustrated in **Figure 3b**. It is worth to point out that the exact phase transition temperature of $FASnI_3$ remain elusive and experimental data often show conflicting results. Most notably, Schueller et al observed an orthorhombic *Pnma* structure below 150 K which is not observed by other studies[36, 37]. Even the room temperature phase of $FASnI_3$ has been reported with different symmetry, notably tetragonal (*P*4/*mbm*)[37], orthorhombic (*Amm*2)[38], and pseudocubic (*C*2*mm*)[36]. These contrasting results most likely arose due to processing history as the phase stability of different

polymorphs of halide perovskites is known to vary depending on the ambient environment and sample morphology (thin-film vs single crystal vs powders)[35].

The wide range of crystallographic variations also leads to notable optoelectronic properties differences. Interestingly, the bandgap of $FASnI_3$ single crystal was found to decrease from 1.38 eV (280 K) to 1.12 eV (4.3 K) upon cooling which is counterintuitive[36]. In conventional semiconductors (such as GaAs or Si), the bandgap decreases with increasing temperature because of the thermal broadening of the bands. In Sn-based halide perovskites, this has been attributed to the dynamic off-centering of Sn^{2+} cation within the structure which reduces the overall symmetry[36] and carrier phonon coupling[37]. This role of symmetry is further illustrated in **Figure 3c** with bonding environment. The VBM, exhibiting high covalency, is formed by antibonding contributions from Sn $5s^2$ and *X mp* orbitals, whereas the CBM, is characterized by an antibonding combination, but has mostly ionic character with major contributions from Sn 5*p* orbitals. Lowering temperatures reduces symmetry, which consequently reduces the overlap between the orbitals. However, in contrast to conventional

semiconductors, a decrease in orbital overlap raises the energy of the antibonding state (VBM) in halide perovskites, resulting in a decrease of the bandgap[39].

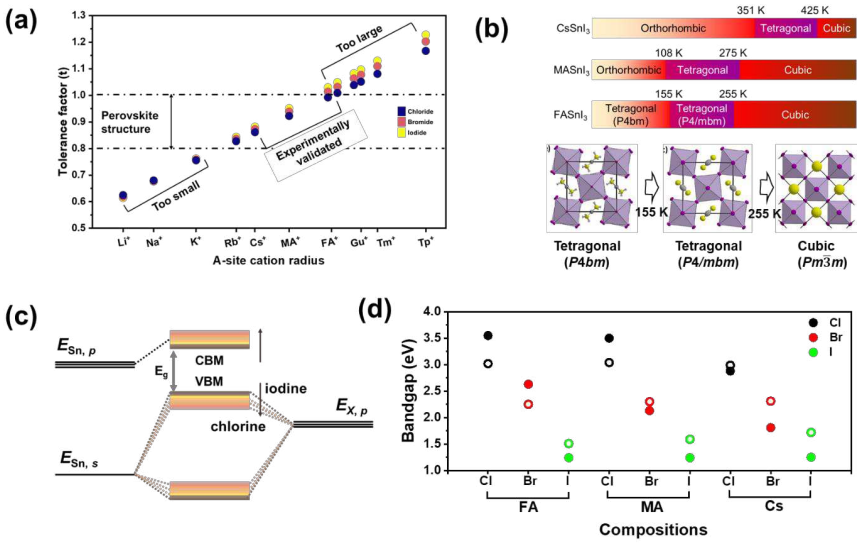

Figure 3. *Illustration of bandgap and crystal structure variation of Sn-based compounds and their role in optoelectronic properties. (a) Tolerance factor of Sn-based 3D halide perovskites with selected A-site cation, illustrating the stability region. (b) Evolution of crystal structure at different temperature for $ASnI_3$ (A = Cs, MA, FA) structure along with representative crystal structure FASnI3. The data were collected from [34, 35,] Schueller, Laurita, Fabini, Stoumpos, Kanatzidis and Seshadri [38, 40, 41 36, 37]. (c) Schematic illustration of orbital contribution to the band-edges in Sn-based halide perovskite. (d) Bandgap variation of Sn/Pb-based halide perovskites across different halides and selective A-site cations. Full circles and empty circles represent Pb-based and Sn-based halide perovskites respectively.*

Apart from the symmetry of the structure, the ease of tunability of optoelectronic properties via compositional alteration, especially of halides, remains one of the most interesting aspects of halide perovskites. Having corner-shared perovskite structure, 3D THPs exhibit direct bandgaps with strong absorption coefficients (> 10^4 cm^{-1}) in the visible region. The bandgaps

of THPs can be modified across a wider range via halide substitution. **Figure 3d** shows the variation of bandgaps in THPs with different compositions. For instance, the bandgaps of $CsSnX_3$ can be tuned continuously from 1.3 – 3 eV by varying halide composition from I to Cl[42]. However, the role of *A*-site cations on the bandgap is insignificant compared to that of halides. This could be explained by the electronic structure of THPs. As illustrated in **Figure 3c** and **4a**, the band-edges are essentially formed due to hybridizations of Sn 5s, 5p and halide *m*p orbitals which rules out the involvement of *A*-site cations. The slight change in bandgap with different *A*-site cations is thus due to changes in the crystal structure. The role of halides on the other hand, is much more predominant in determining the energy levels of VBM as the energy levels of the orbitals decrease from chlorine to iodine. As explained earlier, the decrease in orbital energies raises up the VBM due to antibonding nature, and consequently the bandgap decreases from chloride to iodide perovskites. The bandgap values are even smaller than LHPs for same halide *A*-site cations, making them even superior candidates for applications that require a wider absorption range (**Figure 3e**). Electronic structure calculations revealed that due to low-lying Sn-based orbitals, the valence band of THPs are much higher than that of Pb-based halide perovskites, and therefore this results in smaller bandgaps.

Apart from smaller bandgaps, experimental studies also report excellent carrier mobility (mostly hole mobility) in THPs, ranging from 10^2 to 10^3 cm^2 V^{-1} s^{-1} which agree well with DFT-based electronic structure calculations [43]. Unfortunately, the high conductivity in THPs may be assisted by strong self-doping. While the exact mechanism of self-doping is still debatable, it is generally accepted that the oxidation of Sn^{2+} to Sn^{4+} promotes Sn-vacancies, leading to *p*-doping. For example, evaporated $CsSnI_3$ polycrystalline thin-films showed an increase in conductivity by about 2 to 7 times when exposed to ambient as compared to the films measured under N_2, which is attributed to the oxidation-induced Sn-vacancies[44]. A comparative defect characterization study between $FASnI_3$ and $MASnI_3$ revealed that larger organic cations can increase the formation energies of Sn-vacancies by promoting weaker Sn

5*s* and I 5*p* antibonding coupling with longer Sn-I bond length (**Figure 4a**)[45]. Moreover, it was also found that conductivity of $FASnI_3$ can be tuned from *p*-type to neutral under Sn-rich growth conditions, while $MASnI_3$ showed high *p*-type behavior irrespective of growth conditions. Recently, De Angelis and co-workers utilized DFT calculations to show that Sn vacancies in bulk $MASnI_3$ are thermodynamically unfavorable[46]. This suggests that the origin of self-doping is the surface oxidation of Sn^{2+} to Sn^{4+} which later diffuses inside the bulk. They found that the formation of Sn^{4+} defects, i.e., the hypothesized oxidation products of $MASnI_3$, are not likely to form in the bulk. Moreover, Sn^{4+} defects, being metastable, will thermodynamically convert to Sn^{2+} by releasing two holes in the VB, which might be the reason for *p*-type self-doping. The corresponding defect transition levels of these species lie within the VB, making them shallow in nature, as shown in **Figure 4b**. Unfortunately, irrespective of the origin, high self-doping also leads to strong non-radiative recombination in THPs which results in short carrier lifetime (in ps and tens of ns as compared to hundreds of ns in LHPs) and poor PLQY. Earlier, Kanatzidis and co-workers showed that formation of Sn^{4+} centers could be prevented by introducing strong reducing agents such as H_3PO_2, which can even promote *n*-type mobility[47]. Several studies dedicated to the fabrication of superior Sn-based perovskite thin-films under reducing environment have shown excellent promise in improving optoelectronic properties in general[48]. Presence of excess Sn^{2+} in the precursor solution was also found to be beneficial in improving both the lifetime and radiative recombination, which are important parameters in optoelectronic applications[49]. In general, 3D THPs are expected to exhibit excellent optoelectronic properties suitable for high-performing optoelectronic devices as their electronic structure features similar characteristics as seen for LHPs. Nevertheless, the thermodynamic instability of Sn^{2+}, especially in iodide perovskites, remains a major challenge for stable high-performing optoelectronic devices.

The stability of 3D Sn-based halide perovskites was improved significantly when the Kanatzidis group reported a new variant of the 3D crystal structure of the THPs family, termed as "Hollow perovskite"[50, 51]. This type of structure is derived from the 3D parent phase by

incorporating small amounts of divalent organic cations such as ethylenediammonium (en), propylenediammonium (PN) or trimethylenediammonium (TN) without altering the 3D crystal structure (**Figure 4c**). A similar structure was also reported later with the incorporation of monovalent organic cations, such as 2-hydroxyethylammonium, within the $FASnI_3$ structure[52]. Incorporation of these moderate-sized cations apparently violates the structural tolerance factor ($t > 1$) due to their large ionic radii. Nevertheless, experimental results indicate that these organic cations accommodate inside the crystal lattice, most likely by partially replacing both $[SnI_6]^{4-}$ octahedra and smaller *A*-site cations, hence creating a hollow space within the 3D crystal structure. While it is not clear how this structure helps in preventing oxidation of Sn^{2+}, experimental results indicate that the ambient stability of hollow perovskites is much higher in compared to pristine Sn-based 3D halide perovskites. Moreover, the optoelectronic properties of these hollow perovskites resemble that of 3D THPs, albeit widening of the bandgap due to a less connected octahedral network arising from Sn^{2+} and *X*-site vacancies. Hollow perovskites also exhibit bandgap tunability via halide exchange, thus amplifying their promise as lead-free absorber materials.

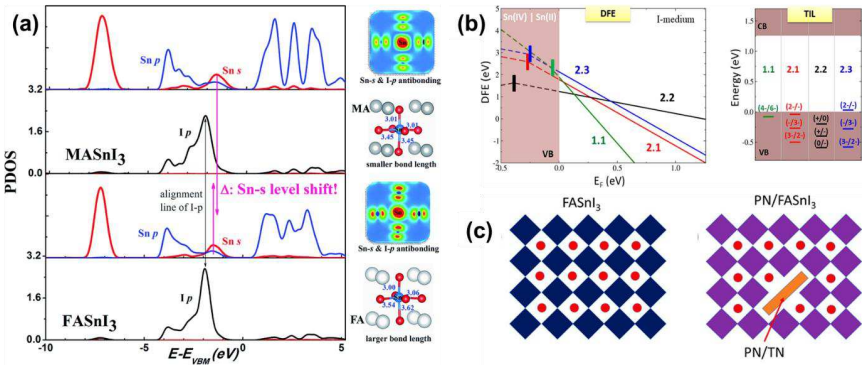

***Figure 4**. Electronic structure of Sn-based halide perovskites. (a) Comparative partial density of states analysis of $MASnI_3$ and $FASnI_3$, along with bond lengths and partial charge density, illustrating the role of A-site cations on the bonding environment. (b) Defect formation energy diagram of the modeled bulk Sn^{4+} defects as calculated for $MASnI_3$: three tin vacancies system*

*(3 V_{Sn}, structure **1.1**), I_2 added to tin Frenkel defect on the MA site (structure **2.1**), interstitial SnI_2 unit in the MA site (structure **2.2**), and interstitial SnI_4 unit in the MA site (structure **2.3**). Thermodynamic ionization levels (TIL) of the defects showing that they do not introduce deep levels in the band gap. Please refer to the reference for structural description. (c) Schematic illustration of "Hollow perovskites" along with 3D aristotype FASnI3. The orange rectangular block represents large organic cation which replaces both metal-halide octahedra and A-site cation to accommodate. (a) Reproduced with permission from Shi et al., Journal of Materials Chemistry, A **5** (29), 15124-15129 (2017). Copyright 2017 Royal Society of Chemistry.[45], (b) Reproduced with permission from Ricciarelli et al., ACS Energy Letters **5** (9), 2787-2795 (2020). Copyright 2020 American Chemical Society.[46], (c) Reproduced with permission from Ke et al., ACS Energy Letters **3** (7), 1470-1476 (2018). Copyright 2018 American Chemical Society.[50]*

3.1.2 Ge-based halide perovskites:

Despite having similar electronic structure and predicted promise, the Ge-based 3D analogues differ from their heavier congeners (Pb and Sn) because Ge^{2+} shows a pronounced effect of stereo-chemically active lone pair and because of their tendency to crystallize in polar space groups. Based on the tolerance factor estimation, only ammonium (NH_4^+), Rb^+, and Cs^+ cations are expected to form 3D perovskite structures with $[GeX_6]^{4-}$ octahedral network (t < 1)[30, 53]. However, cesium, methylammonium, and formamidinium have shown to crystallize in the 3D Ge-based halide perovskite (GHP) structure, albeit in trigonal crystal structure which is different from aristotype perovskite structure (*Pm*3*m*)[54]. In this structure, the Ge^{2+} cation forms three short and three long bonds with the halide anions within the $[GeX_6]^{4-}$ octahedron, resulting in off-centering of the metal cation (**Figure 5a**). The size of *A*-site cation heavily influences the distortion in $[GeI_6]^{4-}$ octahedra, where bond distortion index increases with larger *A*-site cations and with smaller halides (**Figure 5b**). Small ionic radius and the strong stereochemical activity of the $4s^2$ lone-pair electrons in Ge^{2+} cation is hypothesized to be the reason for this distorted structure. While the origin of the distortion is still under debate, the rotation of octahedra (octahedral tilting) is linked to many interesting phenomena, ranging from

electronic and magnetic properties[55], second harmonic generation[54], to improper ferroelectricity[56]. First-principle electronic structure calculations revealed that this distortion leads to less overlap between metal-halide antibonding orbitals in the valence band, resulting in increase in the bandgaps of GHPs as compared to LHPs. For example, iodide-based GHPs exhibit direct bandgap ranging from 1.6–2.5 eV, depending upon the *A*-site cation, with the smallest being in $CsGeI_3$ (**Figure 5c**). This remarkable dependency of bandgaps on different *A*-site cation is the strongest compared to that of Pb- or Sn-based halide perovskites. From single crystal data, this remarkable modification of bandgap can be directly linked to the octahedral distortions as larger A-site cation results in larger distortions and consequently larger bandgaps [54]. **Figure 5e** further illustrates a change in optical bandgaps of GHPs with increasing distortion in metal octahedra. The structural distortion is also expected to impart anisotropy in charge transport and optical absorption[56]. The anisotropic behaviour was further supported by the sub-bandgap absorption in $MAGeI_3$, presumably due to strong ferroelectric polarizations arising from anisotropic charge transport and absorption. This could lead to a substantial increase in incident photon conversion efficiency during photovoltaic or photodetection applications. Nevertheless, 3D Ge-based halide perovskites are also plagued by instability in ambient environment. While early theoretical calculations showed that $MAGeI_3$ is less likely to degrade into precursors (MAI and GeI_2) as compared to analogous $MAPbI_3$, experimental results indicate that Ge-based 3D halide perovskites follow a similar degradation pathways like Sn-based 3D halide perovskites[57] at higher degradation rates. A detailed investigation on the intrinsic point defects in $CsGeI_3$ showed the presence of mid-bandgap iodine vacancies (V_I), which is remarkably different from Pb- and Sn-based 3D halide perovskites[58]. While the exact reason is not explained, we can hypothesize that distortion in octahedra and poor hybridizations are the main reasons for this anomaly. Moreover, Ge-based halide precursors (GeX_2) are also only mildly soluble in organic solvents, resulting in inadequate processability for thin-films. Therefore, experimental studies on GHPs are still scarce as compared to other perovskites and most of the studies are dedicated towards theoretical calculations.

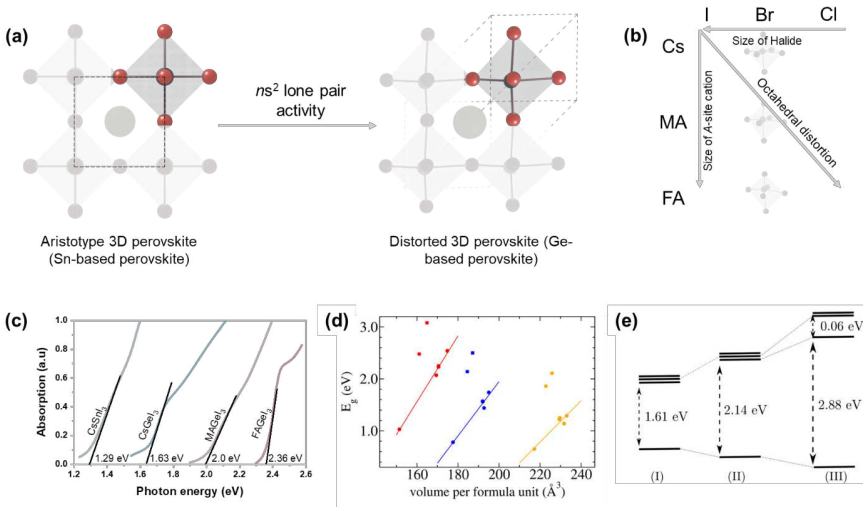

***Figure 5**: Octahedral distortion in Ge-based 3D perovskites and their optical bandgap. (a) Schematic illustration of octahedral distortion in Ge-based 3D halide perovskite due to active lone-pair effect and resulting polar crystal structure as compared to aristotype structure in conventional halide perovskites. (b) Graphic representation of octahedral distortion across $AGeX_3$ composition (A = Cs, MA, FA, X = Cl, Br, I). (c) UV-Vis absorption spectra of Ge-based halide perovskites along with CsSnI3 for comparison. Solid black lines represent the bandgap of that composition. (d) Fundamental energy band gap, E_g, as a function of the volume per formula unit for the $CsGeX_3$ perovskites. The straight lines represent a linear regression from the ideal cubic, D-cubic, D-tetragonal or, D-tetragonal IR, and super cubic phases. The red, blue, and orange colors represent X = Cl, Br, and I ions, respectively. Circles represent the structures derived from the ideal cubic, whereas squares represent the hexagonal phases. (e) KS eigenvalues for the valence band maximum (VBM) and conduction band minimum (CBM) of the $CsGeCl_3$ perovskite calculated with the HSE06 functional. (I) ideal cubic phase in its optimized lattice parameter, (II) ideal cubic phase with the lattice parameter of the D-cubic phase, and (III) D-cubic phase. (c) Reproduced with permission from Thirumal et al., Journal of Materials Chemistry A 3, 23829-23832 (2015). Copyright 2012 Royal Society of Chemistry*

(e) Reproduced with permission from Dias et al., The Journal of Physical Chemistry C ***125*** *(35), 19142-19155 (2021). Copyright 2021 American Chemical Society.*[59]

3.1.3 Other 3D halide perovskites:

Among other divalent cations, only Mg^{2+}, Ca^{2+}, Sr^{2+}, and Ba^{2+} can form 3D perovskite structures according to the Goldschmidt tolerance factor estimation[30]. However, the absence of ns^2 electrons renders their optoelectronic properties vastly different from LHPs. Theoretical calculations also predict wide band gaps and unfavorable optoelectronic properties, which attracted less attention for experimental synthesis[60]. [61] utilized DFT-based high-throughput screening to assess the optoelectronic properties of various divalent metal cation-based 3D perovskite crystal structures. Many of these divalent cations-based hypothetical perovskites exhibited distorted crystal structures and instability. The authors identified Mg^{2+} as a potential candidate with the calculated electronic bandgap was found to be 0.9 eV, 1.5 eV and 1.7 eV for $FAMgI_3$, $MAMgI_3$, and $CsMgI_3$ composition respectively based on LDA approximation. Likewise, Krishnamoorthy et al [31] also carried out computational screening of 360 AMX_3 chemical compositions with *A*-site being Cs^+, Rb^+, and K^+ [31]. While both studies agree well on the electronic bandgaps of Mg-based hypothetical halide perovskite, formation energies of Mg-based halide perovskites in the second study were found to be much larger. At present, only face-sharing low-dimensional structure of $CsMgI_3$ having wide bandgap (4.8 eV) has been reported[62], which will be discussed in perovskite-derivative section. Among others, the pseudo-cubic $CaCaI_3$ has been experimentally synthesized exhibit an optical bandgap of 2.95 eV, which makes it unsuitable for photo-absorption applications[63]. Theoretical calculations also predict stable perovskite structures for Sr- and Ba-based halide perovskites, albeit they are also likely to exhibit large bandgaps due to smaller electronegativity difference and lack of *d*-orbitals in the valence[64, 65]. However, at present, no experimental evidence can be found to prove the existence of these structures. Divalent rare-earth and lanthanide elements are also known to crystallize into perovskite structures with halides since the 1980s, as most of these studies are focused on their crystal structure and calorimetric investigations[66-68]. Early results indicate that $CsEuCl_3$ stabilizes into distorted tetragonal structure although degradation occurs

under ambient conditions[66]. Similar results were also obtained for bromide compounds[69]. Although both the compounds exhibit large bandgaps which are undesirable for photo-absorption applications, they show strong photoluminescence, which could make them excellent candidates for light emission.

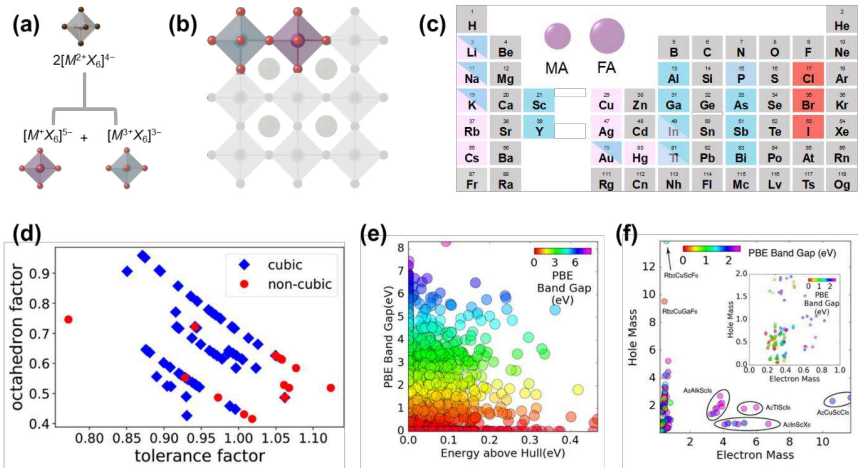

Figure 6: *Double perovskites. (a) Schematic illustration of splitting divalent cations into monovalent and trivalent cation to form (b) double perovskite structure. (c) Partial periodic table of elements showing potential monovalent and trivalent cations for double perovskite structure. (d) A structure map for known halide $A_2BB'X_6$ compounds. Crystal structures reported in the ICSD are indicated by blue diamonds and red circles for cubic and noncubic structure, respectively. (e) Distribution of calculated energy above the hull and PBE band gap. The scatter plot illustrates the distribution of calculated energies above hull and band gap values for 1149 cubic double perovskite halide compounds. (b) The distribution of calculated effective mass and PBE band gap values. The scatter plot illustrates the distribution of electron mass and hole mass for 189 double perovskite halides with E_{hull} < 50 meV/atom and 0.1 eV < E_g < 2.5 eV. Inset: zoom-in view showing only materials with small effective masses. (d-f) Reproduced with permission from Cai et al., Chemistry of Materials* ***31*** *(15), 5392-5401 (2019). Copyright 2019 American Chemical Society.*[70]

3.1.4 Double perovskites:

Double perovskites (or elpasolites), with a general formula of $AB'B''X_6$ are an extended family of 3D perovskite structure in which one monovalent (*B′*) and one trivalent metal cation (*B″*) are stacked alternatively to mimic the divalent oxidation state required for halide perovskite structures. As opposed to alloyed perovskites (such as $CsPb_{1-x}Sn_xX_3$), double perovskites must contain two structurally distinguishable $[B^{n+}X_6]^{n-6}$ motifs. Because of the double occupancy at the *B*-site, these perovskites are simply called "double perovskites"[71]. Halide double perovskites came into prominence when three groups independently reported synthesis and optoelectronic properties of Cs_2AgBiX_6 (*X* = Cl, Br) in 2016[61, 72, 73]. A recent review on the historical development of halide double perovskites can be found in the work by Wolf and co-workers [74]. Following the discovery of Cs_2AgBiX_6, several studies dedicated towards high throughput screening and novel synthesis protocols. Theoretical calculations predicted several double perovskites with B′ being Li^+, Na^+, K^+, Rb^+, Ag^+, Tl^+, Cu^+ etc., and B″ being Al^{3+}, Ga^{3+}, In^{3+}, Tl^{3+}, Bi^{3+}, Sb^{3+}, and lanthanides, and subsequently, many of them have been experimentally synthesized. In a typical crystal structure, two heterovalent cations are arranged alternatively (rock-salt) along three four-fold cubic axes to form corner-shared octahedral network as shown in **Figure 6a, b**. The monovalent cation still occupies the cubo-octahedral voids to hold the structure in 3D space. While the ordering for the *B*-site can be rock-salt or random for oxide double perovskites, the former has been shown to be thermodynamically preferred for the halides [75]. Although several combinations of cation pairs can be put into octahedral positions based on oxidation state, the structural stability (aristotype) of the double perovskites still depends on both tolerance factor (*t*) and octahedral factor (μ). While *t* has same role as in conventional halide perovskite, μ (r_B/r_X, *r* is the radius of *B*-site cation (*B*) and halide (*X*)) determines whether a certain cation can form octahedral bonding with halides. Too small or too large a value of μ would result in large distortions, while an optimal value between 0.44 and 0.90 was found to promote cubic structure. A study employing ~2000 combinations of inorganic cations in *B*-site along with K^+, Rb^+, and Cs^+ as *A*-site cation, found 1149 compounds can form cubic structure (**Figure 6d**) and 305 (not

including fluorides) of them are within thermodynamic stability range (**Figure 6e**)[70]. A recent high-throughput DFT-based convex-hull calculation also predicted that only 112 of the 980 compounds are thermodynamically stable[76]. The difference between two studies is the cut-off energy used to estimate the stability. Having more than 1440 compositions that are known to have double perovskite structure, many of them are fluoride-based, which limits their solution-processed synthesizability[77]. Among heavier halides, nearly all of the synthesized double perovskites exhibit large optical bandgaps, arising from the chemical mismatch between monovalent and trivalent cations. Smaller bandgaps were predicted for In^+ and Cu^+ as B′ and Sb^{3+}/Bi^{3+} as B″ cation combination[61, 78]. Nevertheless, In^+-based compounds suffer from poor solubility in organic solvents and spontaneous oxidation from In^+ to In^{3+}[79] which poses a major question on the synthesizability of In^+-based halide double perovskites. Similarly, synthesizability of Cu^+-based iodide double perovskite also raises questions as six-fold coordination of Cu^+ with iodide and bromide is thermodynamically unfavourable (**Figure 2**). These results indicate the need to consider accurate redox chemistry when predicting stability of new compounds, especially when less common oxidation states are involved.

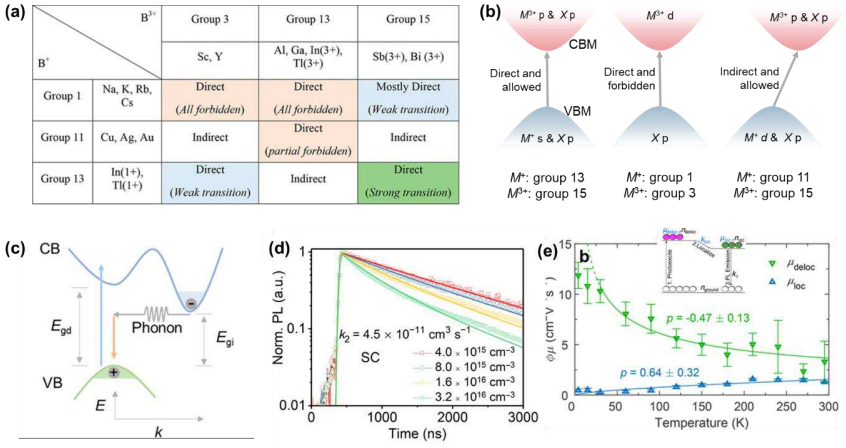

Figure 7: *(a) Possible Combinations for $A_2B^+B^{3+}X_6$ Double Perovskites, (b) Schematic illustration of bandstructure of three prominent categories of double perovskites. (c) Schematic*

*of the phonon-assisted transitions at the indirect band edge for a typical indirect semiconductor. VB, valence band; CB, conduction band; Egd, direct band gap; Egi, indirect band gap. (d) Fluence-dependent PL decays of $Cs_2AgBiBr_6$ SC upon 530-nm laser excitation. (e) Temperature dependence of the effective charge-carrier mobilities associated with the delocalized (μ_{deloc}, green) and localized (μ_{loc}, blue) states. Power-law fits are plotted as solid lines in the corresponding colors, with their exponents (p) displayed alongside. (c) (d) Reproduced from Wu et al., Science Advances **7** (8), eabd3160 under a Creative Commons Attribution 4.0 International (CC BY 4.0) license. Copyright 2019 American Association for the Advancement of Science .[80] (e) Reproduced with permission from Wright et al., The Journal of Physical Chemistry Letters **12** (13), 3352-3360 (2021). Copyright 2021 American Chemical Society, under a Creative Commons Attribution 4.0 International (CC BY 4.0) license. No changes were made.[81]*

The physical and optoelectronic properties of double perovskites are determined by the *B*-site cations in combination with halides, just like conventional halide perovskites. These promising double perovskites can be classified into nine groups based on the electronic structure of the constituent B-site cation (**Figure 7a**) and **Figure 7b** shows the schematic band structure of the three representative categories. For the case of the most famous halide double perovskite, $Cs_2AgBiBr_6$, the VBM mainly originates from the antibonding states of Ag 4*d* and Br 4*p* orbitals, while the CBM is mainly composed of Bi 6p orbitals with slight contribution from Ag 5s and Br 4p orbitals. The Bi 6*s* lone-pair orbitals have no significant contribution to the VBM as they lie at 10.2 eV below the VBM. This apparent mismatch of hybridization leads to indirect and large bandgap in $Cs_2AgBiBr_6$, which results in poor photoluminescence. Interestingly, Gao and coworkers[82] observed that the bandgap can be reduced by 0.26 eV from 1.98 eV in pristine $Cs_2AgBiBr_6$ by fabricating the crystal at high temperature (150 ℃). The authors claimed that temperature-induced disorder is the most likely reason for this bandgap reduction. One the other hand, alkali metals in B′-site can induce direct bandgaps, yet due to parity forbidden

transition, these compounds also exhibit large bandgap and are usually transparent. A similar result also found for $Cs_2AgInCl_6$[60].

The defect chemistry of these double perovskites remains a subject under debate. The dominant defects in $Cs_2AgBiBr_6$, such as Ag_{Bi}, V_{Bi}, and Br_i, are found to create mid-bandgap states, despite having an antibonding VBM [83]. In addition, shallow defects such as V_{Ag} are also abundant in $Cs_2AgBiBr_6$. Similar findings were also obtained for $Cs_2AgBiCl_6$ and $Cs_2AgInCl_6$ compounds[84]. This is in stark contrast to conventional halide perovskites which are tolerant towards intrinsic defects. In addition, experimental studies indicate that $Cs_2AgBiBr_6$ possesses long carrier lifetimes (~688 ns in crystals and ~675 ns in powder[72]) along with long carrier diffusion length (~ 1 μm[85]) and moderate defect densities (~ 10^9 cm^{-3} in crystals and 10^{16}–10^{17} cm^{-3} in films[86, 87]). This apparent contrasting results necessitate further validation from both experimental and theoretical perspectives to quantify the defect levels and concentrations, to understand the intrinsic relationship between stoichiometry and defects and to provide guidance for reducing the deep-level defects in $Cs_2AgBiBr_6$.

A variant of these double perovskites can also be obtained with a single metal cation having both monovalent and trivalent oxidation state. These mixed-valence double perovskites include compounds based on Tl, In, and Au (the latter shows strongly distorted octahedra). While Tl is highly toxic, pure Au-based compounds can be of interest for optoelectronic applications. All inorganic $Cs_2Au^+Au^{3+}Cl_6$ was first synthesized in 1922[88] and the structure was determined later in 1938 along with $Cs_2Ag^+Au^{3+}Cl_6$ [89]. Both compounds are black in color and crystallize in the tetragonal structure. However, early work on Au-based halide perovskites were limited to structural characterizations and pressure-induced insulator-to-metal transition [90-92]. In contrast to conventional double perovskites, Au-based halide perovskites comprises corner-connected heavily-distorted haloaurate octahedra, owing to presence of linear $[Au^+X_2]^-$ and square-planar $[Au^{3+}X_4]$ complexes (**Figure 8a, b**). This distortion arises due to the large size difference between Au^+ and Au^{3+} [93]. Recently, Au-based halide perovskites gained renewed interests due to their small and direct bandgap (e.g., 1.2 eV for $MA_2Au^+Au^{3+}I_6$) which

is highly desirable for PV applications. For instance, a theoretical study calculated power conversion efficiency of only 50 nm thin $Cs_2Au^+Au^{3+}I_6$ layer can reach up to 18%, while for the same thickness, $MAPbI_3$ can only harvest about 8% of solar energy[94] (**Figure 8c**). Earlier reports indicated the origin of the small band gap to the metal−ligand intervalence charge transfer (IVCT) between the $[Au^+X_2]^-$ and the $[Au^{3+}X_4]^-$ groups[91]. Recent theoretical calculation indicates that the presence of intermediate bandgap, originating from an antibonding hybridization of Au^{3+} $d_{x^2-y^2}$ orbital and I *p* orbital is the most likely reason for the smaller bandgap[94]. Murasugi et al[95] recently synthesized a series of Au-based halide perovskites and found that the crystal structure is heavily dependent on the size of *A*-site cation (**Figure 8d**). Due to heavily distorted gold halide octahedra, the perovskite structure can be formed even beyond tolerance factor limit (t >1), however crystal symmetry reduces at higher t values (monoclinic structure for 1.07 < t <1.2). **Figure 8e** shows the optical absorption spectra of gold halide perovskites with different *A*-site cations which illustrates the continuous increase of bandgap with larger A-site cation. Additional parameter in determining the band gap is the in-plane distance $d(Au^{I}\cdots I)$ which specifies the anisotropic optoelectronic properties.

Another family of the halide double perovskites are based on lanthanide (Ln) series where B^{3+} site is essentially occupied by lanthanide (III) cations. The development of lanthanide double perovskites began in last century as new scintillator materials for radiation detection; consequently, most of the lanthanides are used as host materials for rare-earth dopants (e.g., Ce^{3+}), and their pristine physical and optoelectronic properties are often overlooked. A theoretical screening was carried out based on Embedded-Ion Method (EIM) potential[96] to characterize 640 lanthanide double perovskites, covering five alkali elements Li, Na, K, Rb, and Cs, four halogen elements F, Cl, Br, and I, and eight selected lanthanide elements La, Nd, Eu, Er, Ce, Sc, Y, and Gd. Furthermore, 13 Ln-based double perovskites were synthesized, out of which 9 compounds were crystallized in cubic double perovskite structure. Nevertheless, most of the lanthanide-based halide double perovskites are expected to exhibit extremely large optical bandgap (~ 6 eV or more), which makes them unsuitable for

optoelectronic applications. Recently, Hu et al[97] synthesized $Cs_2NaTbCl_6$ and $Cs_2NaEuCl_6$ crystals by hydrothermal method. Both crystals were transparent and exhibited long PL lifetime (in ms). First-principle calculations revealed that due to localized *f* states, large electronegativity differences between alkali cations and lanthanides, and the large distance between the trivalent cations localizes band-edges, these compounds are expected to offer poor carrier mobilities[98, 99]. The discrete band structure of these compounds further suppresses thermalization of hot carriers, which is again undesirable for optoelectronic applications.

All the double perovskites described above possess a 3D corner-shared network in which two different valent cations form a rock-salt structure. Nevertheless, more exotic 3D perovskite structures can be formed by introducing defects in the crystal structure. Yang's group exemplified this idea by replacing the atomic positions in conventional $BaTiO_3$ lattice with metal halide octahedra, thus forming an extended ionic octahedron network (ION) which are charge-balanced by the monovalent cation[100]. They discovered a novel perovskite structure $Cs_8Au_{3.5}In_{1.5}Cl_{23}$ which can be represented as $[[InCl_6][AuCl_5][Au/InCl_4]_3]^{8-}$, where three different ionic octahedra $[InCl_6]$, $[AuCl_6]$, and $[Au/InCl_6]$ are still connected at the vertex. While the compound exhibit process dependent properties due to spontaneous disproportionation reaction of Au^+ and Au^{3+}, this concept can provide an enormous chemical space for further exploration, and thus it opens a new venue for the rational design of new halide perovskite materials.

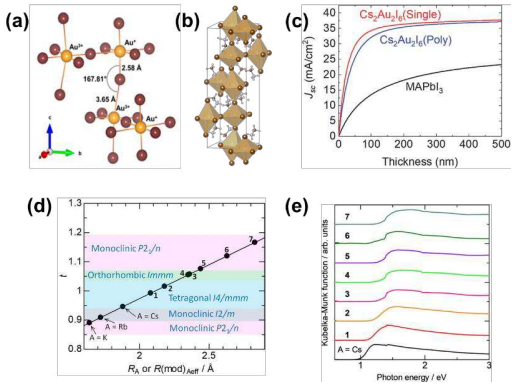

Figure 8: *Gold-based mixed valence halide perovskites. (a) ball-and-stick model of Au-based halide perovskites structure showing distortion along in-plane and off-plane. (c) polyhedral model of the same. (b) theoretical short-circuit current density from Au-based iodide perovskites under 1-sun illumination. (d) Tolerance factors for gold–iodide perovskites as a function of modified effective radii of cations R(mod)$_{Aeff}$. The solid line is a guide for the eye. (e) UV/Vis-NIR spectra of $A_2[Au^{I}I_2][Au^{III}I_4]$ [A = MA(1), FA (2)], $A'_2[I_3]_{1-x}[Au^{I}I_2]_x[Au^{III}I_4]$ [A'=imidazolium (IMD) (3), guanidinium (GUA) (4), dimethylammonium (DMA) (5), pyridinium (PY) (6), and piperizinium (PIP) (7)] together with $Cs[AuI_2][AuI_4]$. (a), (b) Reproduced with permission from Ghosh et al, Chemistry of Materials **32** (15), 6318-6325 (2020). Copyright 2020 American Chemical Society.[93] (c) Reproduced with permission from Debbichi et al., Adv. Mater., **30** (12), 1707001 (2018). Copyright 2018 Wiley-VCH GmbH.[94], (d), (e) Reproduced with permission from Murasugi et al., Chem. Eur. J., **25** (42), 9885-9891 (2019). Copyright 2019 Wiley-VCH GmbH.[95]*

3.2 2D layered structure:

Contrary to the rigid 3D perovskite structure, 2D layered perovskite structure can be rationalized as slabs or sheets of corner-shared octahedral networks sandwiched between large cations or cationic structural moieties. The structure essentially forms when the cubo-octahedral space in 3D perovskite structure cannot accommodate larger cationic moieties, resulting in separation of the octahedral sheets along certain crystallographic planes

corresponding to the axis of an ideal cubic perovskite. When the two adjacent inorganic layers has an offset of (0.5, 0.5), as shown in **Figure 9a**, the large organic molecule occupies the interlayer space between the inorganic layer, and the smaller A-site cation fits within the cubo-octahedral voids generated within the inorganic layers. The larger monovalent organic cations are anchored by hydrogen bonding with halide atoms at only one side, forming an interdigitated organic layer structure. This structure is known as Ruddlesden-Popper (RP) phase. In another structure variation, the adjacent inorganic layers exhibit a coordinate displacement of (0,0), such as in butylammonium germanium iodide, which is known as the Dion-Jacobson (DJ) phase (**Figure 9b**). In this structure, there is only one layer of bulky organic layer between the inorganic octahedral sheets as compared to two organic layers required to form RP structure. Consequently, DJ structures usually have a shorter *X*−*X* interlayer distance as compared to RP phase. An intermediate structure is also possible when the parallel inorganic layer has a coordinate offset of (0.5, 0) and the alternating *A*-site cations occupy the pockets of inorganic metal octahedral layers and interlayer space between them (**Figure 9c**). This kind of structure is known as Alternating Cation in Interlayer space (ACI) type. The chemical formula of RP, DJ, and ACI structure can be represented as $A'_2A_{n-1}B_nX_{3n+1}$, $A'A_{n-1}B_nX_{3n+1}$, and $A'A_nB_nX_{3n+1}$ respectively, where *n* indicates the number of inorganic layers that are stack together (Figure 9d). In the current era, with the advent of halide perovskites, the inclusion of non-spherical and often highly anisotropic organic molecules at the inter-layer *A*-site opened up further variations in the layered structure, and currently 'layer shift' is more often used terminology to describe low-dimensional halide perovskites, rather distinguishing between RP, DJ, and ACI phases[101, 102]. Depending on the crystallographic planes, 2D layered

structures can also be classified as the <100>, <110>, or <111> oriented 2D perovskites (Figure 9e).

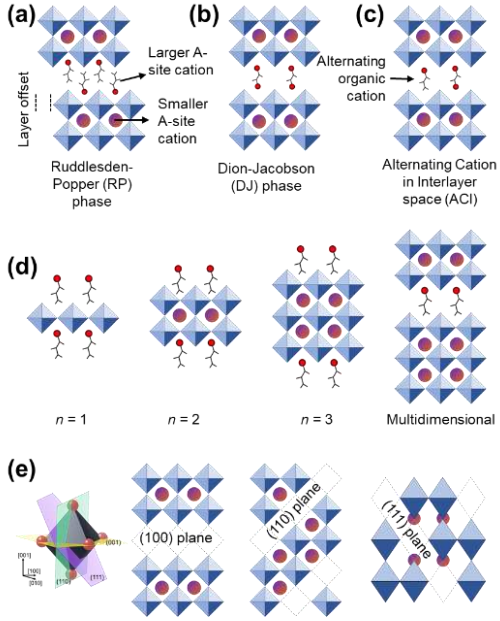

Figure 9: *Low-dimensional halide perovskite structure. Schematic illustration of (a) Ruddlesden-Popper (RP) phase, (b) Dion-Jacobson (DJ) phase, (c) Alternating Cation in Interlayer space (ACI) phase. Panel (d) shows the different number (n) of inorganic layers forming low-dimensional structures (from n = 1 to n = multidimensional). Panel (e) illustrates (100)-, (110)-, and (111)-oriented low-dimensional structures. (Empty octahedron indicates missing planes in the 3D perovskite structure.)*

3.2.1 Sn/Ge-based 2D structure

The development of organic-inorganic lead-free 2D structures also started in early 1990s when Mitzi et al [103], reported a family of Sn-based layered halide perovskites, $(C_4H_9NH_3)_2(CH_3NH_3)_{n-1}Sn_nI_{3n+1}$ which showed semiconducting to metallic transition with increasing number of inorganic layers (n). These structures resemble the Ruddlesden-Popper (RP) phase. Later, the low-dimensional family was extended to Ge-based halide perovskites along with more complicated organic cations[104-106]. As there are no size restrictions for the *A*-

site cation, a plethora of monoammonium and diammonium cations are employed to form (100)-oriented 2D structure. The optoelectronic properties of these 2D layered perovskites mostly depend on the nature of inorganic layers and the separation between them, while the organic layers play a limited role in the band edge formation. This was confirmed in early works as the electronic structure of low-dimensional tin halide perovskites, calculated using the extended Hückel tight binding method, was found to be similar to that of a single $[SnI_4]^{2-}$ layer[107, 108]. **Figure 10a,b** show the calculated band structure for an idealized undistorted 2D SnI_4^{2-} perovskite sheet and corresponding projected density of states. The band edge composition is similar to that of 3D THPs as described previously. Nevertheless, one striking difference is the strong dispersion of the band-structure along in-plane as compared to that of out-of-plane direction (Γ to a point located at the edge of the Brillouin zone), rendering the valence band and conduction band to be two dimensional. Recent DFT-based calculations also agree well with the fact that *A*/*A*′-site cations do not contribute to the VBM and CBM, which are entirely formed by hybridization between metal and halide orbitals [109-111]. This is since the ammonium cations usually have larger HOMO-LUMO gaps as compared to that of inorganic layers and the organic molecules are attached by only hydrogen or van der Waals bonding with the inorganic layer. Consequently, there is negligible electronic coupling between the perovskite sheets, and flat dispersion of electronic bands are observed along the direction of the stacking axis.

The most pronounced effect of the quantum confinement and structural templating can be seen in the excitation binding energy and optical bandgap in the absorption spectrum. Excitons are Coulombically-bound neutral electron-hole pairs which are prevalent in low-dimensional structures due to quantum confinement effect. Due to large dielectric difference between organic layer (~ 2.6) and inorganic layers (~ 6), 2D halide perovskites behave as natural quantum-well, exhibiting strong excitonic behavior. For optoelectronic applications, it is desirable that excitons either are dissociated into free carriers (e.g., for photovoltaics) or radiatively recombine (e.g., for LEDs). A critical parameter is the exciton binding energy (E_b)

which is defined as the difference between the energy of the excitonic state and the electronic band gap, determines the behavior of excitonic states in a material. In 3D halide perovskites, E_b is comparable to or smaller than kT (thermal energy) and the exciton can be dissociated easily into free carriers at room temperature. However, for efficient LEDs, a reasonably high E_b is needed to enhance electron-hole confinement. The values of bandgap and exciton binding energies in 2D perovskites depend on the number of inorganic layers (n) and the choice of organic cation. Additionally, larger differences in dielectric constants lead to higher exciton binding energies, electronic band gaps, and flat dispersion.

In the case of electronic bandgaps, quantum confinement leads to a systematic increase of the band gap with decreasing layer thickness. **Figure 10c** illustrates the variation of computed bandgaps of a hypothetical series $Cs_{n+1}Sn_nX_{3n+1}$ (X = Cl, Br, I) against number of inorganic layers (n). This is a fair assumption due to negligible interaction of *A*-site cations on the band structure and the fact that inorganic cations usually promote a non-distorted structure. However, in-plane *B*–*X* bonds become shorter than in bulk during structure relaxation, indicating the octahedral distortion may be necessary to stabilize the low-dimensional structure. On the other hand, the band gap gradually approaches the bulk value ($n \rightarrow \infty$) with the increase in the layer thickness as expected. **Figure 10d** shows the computed band structures of the hypothetical $Cs_{n+1}Sn_nX_{3n+1}$ (X = Br, I) series. Several main features can be highlighted with increasing the number of inorganic layers (n) such as (i) nature of bandgap remain direct for any number of inorganic layers, (ii) the band gap gradually becomes smaller, and (iii) increase in sub-bands and decrease of bandwidth in both CB and VB, (iv) substitution of I by Br lead to larger the band gaps. As previously described, the in-plane hybridization between Sn and *X* orbitals is valid for all the low-dimensional structure the bandgap originates which results in similar band structure, while the latter two can be explained by the reduced quantum confinement with increasing inorganic layer.

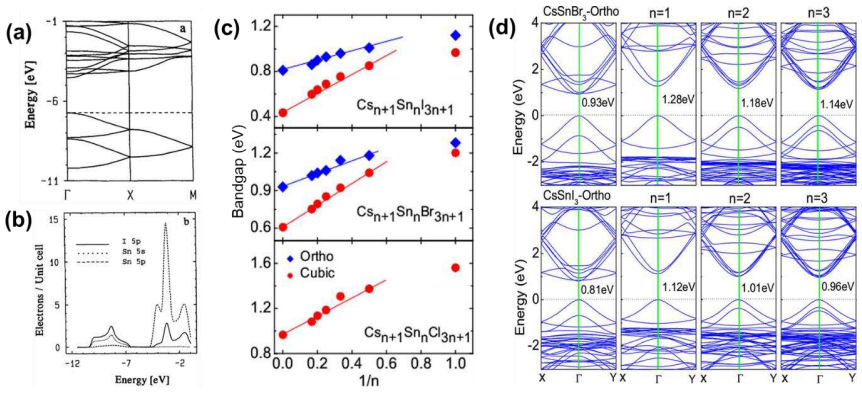

Figure 10. *Electronic structure of low-dimensional Sn-based halide perovskites. Valence and conduction bands calculated for a single SnI_4^{2-} layer. (a) dispersion relations, where the dashed line refers to the highest occupied level. (b) atomic orbital compositions in terms of projected density of states. (c) Band gap for cubic and orthorhombic bulk and layers (n = 1–6) without spin–orbit interactions. For $Cs_{n+1}Sn_nCl_{3n+1}$ results are given only for the cubic phase. We have fitted the points (except for n = 1) with a line to show the behavior as 1/n changes. (d) Band structure plots for bulk $CsSnI_3$ and $CsSnBr_3$ in the orthorhombic phase and their layers with 1 to 3 unit cell thickness. The VBM is taken as reference of energy. The value of the band gap is given in each case. (a), (b) Reproduced with permission from Papavassiliou et al., Solid State Communications* ***91*** *(9), 695-698 (1994). Copyright 1994 Elsevier Ltd.[107], (c) and (d) Reproduced with permission from Bala et al., The Journal of Physical Chemistry C* ***122*** *(13), 7464-7473 (2018). Copyright 2018 American Chemical Society.[111]*

In other words, with increasing the number of inorganic layers, the optoelectronic properties of 2D layered structure draw closer to that of the 3D structure. **Figure 11a** shows the experimentally-obtained optical absorption spectra of $(CH_3(CH_2)_3NH_3)_2(CH_3NH_3)_{n-1}Sn_nI_{3n+1}$ perovskite series. As observed in electronic band structure calculations, the optical bandgap drastically reduced from 1.83 eV (n = 1) to 1.37 eV (n = 5), moving close to 3D $CH_3NH_3SnI_3$ (1.2 eV, $n = \infty$)[112]. Similar results were also obtained in analogous $(BA)_2(FA)_{n-1}Sn_nI_{3n+1}$ series which shows a bandgap tunability from 1.96 eV (n=1) to 1.4 eV (n = 10) only by varying number

of inorganic layers (**Figure 11b)**[113]. The absorption spectra of $(BA)_2(FA)_{n-1}Sn_nI_{3n+1}$ series were later fitted to a quantum-well model to illustrate the variation of exciton binding energies, from 287 meV (n = 1) to 10 meV (n = 10) (**Figure 11c**). Such high binding energies essentially establish the excitonic nature of the lower n (1 and 2, in this case) perovskites, while presence of free carriers was observed in n = 5 and n =10 compounds. Similar studies were also directed towards Ge-based halide perovskites which show surprisingly much less dependence of bandgap on the number of inorganic layers[114, 115]. For example, a bandgap difference between n = 1 and n = ∞ is only 0.3 eV in $(CH_3(CH_2)_3NH_3)_2(CH_3NH_3)_{n-1}Ge_nBr_{3n+1}$ (**Figure 11g**). Through DFT-based electronic structure calculations, the weak dependence of bandgaps is attributed to the strong localized states of germanium orbitals, leading to similar band edge energies of layered structure and parent 3D perovskite[114, 116].

Nevertheless, limited efforts were directed towards low-dimensional GHPs, mostly due to their large bandgap. Alloying with Sn has been shown a viable strategy to reduce the bandgap of low-dimensional GHPs[117]. It should be noted here that in most studies, the number of inorganic layers is usually assumed based on the precursor composition (stoichiometry) as it is difficult to determine accurate crystallographic information for higher order structures. For Pb-based halide perovskites, higher n (≥ 5) compounds usually have positive formation energy [118], leading to unfavorable crystallization kinetics. Ma et al[116] computed formation enthalpies of Sn- and Ge-based RP phases with respect to two decomposition pathways: (a) oxidation to respective tetravalent state, and (b) degradation to the precursors. Both the pathways showed similar degradation trend with higher n structures having more positive enthalpy as compared to lower n structure. In addition, higher n structures are also more likely to degrade under oxidative environment, and less stable as compared to lower n structures. However, there are no calorimetric studies dedicated towards lead-free halide perovskites.

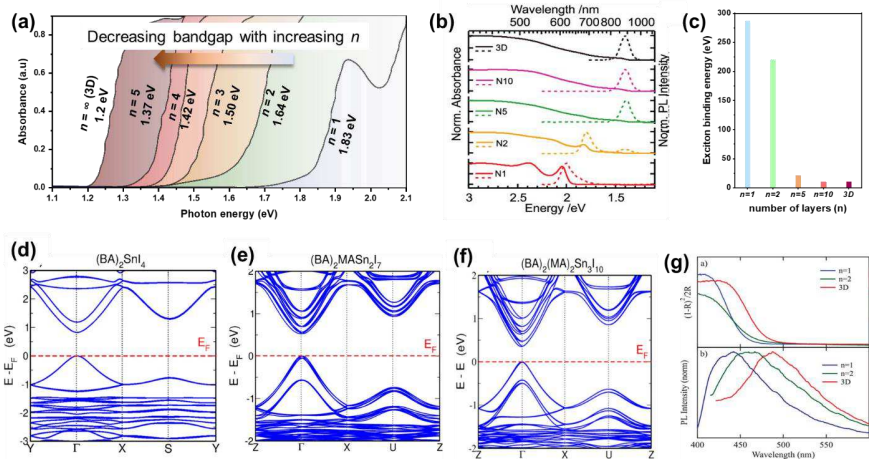

Figure 11. *(a) Optical absorption spectra of bulk polycrystalline $(BA)_2(MA)_{n-1}Sn_nI_{3n+1}$ series and their bandgap, (b) ultraviolet–visible (solid lines) and PL (dashed lines) spectra of $BA_2FA_{n-1}Sn_nI_{3n+1}$ (n = 1, 2, 5, 10, and ∞, referring to N1, N2, N5, N10, and 3D, respectively) perovskite thin-film samples. (c) exciton binding energy of the same. (d), (e), (f) Band structures of $(BA)_2(MA)_{n-1}Sn_nI_{3n+1}$, for (d) n = 1, (e) n = 2, (f) n = 4 obtained with PBEsol and SOC. (a) Reproduced with permission from Cao et al., ACS Energy Letters* ***2*** *(5), 982-990 (2017). Copyright 2017 American Chemical Society.*[112]*, (b) Reproduced with permission from Narra et al., The Journal of Physical Chemistry Letters* ***12*** *(51), 12292-12299 (2021). Copyright 2021 American Chemical Society.*[113]*, (d), (e), (f) Reproduced with permission from Zibouche and Islam, ACS Applied Materials & Interfaces* ***12*** *(13), 15328-15337 (2020). Copyright 2020 American Chemical Society.*[119]

As the band-edges of halide perovskites are mostly formed by the inorganic metal halide interaction, one can presume that the *A*-site cations play a limited role on the optoelectronic properties. However, the final crystallographic structure and thermodynamic stability are heavily influenced by the choice of organic cation and reaction parameters, which indirectly influence the optoelectronic properties of the 2D layered structure. Firstly, by tuning with the thickness and composition of the organic layer, one can also alter the optoelectronic properties

of the layered structure. Moreover, smaller interlayer spacing, especially in eclipsed structures, lead to better electronic coupling between the perovskite layer and can promote a sizable band dispersion in the direction of reciprocal space corresponding to the stacking axis. Secondly, the organic spacer cation has a significant impact on the distortion of the metal halide octahedra due to the stress originating from the electrostatic and hydrogen-bonding interactions between organic and inorganic layers. In general, the octahedral distortion can be in-plane, out-of-plane, or deviated from ideal octahedra, depending on the charge density and tail group of the *A*-site cations (**Figure 12a, b, c**). As the organic cations usually have inhomogeneous charge density (higher in head and lower in tail group), the inorganic metal-halide layer tends to distort in-plane to compensate the charge density difference. An out-of-plane distortion can occur when there is a more sterically-demanding cationic headgroup, such as trimethylammonium, which is too large to accommodate. Further increases in bulkiness of the organic cation, such as in 2-BrPEA, 2-CF 3PEA, and 1-PYREA salts, can result in a combination of in-plane and out-of- plane distortions. In an early work, Mitzi and co-workers illustrated the role of distortion on the electronic structure 2D ($RNH_3)_2SnI_4$ (R = organic group) perovskites[108]. **Figure 12e** and **12f** shows the experimental exciton resonances and bandgap of Sn-based 2D iodide perovskites with functionalized aromatic moieties and ethylammonium against Sn–I–Sn bond angle respectively. As expected, the impact of in-plane distortion on bandgap (excitonic energy) is found to be more severe than an idealized out-of-plane distortion due to a greater loss of overlap between Sn and I orbitals. As the valence band comprises metal s and halide p antibonding orbitals, a decrease in the level of overlap would push the valence band downwards, while the conduction band remains nearly unchanged. In another study which involves pentane-diammonium (PeDA) and iPy as the organic cations, it was revealed that the larger bandgap of $(iPy)_2SnI_4$ was due to the large octahedral distortion, despite a reduced out-of-plane distortion[120]. Similar results were also obtained by substituting a functional group within the organic molecule. For example, the position of the fluorine substitution on the phenyl ring in $(C_6H_4FC_2H_4NH_3)_2SnI_4$ leads to an increase of the in-plane distortion for the ortho, meta, and para positions, increasing the optical bandgap[121]. The

conformation of the organic cation was further illustrated by substituting halide group in 2-substituted phenethylammonium cations, $(2\text{-}XC_6H_4C_2H_4NH_3)_2SnI_4$ (X = F, Cl, Br)[122]. Smaller halides such as F and Cl substitution leads to gauche conformation, like PEA, while Br substitution resulted in anti-conformation with larger in-plane distortion. Consequently, the excitation energy shifted towards higher energies in $(2\text{-BrPEA})_2SnI_4$ (2.23 eV) as compared to $(2\text{-ClPEA})_2SnI_4$ (2.12 eV) and $(2\text{-FPEA})_2SnI_4$ (2.11 eV).

However, a contradictory result was obtained in BA_2SnI_4 which showed larger optical bandgap at low-temperature (LT) as compared to room temperature (RT) phase, despite negligible in-plane distortion (26.4° (LT) *vs.* 21.3° (RT)) as compared to out-of-plane distortion (22.3° (RT) *vs.* 2.3° (LT)). The authors concluded the cooperative effect of two distortions should be taken into consideration simultaneously, as both occur at the same time. This conclusion was quantified by evaluating the overall Sn-I-Sn bond angle[123]. The octahedral distortion in the inorganic layer is found to decrease with increasing the length of the organic spacer cations due to the minimization of the stress transmitted to the inorganic layer. The observation that greater structural distortion or tilting occurs in inorganic octahedra is consistent with the notion that the surface closest to the organic spacer cation layer experiences more distortion/tilting than the middle layer. In addition to the organic cation, the optical bandgap of 2D halide perovskites also increases when exchanging iodine to bromine to chlorine, much like the 3D perovskites.

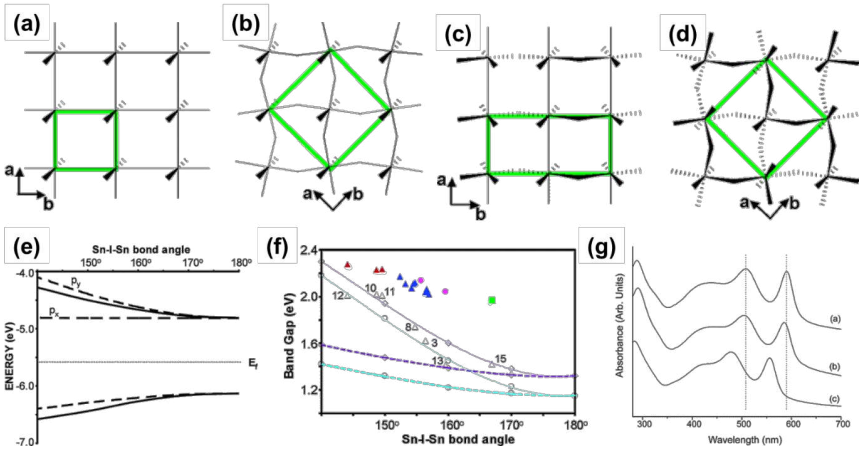

Figure 12. *Distortion in Sn-based low-dimensional structure. Schematic of 2D perovskite sheets which shows the (a) undistorted lattice, (b) in-plane distortion, (c) out-of-plane distortion, and (d) combined in- and out-of plane distortion. The green box highlights the unit cell that describes each lattice. (e) Plot of the energy of the top of the valence band (Sn s-based) and bottom of the conduction bands (Sn p_x- and p_y-based) upon in-plane (solid lines) and out-of-plane (dashed lines) distortions to the SnI_4^{2-} perovskite lattice (calculated with an average Sn−I distance of 3.16 Å) which demonstrates the origin of the band gap variation with structural distortion. The Fermi energy is marked by a dotted line. (f) Plot of the calculated band gap as a function of the in-plane (solid lines) and out-of-plane (dashed lines) distortions. Purple and blue lines represent calculations with average Sn−I distances of 3.16 and 3.14 Å, respectively. Open circles and diamonds represent calculated band gaps for idealized structures with Sn−I distances of 3.14 and 3.16 Å, respectively; open triangles represent calculated band gaps for experimental crystal structures (reference numbers are correlated with Table 1). Filled symbols represent the experimental exciton peak energies from Table 1 for the following systems: blue triangles for purely in-plane distortion and red triangles for combined in- and out-of-plane distortions (PEA derivatives* ***1−12****), purple circles for alkylammonium derivatives* ***13*** *and* ***14****, and green squares for TMAEA* ***15****. (g) (a)-(f)*

*Reproduced with permission from Knutson et al., Inorganic Chemistry **44** (13), 4699-4705 (2005). Copyright 2005 American Chemical Society.*[108]

The charge transport properties in this layered structure attracted a lot of interest from the beginning when 2D tin-based iodide perovskites exhibited semiconductor to metallic transition with increasing number of inorganic layers (*n*)[103, 124]. Later, it was revealed that the self-doping of Sn^{2+} is the most likely origin of high conductivity in low-dimensional structures, much like 3D THPs [120]. In general, due to the layered structure, 2D halide perovskites exhibit highly anisotropic charge transport behavior owing to large differences in charge transport properties between organic and inorganic molecules. Thus, with increasing number of inorganic layers (*n*), electrical conductivity, especially charge carrier mobility was found to increase in the perpendicular direction due to Coulombic shielding offered by the inorganic layer. Nevertheless, the exact mechanism by which the carriers tunnel through the inorganic layers remains unknown. This can be directly linked to the dispersion or width of VBM and CBM which shows a decrease of carrier effective mass with increasing inorganic layer number (*n*) as shown for $(CH_3(CH_2)_3NH_3)_2(CH_3NH_3)_{n-1}Sn_nI_{3n+1}$ (n = 1, 2 and 3) series[123]. As compared to 3D structures in which the charge carriers are considered to move through delocalized bands, the presence of continuum organic cations in low-dimensional structures essentially acts as barriers. Thus, nature of the organic cations and their orientation heavily influence the charge transport properties in low-dimensional structure. For example, diammonium cations or molecules having π-conjugation are expected to drastically improve the charge transport properties across the inorganic sheets due to smaller interlayer distance and ease of hopping[125]. Takahasi et al[120] studied several tin-based low-dimensional structures having monoammonium and diammonium cations in the *A*-site, and showed wide variations in the electrical resistivity. For example, the smallest cation butylammonium, having A_2SnI_4 structure, showed the lowest resistivity which is comparable with diammonium cation (C5di) having $ASnI_4$ structure. Nevertheless, structures having smaller valence bandwidths usually showed higher resistivity, indicating a decrease in carrier effective mass. Moreover, the close

proximity between layers in the DJ structure coupled with the organic molecules' high dielectric constant can enhance the dielectric screening effect, thereby reducing the quantum confinement of charge carriers.

3.2.2 Transition metal-based low-dimensional structure:

While Sn- and Ge-based low-dimensional perovskite structures receive the most attention, transition metal-based 2D halide perovskites, with a general formula of $A_{n+1}B_nX_{3n+1}$ with A= Cs^+, Rb^+, K^+ ,organo-ammonium cation etc; B = Cd^{2+}, Mn^{2+}, Fe^{2+}, Cu^{2+}, Hg^{2+}, Zn^{2+}, Co^{2+} etc., X= Cl^-, Br^- and n denotes the number of inorganic layers, are also well-studied for their magnetic properties[126-129]. The simplest structure is A_2BX_4 (n = 1), which adopts either K_2NiF_4 (space group $I4/mmm$)[130] or $TlAlF_4$ (space group $P4/mmm$)[131] structure, depending on the ionic radius. These magnetic materials crystallize in a tetragonal structure, and usually have indirect band gaps with very flat bands, which usually results in poor charge transport properties. However, many of these compounds exhibit symmetry-altering phase transitions upon temperature change. The most studied compounds of this class are Cu- and Fe-based halide perovskites due to the presence of Jahn-Teller (JT) active metal cations and stereo-active lone pairs, leading to unusual physical phenomena such as piezochromism[132], ferro- to anti-ferromagnetic transformation[126, 133, 134], ferroelectricity under pressure and temperature[134-136]. The JT distortion, which originates from Cu $3d^9$ electronic configuration, produces in-plane distortion of the corner-sharing copper halide octahedra (**Figure 13a**), and consequently poor overlap between copper-derived half-filled orbitals. Application of isostatic pressure has been demonstrated to reduce the orbital orthogonality (in-plane distortion) in A_2CuX_4 compounds, leading to better orbital overlap[137]. **Figure 13b, c** shows the evolution of $[CuCl_6]^{4-}$ octahedral under isostatic pressure in $(EDBE)[CuCl_4]_4$. The optical absorption spectra of $(EDBE)_2[CuCl_4]_4$ exhibited a red-shift with both temperature and pressure, resulting in thermochromism and piezochromism, respectively (**Figure 13d**). Electronic structure calculations revealed that the origin of thermochromism is the broadening of conduction band states, while piezochromism is due to reduction of JT and tilting of octahedra[132]. Additionally, electrical conductivity was shown to increase at least by five orders of magnitude in $(EA)_2CuBr_4$ compounds under

moderate pressure, suggesting that high pressure can dramatically improve the *d*-orbital overlap through octahedral tilting and Cu—Cl bond shortening[138]. One instance is $(C_2H_5NH_3)_2[Fe^{II}Cl_4]$ which undergoes a series of phase transition from tetragonal to orthorhombic to monoclinic (*I*4/*mmm* ↔ $P4_2/ncm$ ↔ *Pccn* ↔ *Pcab* ↔ *C*2/*c*) as temperature is reduced from 383 K to 10 K. These transitions were accompanied by both tilting and rotation of the $[FeCl_6]$ octahedra[133]. The compound displayed promising multiferroicity and giant hysteresis at low temperatures, making it one of the hardest known molecular magnets.

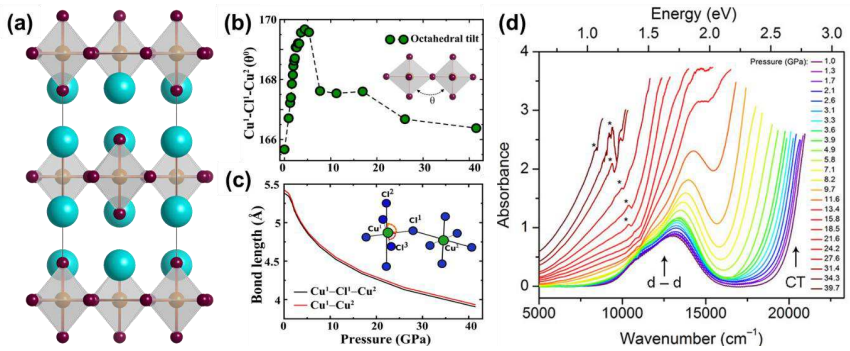

Figure 13: *(a) Polyhedral model of Cs_2CuCl_4 crystal structure. (b) Octahedral tilt angle as a function of pressure. (c) Variation of Cu^1–Cu^2 bond length and Cu^1–Cl^1–Cu^2, i.e., (Cu^1–Cl^1) + (Cl^1–Cu^2) with pressure. (Inset in c) Various bond lengths, where Cu^1–Cl^1 is the equatorial (eq) bond and Cl^1–Cu^2 is the axial bond. (d) Variable-pressure absorption spectra for **1** using visible and infrared (IR) wavelengths showing the crystal field (d–d) and ligand-to-metal charge transfer (CT) transitions. Asterisks indicate a detector change between visible and IR wavelengths. d–d transitions and CT transitions are shown as blue and red arrows, respectively, in the orbital energy diagrams for D_{4h} and O_h symmetry. Both symmetry allowed and forbidden transitions are shown. (Figure b), (c) Reproduced with permission from Gupta et al., Inorganic Chemistry **55** (13), 6817-6824 (2016). Copyright 2016 American Chemical Society.[132], (d) Reproduced with permission from Jaffe et al., Journal of the American Chemical Society **137** (4), 1673-1678 (2015). Copyright 2015 American Chemical Society.[138]*

3.2.3 2D double perovskite:

Apart from divalent metal-based layered structure, 2D analogues of double perovskites have also received a lot of attention recently. The recent development of low-dimensional halide double perovskites was catalysed by a report from Connor et al.[139], who demonstrated dimensionality reduction of the 3D $Cs_2AgBiBr_6$ by incorporating BA to achieve $(BA)_4AgBiBr_8$ (n = 1) and $(BA)_2CsAgBiBr_7$ (n = 2) layered structure. As there are fewer geometric constraints over *A*-site cation size for forming layered structures, a plethora of novel low-dimensional halide double perovskites have been synthesized, even with compositions that are known to be unstable in 3D crystal structures. For example, pure iodide-based double perovskites are rare due to unfavourable tolerance factor and higher stability of the competing phase[83]. However, several 2D iodide double perovskites have been synthesized, such as $(AE2T)_2AgBiI_8$ [140], $(IPA)_4AgBiI_8$ [141], $(AMP)_4[BiAgI_8]_2{\cdot}H_2O$, and $(APP)_4[BiAgI_8]{\cdot}H_2O$ (where AE2T = 5,5-diylbis(amino-ethyl)-[2,20-bithiophene], IPA = 3-iodopropylammmonium, AMP = 4-aminomethylpiperidinium, APP = 4-aminopiperidine). This increased stability window, especially in the case of iodides, is related to the higher templating capacity of the organic cation as compared to that pure inorganic compositions which are most likely to form low-dimensional ternary structures. More interestingly, fewer geometric restrictions also offers highly distorted and tilted $[B^{n+}X_6]^{n-6}$ octahedral units achieving a more stable configuration. For example, monovalent Cu-based 3D double perovskites is highly unlikely due to the preference of Cu^+ for three or four-fold coordination, but several examples of Cu^+-based 2D halide double perovskites have recently emerged where Cu^+ adopts extremely distorted octahedral coordination[142, 143].

Despite the templating effect by the organic cations, the optoelectronic properties of these low-dimensional double perovskites mostly dominated by the metal and halide composition. For example, $(BA)_4AgBiBr_8$ (n = 1), $(BA)_2CsAgBiBr_7$ (n = 2), and the 3D parent $Cs_2AgBiBr_6$ possess band gaps of ≈2.6 eV, ≈2.4 eV, and ≈2.2 eV, respectively, which is less significant modification as compared to the dimensionality engineering in divalent metal cation-based structures[139]. Even varying the organic cation has little impact on the bandgap tunability. For

example, $A_n AgBiBr_8$ (n = 2 or 4) (A = PA, BA, octylammonium (OCA), and butyldiammonium (BDA) exhibit similar band gaps in the range of 2.41 to 2.45 eV[144]. In a similar vein, Bi et al.[143] investigated several $A_n CuBiI_8$ (n = 2 or 4) compositions containing various organic cations and found that the band gap values of these materials fall within a narrow range of 1.55 eV to 1.65 eV. A noteworthy observation from both studies is that materials with greater interlayer distances and higher octahedral distortion typically exhibit slightly larger band gaps, which is similar to the behavior of Pb- or Sn-based 2D systems.

That said, a wide range of property tunability is possible for *B*-site cation engineering with bandgaps spanning a remarkable range of 1.14 eV to 4.27 eV, depending on the choice of halide. As expected, the bandgaps are smallest and largest for iodide and chloride materials, respectively. Among various monovalent cations at B-site, the smallest bandgap is offered by Au-based perovskites, followed by Cu- and Ag-based compounds due to presence of intervalence charge transfer in the former and presence of d-orbitals in the Cu-based compounds. The band gap varies with trivalent cations as Bi < Sb ≪ In with indium-containing compounds exhibit largest bandgaps due to the change in electron configuration, $4d^{10}5s^0$ for In^{3+} vs $(n-1)d^{10}ns^2np^0$ for Sb^{3+} and Bi^{3+}. The smaller bandgaps in Bi-based compounds are also expected due to larger relativistic effect as compared to that of Sb-based compounds [139, 145]. A particularly interesting case of hybrid low-dimensional perovskite is the mixed valence: $[NH_3(CH_2)_8NH_3]_2[(Au^+I_2)(Au^{3+}I_4)(I_3)_2]$ and $NH_3(CH_2)_7NH_3]_2[(AuAu^{3+}I_2)(Au^{3+}I_4)(I_3)_2]$ which even exhibits smaller bandgaps than 3D analogues[146]. This narrowing of the bandgaps can potentially be explained by the incorporation of I_3^- in the low-dimensional structure. Another hybrid material that has been reported recently is $(IPA)_4AgBiI_8$, which has iodide as its primary component. The interlayer cation in this material is IPA, which was initially 3-bromopropylammonium but underwent an in-situ reaction with hydroiodic acid to become 3-iodipropylammonium. This reaction resulted in a narrow-direct bandgap of 1.87 eV in the layered double perovskites[141].

Nevertheless, the nature of bandgaps in these series of low-dimensional structure remains elusive. For example, electronic structure shows an indirect bandgap of $Cs_2AgBiBr_6$, whereas $n = 1$ $(BA)_4AgBiBr_8$ has a direct band gap[139], a trend which is markedly different in comparison with Sn-based low-dimensional perovskite structures. This change from indirect to direct bandgap is attributed to a reduction in dimensionality. Moreover, the nature of bandgap in $(AE2T)_2AgBiI_8$ is calculated to be indirect without spin-orbit coupling (SOC) effect, but changes to direct when SOC is considered[140]. In contrast, recent reports also predict a direct bandgap for $(PEA)_2CsAgTlBr_7$ (PEA = phenethylammonium), which is similar to the 3D double perovskite $Cs_2AgTlBr_6$ [147]. The bandgap of the $n = 1$ compound, on the other hand, was found to be indirect, originating from Ag-to-Tl metal charge transfer. On a separate note, hybrid low-dimensional halide double perovskites generally have flatter bands which pose difficulty in accurately determining the nature of bandgap. Despite this, empirical and theoretical findings suggest that the type of bandgap is considerably influenced by factors such as the composition, layer thickness, and the degree of local structural distortion. Thus, it is crucial to conduct meticulous theoretical investigations before drawing conclusions about the trend based solely on the 3D parent material or the reduction in dimensionality.

3.2.4 (110) and (111)-oriented 2D structure

Apart from (100) orientation, low-dimensional perovskite structures also consist of corrugated (110) and (111) oriented inorganic layers, although these are quite rare as small and highly symmetric cations are required to stabilize them[148-150]. As shown in **Figure 14b**, corrugated (110)-oriented structures can be described by the missing metal octahedra in <110> direction. Each layer expands through the corner-connected metal halide octahedra which can be seen as a zigzag pattern from the other direction. Both monoamine and diamine cations can be incorporated at *A*-site to form (110)-oriented 2D perovskite structure, adopting a general formula of $AA'BX_4$ (*A* and *A'* can be same or different monoamine cation) or $A^{2+}BX_4$ (*A* is a diammonium cation). An early known example of this structure is the $[NH_2C(I):NH_2]_2(CH_3NH_3)_nSn_nI3_{n+2}$ series[124] in which the open octahedral voids formed by the undulated layers contain smaller $(CH_3NH_3)^+$ cations, while the large organic cation

$(NH_2C(I):NH_2)^+$ sits inside the interlayer spacing. Other known examples includes iodoformamidinium tin iodide $[NH_2C(I):NH_2]_3SnI_5$ [151], $(Gu)_{1.5}(Me\text{-}ImH)_{0.5}SnI_4$ (Gu = guanidinium, Me-ImH$^+$ = 1-methylimidazolium)[152], α-$[NH_3(CH_2)_5NH_3]SnI_4$ [148], and Gu_2SnI_4 [149]. In the last example, the guanidium cation occupies both *A* and *A'*-site in the (110) oriented 2D structure[16]. Perovskite layers with a (110) orientation are inherently distorted, and they are typically stabilized by secondary bonding interactions involving hydrogen or other elements. Consequently, these (110)-oriented perovskites often emit white light at room temperature due to the formation of self-trapped excitons (STEs).

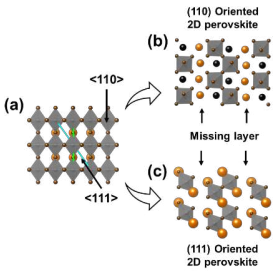

Figure 14. *Schematic illustration of the cleaving plane in aristotype perovskites to form (110) and (111) oriented 2D layered structure. Arrows in Figure (a) indicate the cleaving planes, whereas Figure (b) and Figure (c) show the final crystal structure of the (110)- and (111)-oriented 2D crystal structures. Missing octahedral layers in Figures (b) and (c) are shown by arrows.*

On the other hand, there are no reports on divalent metal cation based (111)-oriented 2D halide perovskites. Unlike the rest of the layered perovskite configurations, (111)-oriented perovskites are essentially vacancy-ordered structures in which a metal octahedra layer is missing in each third layer (n =2) (**Figure 14c**), which necessitates the central metal cation to be in the +3 oxidation state to maintain the charge balance with the halides. Hence, trivalent cations remain the most ideal candidates to form (111)-oriented 2D halide perovskites having the formula of $A_3B^{+3}{}_2X_9$ (B = Cr^{3+}, As^{3+}, Sb^{3+}, Bi^{3+}, In^{3+})[153-156]. It should be noted here that the

same formula unit can also be used to describe 0D variants of those compounds which we will discuss later under perovskite-derivative structures. A smaller *A*-site cation and smaller halides favor the formation of (111)-oriented structures whereas a combination of larger *A*-site cation along with larger halides promote the formation of 0D structures. For example, $Cs_3Sb_2I_9$ prefers to crystallize into zero-dimensional dimer structure, whereas Rb-analogous are easily stabilized into (111)-oriented 2D structure[157]. Additionally, zero-dimensional $Cs_3Sb_2I_9$ can be converted to (111)-oriented 2D structure by substituting iodide with smaller halides, such as bromide or chloride[158, 159]. While the electronic structures of these compounds are governed by the *B*-site cations and halides, the optoelectronic properties of these two polymorphs differ significantly with typically direct bandgaps in (111)-oriented 2D structures and indirect bandgaps for 0D structure owing to superior connectivity of the octahedra in the former. For the same reason, the optoelectronic properties are also nearly identical for different *A*-site cations for same crystallographic structure. Typically, iodide-based compounds have direct bandgaps of around 2 eV with Bi-based compounds generally having slightly smaller bandgaps (due to larger relativistic effect) compared to Sb-based compounds. The smallest bandgap that has been reported with (111)-oriented 2D (n=2) is around 2 eV in $(NH_4)_3Bi_2I_9$, which is still quite larger than the optimal values required for photovoltaics[156]. On the other hand, bromide and chloride analogues exhibit much wider bandgaps of 2.6 – 3.0 eV. We should note here that $CsBi_3I_{10}$ is claimed to have a layered structure with a bandgap of 1.77 eV. Nevertheless, there is no single crystal data to confirm the structure as of now[160]. In direct comparison, 2D layered structure always offer better optoelectronic properties as compared to 0D dimer structure, at least in terms of charge transport, excitonic binding energy, and radiative recombination. Additionally, the effective mass of $A_3B_2X_9$ layered structures can be further reduced along certain crystallographic orientations by tuning *A*-site or *X*-site ions.

By mixing these vacancy-ordered structures, the library of perovskite-derivative compounds can be extended to many different formulas, such as $A_4B^{3+}B^{+5}X_{12}$, and $A_4B^{2+}B^{3+}{}_2X_{12}$. For example, incorporating Mn^{2+} with $Cs_3Bi_2Cl_9$ structure leads to heterometallic $Cs_4MnBi_2Cl_{12}$

($A_4BC_2\square X_{12}$) vacancy-ordered triple perovskite, having 25% lower vacancies than the parent $A_3B_2X_9$ structure. In this arrangement, both Bi^{3+} and Mn^{2+} cations are bonded to six Cl^- ions to generate two distinct types of octahedral blocking units. These units are organized into a triple-layered 2D structure in which a layer of $[MnCl_6]^{4-}$ octahedra is sandwiched between two layers of $[BiCl_6]^{3-}$ octahedra. The $[MnCl_6]^{4-}$ layer is held in place by sharing corners with the adjacent [BiCl6]3- layers.. Likewise, (111)-oriented (n=3) crystal structure can be formed by intercalating Cu^{2+} [161] and Mn^{2+} [162] cations in 2D (n=2) $Cs_3Sb_2Cl_9$ [161, 162]. As shown in **Figure 15a**, **b**, (111)-oriented 2D (n=3) structure consists of alternating, corner sharing $[M^{2+}Cl_6]^{4-}$ and $[SbCl_6]^{3-}$ octahedra with Cs^+ occupying the voids in the framework, thus forming n=3 layer with the chemical formula of $Cs_4MSb_2Cl_{12}$ (M = Cu^{2+}, Mn^{2+}). Interestingly, $Cs_4CuSb_2Cl_{12}$ exhibited an optical bandgap of 1.0 eV as compared to 3.0 eV of the parent n=2 $Cs_3Sb_2Cl_9$ phase or n=3 $Cs_3MnSb_2Cl_{12}$. This is a classic example of Jahn-Teller distortion originating from d^9 configuration Cu^{2+} cations. As shown in **Figure 15d, e**, the presence of highly localized mid-bandgap states originating from Cu d orbitals is the most likely reason for low bandgap in Cu-based compounds as compared to Mn-based compounds. However, this also implies a low density of states close to the band edge, which may reduce the probability of electronic transitions drastically. (111)-oriented 2D structure can also be formed by multivalence state of Sb such as $Cs_4Sb^{3+}Sb^{5+}Cl_{12}$ which was reported back in 1960s, and later, $Rb_4Sb^{3+}Sb^{5+}X_{12}$ as an analogous structure. The $[Sb^{3+}Br_6]^{3-}$ and $[Sb^{5+}Br_6]^{1-}$ octahedra are both distorted from O_h symmetry and have D_{4h} symmetry. Notably, these compounds exhibit an unusual dark coloration, suggesting that they possess strong visible light absorption capabilities. This light absorption is attributed to electron transfer from the $[Sb^{3+}X_6]^{3-}$ octahedra to $[Sb^{5+}X_6]^{1-}$ octahedra, which is facilitated by van der Waals interactions involving the halogens and/or cations.

The $Cs_4BB'_2X_{12}$ family has been the subject of both experimental and theoretical investigations regarding their optoelectronic properties. For instance, one recent study on $Cs_{n+3}B_{n+2}Sb_2I_{3n+9}$ (B = Sn, Ge) compositions[163] found that presence of $[SnI_6]$ or $[GeI_6]$ octahedral layers between

$[Sb_2I_9]$ bilayers promote better optoelectronic properties including smaller band gaps and effective mass, larger dielectric constants, lower exciton binding energies, and higher optical absorption when compared to the pristine compound ($Cs_3Sb_2I_9$). The thickness of the inserted octahedral layers ($[BX_6]$) can be further tuned to optimize the band gaps and effective mass across a wide range. The larger optical bandgaps of these series of compositions prompted another theoretical study for the new transparent conductors. Among 54 potential compositions (B^{2+} = Mg^{2+}, Ca^{2+}, Sr^{2+}, Zn^{2+}, Cd^{2+}, Sn^{2+}; B^{3+} = Sb^{3+}, In^{3+}, Bi^{3+}; X = Cl^-, Br^-, I^-), seven compounds were predicted to have ideal properties for p-type transparent conductors, with $Cs_4CdSb_2Cl_{12}$ showing particular promise[164]. A subsequent study by Hu et al[165] suggests that these optically transparent compounds are probably electrically insulating, which contradicts the earlier findings. While computational research in this field persists[166], it is evident that further advances are needed on the experimental front.

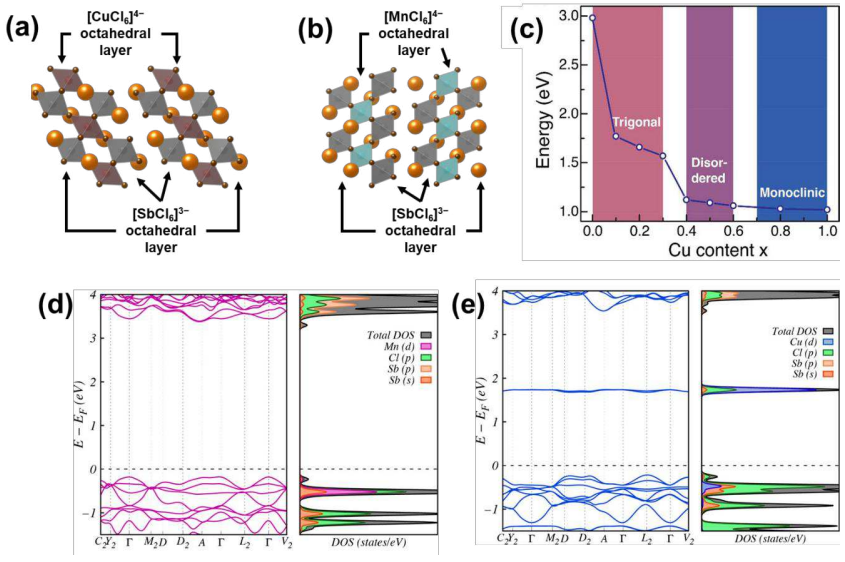

Figure 15. *(a),(b) Polyhedral model of (111)-oriented 2D (n=3) structure consists of alternating, corner sharing $[M^{2+}Cl_6]^{4-}$ and $[SbCl_6]^{3-}$ octahedra with Cs^+ occupying the voids in the framework, thus forming n=3 layer. (c) Optical bandgaps for $Cs_4Mn_{1-x}Cu_xSb_2Cl_{12}$ as a*

*function of copper concentration. The pink, purple, and blue shaded areas highlight the crystalline phases obtained for a given composition. DFT-calculated band structure diagram, total density of states, and partial density of states (DOS/pDOS) of (d) $Cs_4MnSb_2Cl_{12}$ and (e) $Cs_4CuSb_2Cl_{12}$ (c), (d), (e) Reproduced with permission from Vargas et al., Chemistry of Materials **30** (15), 5315-5321 (2018). Copyright 2018 American Chemical Society.*[162]

3.3 1D perovskite structure:

In contrast to 2D halide perovskites in which the octahedral network propagates in a 2D plane, the metal halide octahedron ($[B^{n+}X_6]^{n-6}$) can also be connected to each other via terminal halogen bridging to form an infinite array of 1D octahedral chains, separated by single or multiple *A*-site cations. The metal halide octahedron can be connected to each other either via trans- or cis-vertices, forming linear or zigzag chain of $(BX_5)_\infty$ respectively (**Figure 16a**). A classic example of the linear 1D structure is the end member of the (110)-oriented $[NH_2C(I)NH_2]_2A_mSn_mI_{3m+2}$ 2D series[167]. When m=1, the 1D perovskite system can be expressed as $[NH_2C(I)NH_2]_2ASnI_5$ (A = $NH_2C(I)NH_2^+$ or $NH_2CHNH_2^+$) in which each $[SnI_6]^{4-}$ octahedron share opposite corners to form nearly linear 1D chains of $[SnI_5]_n^{3n-}$ extending down the crystallographic *a*-axis. The *A*-site cations lie between the chains while iodoformamidinium (IFO) cations separate the chains horizontally. While there are fewer constraints for the size of the interlayer organic cations for forming 1D structures, trans-connected 1D perovskite chains are known for only one case of each Sn^{2+} and Cu^{2+} cation (excluding lead and fluoride compounds). A Cambridge Structural Database survey, carried out on the CSD version 5.43, indicates only fewer than 10 entries containing $[BX_5]^{n-}{}_\infty$ chains where B is the divalent cation (4 Mn-based, 1 Fe-based, 1 Cu-based, 2 Sn-based).

1D perovskite structures, on the other hand, are more common for trivalent metal cations such as Bi^{3+} and Sb^{3+} based halide perovskites, adopting a general formula of A_2BX_5 (*A* is monoamine) or ABX_5 (*A* is diamine)[168-173]. As these ions are weakly bonded to outer *s* electrons and easily polarizable, a great degree of distortion and aggregation of the $[B^{3+}X_5]_n^{2-}$ chain can be observed. Moreover, the covalency of Bi and Sb halide bonds exhibit low-

directional-correlations which promote a much higher tendency to form novel metalate halide structures such as these 1D chains. Both cis- and trans-connected structural motifs are observed in these trivalent metal cation-based halide perovskites. In the most common case, especially for iodides, $[BX_6]^{3+}$ are connected via cis-halogen bridging, thus forming zigzag octahedral chains. In the ideal structure, the *B*−*X*−*B* bridges lay in the plane of *B* atoms (180°), however, often the structure is distorted (140°-150°) depending on the interaction with the organic cations. Additionally, a special case can arise when the zigzag segments can also be built from three octahedra instead of two, a unique feature similar to 2D halide perovskites[174]. The $[BX_6]^{3+}$ units can also form a straight octahedral chain (trans-connected) which is most common in chloride and bromides.

Intriguingly, the 1D structures often feature inorganic motifs that create a van der Waals gap or galley, presenting an opportunity for excess organic cations or foreign molecules to intercalate. Zaleski and Pietraszko[175] explored intercalated structures in $Gu_2SbCl_5{\cdot}GuCl$, in which the anionic sublattice comprises of a 1D chain of $[SbCl_5^{2-}]_n$ and isolated chlorine atoms. The chains consist of distorted $[SbCl_6]^{3-}$ octahedra connected at corners which align along the crystallographic c-direction to form elongated cavities where the isolated chlorine ions reside. The guanidinium cations are linked to chlorine atoms through hydrogen bonds in the cavities created by polyanionic chains (**Figure 16c**).

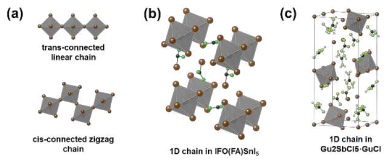

***Figure 16**. 1D perovskite structure. (a) Polyhedral model of cis-connected zigzag and trans-connected linear octahedral chain. (b) Polyhedral model of 1D perovskite crystal structure (IFO(FA)SnI5). (c) 1D perovskite crystal structure (Gu2SbCl5) featuring excess cation (Gu) in van der Waals galley (hydrogen atoms are omitted, and carbon and nitrogen atoms are shown in black and green respectively).*

Currently, there are no strict guidelines for selecting suitable bulky cations for the formation of 1D perovskite chains, although several trends can be observed from the reported literature. First, 1D chains with heavier halides are all hybrid structures (all inorganic 1D chains exclusively form with fluorides) owing to easily deformable perovskite chains and higher degrees of freedom. Another structural requirement is the shape and size of the organic cations as these molecules not only accommodate themselves within the inorganic framework, but they should also provide adequate structure rigidity for 1D octahedral chains. Additionally, primary (H···*X*) hydrogen-bonding, which is an important parameter for 2D perovskite structure formation, cannot determine the 1D structure alone as the close-packing of the metal halide complex is also apparently important and the optimal structures are believed to arise when there is a harmonious interplay between these two factors[176]. Cariati et al investigated the crystal structure of $[bzpipn]_2[BX_5]$ and $[bzpipzn][BX_5]$ (bzpipn = 4-benzylpiperidinium cation, bzpipzn = N-benzylpiperazinium dication; *B* = Sb or Bi; *X* = Cl or Br) to observe the effect of hydrogen bonding as 4-benzylpiperidinium and N-benzylpiperazinium cations have similar dimensions[172]. Based on the vibrational spectra of these compounds, the molecular structures of the complexes were found to depend more on the halogen atoms rather than on the counter-cation dimensions and hydrogen-bonding abilities. Furthermore, the lattice energy of crystal structures can be dominated by electrostatic interactions, which can outweigh the effects of local hydrogen bonding. This results in molecular packing that appears to be primarily influenced by shape complementarity and Coulombic forces.

While the earlier studies were focused on the crystal structure of these polymeric chains, recent successes of halide perovskites have led to reasonable attention on these 1D structure for optoelectronic applications. Earlier, Mitzi and co-workers discovered that 1D structures, $[NH_2C(I)NH_2]_2ASnI_5$ (*A* = $NH_2C(I)NH_2^+$ or $NH_2CHNH_2^+$), possess higher bandgaps and are electrically insulating when compared to semiconducting 2D ($m \geq 2$) and conducting 3D perovskite structures ($m \rightarrow \infty$)[167]. This outcome is anticipated due to stronger dielectric confinement within 1D structure. However, the dielectric confinement can be reduced by

implementing organic cations with higher electron affinity. A case in point is the zigzag chain structure of (naphthalimide ethylammonium)$_2$BiI$_5$ (NBI), where the high electron affinity of naphthalimide creates a type-IIa band alignment at the organic-inorganic heterojunction, overcoming the charge transfer bottleneck[177]. This heterojunction structure leads to the efficient separation of electron-hole pairs and longer excited state carrier lifetimes. Unfortunately, anisotropic electrical properties also observed in NBI single crystals of NBI along the directional growth of $[BiI_5^{2-}]_n$ inorganic chains. Another approach to reducing dielectric confinement is to use a diammonium cation that can also participate in charge transport and optoelectronic properties. (TMP)[BiX_5] (TMP = N,N,N′,N′-tetramethylpiperazine) is a noteworthy example of this type. The compound features alternating layers of inorganic $[BiI_5]_n^{2n-}$ chains and $(TMP)^{2+}$ cations along the b axis. The inorganic layers consist of a 1D array of $[BiI_5]_n^{2n-}$ chains that extend along the [011] direction of the structure[168]. The twist in the zigzag structure was found to increase monotonically from iodide to chloride structure, resulting in significant structural changes. The optical band gaps, as calculated from reflectance spectra, were determined as 2.02, 2.67, 3.21 eV for iodide, bromide, and chloride respectively. Additionally, octahedral distortion is also found to control the optoelectronic properties significantly. For example, $[NH_2C(I)NH_2]_2ASnI_5$ (A = $NH_2C(I)NH_2^+$ or $NH_2CHNH_2^+$) exhibit similar building blocks for both *A*-site cations, However, the large iododformamidinium cation (A = $NH_2C(I)NH_2^+$) induces larger distortions as compared to formamidinium cation which reflects in their corresponding color (orange yellow for A = iodoformamidinium and dark red for A = formamidinium)).

In general, the 1D structures can be an excellent model for self-trapped excitons as they are easily deformable under photoexcitation due to greater vibrational degrees of freedom, which enhances the self-trapping of excitons[178]. 1D quantum wire perovskites have already shown excellent potential in various applications including ferroelectrics, LEDs, super-lattice heterojunction devices, lasers, and light harvesting, in particular, 1D nanowire structures show directional propagation of hole, electron, or photon that could enable improved device

performances in certain directions[179, 180]. However, in-depth investigations of optoelectronic properties in 1D perovskite crystal structures are still scarce.

3.4 0D perovskite structure:

Another vacancy-ordered low-dimensional structure is formed by tetravalent metal cations with the general formula of $A_2B^{4+}X_6$, popularly known as K_2PtCl_6-type (antifluorite) structure, or 0D perovskites. These structures are crystallographically identical to double perovskites, having one of the *B*-site cations is partially replaced by a vacancy (at a ratio of 1:1), resulting in isolated metal halide octahedra. Nevertheless, the close-packed anionic lattice structure is still retained (**Figure 17a, b, c**). This type of structure has been well-known for a long time, along with their symmetry-lowering phase transition at low temperatures[181]. Earlier studies focused on their applications as diamagnetic hosts for paramagnetic ions (Ir^{4+}, Re^{4+}, Os^{4+}) [182], scintillation and gamma-ray spectroscopy[183]. According to Brown[184], the structure type of A_2BX_6 compounds mainly depends on the ratio of the ionic radius of the *A* cation and that of the hole (gap) inside the BX_6 lattice. As the size of the A cation decreases, the crystal structure of A_2BX_6 compounds distorts from cubic to tetragonal or lower symmetry. If the ratio is greater than 0.98 (as in Panichiite), a cubic structure is observed at any temperature. However, for ratios between 0.89 and 0.98 (such as in K_2SnCl_6), the structure is cubic at room temperature but transforms to a lower symmetry at lower temperatures. Over 30 different metal cations have been incorporated as *B*-site cations in A_2BX_6 structures, and hundreds of compositions have been synthesized and characterized so far[182, 185]. A number of these compounds exhibit symmetry-lowering octahedral rotations and tilting as a result of over- or undersized *A*-site cations [184] and stereo-chemical activity of *B*-site cations[186]. While the earlier studies were mostly focused on rare-earth and third-row transition metals as *B*-site cations, their recent revival of interest originates from unusual optoelectronic properties exhibited by Cs_2SnI_6 which is an undesired degradation product of $CsSnI_3$. Despite having isolated octahedra, initial reports indicated strong absorption in the visible range (direct bandgap of 1.3 eV), extremely high charge carrier mobility (310 $cm^2V^{-1}S^{-1}$), and superior air-stability of Cs_2SnI_6 as compared

to parent $CsSnI_3$, making it an extremely promising material for photovoltaic applications[35, 187, 188]. While subsequent investigations reported many contrasting results regarding the optical bandgap (1.3–1.6 eV) and mobilities (1–310 $cm^2V^{-1}S^{-1}$), which were found to be highly dependent on the process history and characterization techniques employed[153, 189, 190], the reasonably smaller bandgap and unusually high carrier mobility still sparked a lot of interest. DFT-based electronic structure calculations revealed heavy effective mass of electrons and holes which is expected due to the low-dimensional crystal structure. However, the close-packed halide lattice can still offer reasonable charge transport across the lattice. Additionally, the presence of defects such as iodine/tin vacancies can also be abundant depending on the process history and the defects can have huge role in charge transport as previously observed for low-dimensional Sn^{2+}–based compounds. Hence, several hypotheses for high mobility have been suggested such as surface-mediated charge states[191], presence of defects such as iodine vacancies[192] and impurity phases such as $CsSnI_3$.

The optical bandgap, on the other hand, could be influenced by the measurement techniques employed; for example, diffuse reflectance spectroscopy is more sensitive towards sub-bandgap states which would most likely indicate a smaller bandgap[190]. Similar to other halide perovskites, optoelectronic properties of vacancy-ordered A_2BX_6 are mostly determined by the electronic states of *B*- and *X*-site ions. Thus, tuning of bandgap is also possible by alloying with bromine and chlorides which widens the bandgap, following a linear relationship. **Figure 17d** shows the computed bandgap of the A_2BX_6 structure. Experimental studies agree well with the trends in the bandgap variation such as in $Cs_2SnI_{6-x}Br_x$ and $Cs_2SnI_{6-x}Cl_x$ series. Similar results are also predicted with Ge-based analogous $Cs_2GeCl_2I_4$, $Cs_2GeBr_2I_4$, $Cs_2GeI_2Br_4$ [193]. The magnitude and nature of bandgap (direct vs indirect) is often determined by the *B*-site and halide ions. For example, Cs_2SnI_6 possesses a direct bandgap, whereas replacing Sn with Te at the *B*-site yields comparatively larger indirect bandgap. Several other $A_2B^{4+}X_6$ structures with *B* = Pd, Pt, and Ti show promising optoelectronic properties with optical bandgap in the visible range, long photoluminescence lifetime, and dispersive electronic

bands. For example, the bandgap of Cs_2TiX_6 (X = Br, I) can be continuously varied from 1.02 to 1.78 eV by partially replacing iodine with bromine[194]. However, their application on optoelectronic devices remains questionable due to issues on both their stability and their ability to efficiently harvest light.

The nature of defects or impurities is yet to be fully understood, as DFT-based calculations often produced contrasting results. Moreover, there is still a debate regarding the true valence of Sn in the compound, as some computational works suggest that it is +2 [195]. Nevertheless, electronic structure calculations are in agreement that the I 5*p* non-bonding states form the VBM in Cs_2SnI_6, while the CBM arises from the anti-bonding state resulting from the hybridization of Sn 5*s* and I 5*p* orbitals. Tin vacancies are predicted to form at energies similar to those related to the Sn-I antibonding orbitals, akin to $CsSnI_3$, and therefore at a transition level within the bandgap but in proximity to the CBM. Additionally, due to the smaller bandgap, iodine vacancies are predicted to be shallow in nature. Interestingly, when Sn is replaced by homovalent Te or Ti, the defect tolerance is lost[196]. The larger bandgap in Cs_2TeI_6 arises from the covalent interaction of Te 5*p* states with I 5*p* states, which pushes the conduction band to higher energies. As a result, the I vacancy becomes a deep-level state (**Figure 17e**). On the other hand, the defect intolerance of Cs_2TiI_6 is attributed to the large number of possible oxidation states and relatively localized d-electronic states.

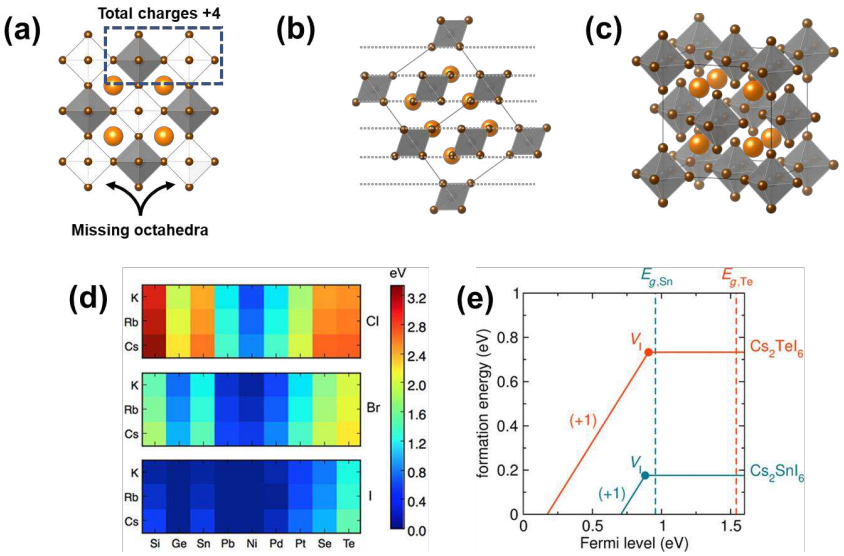

Figure 17. *Polyhedral model of zero-dimensional perovskite structure, illustrating (a) alternating arrangement of missing octahedra and tetravalent metal halide octahedra, (b) octahedral arrangement shows how the cubic packed iodine sub lattice is decorated with Sn atoms to yield the isolated octahedral units (c) isotropic diagram. (d) Color map of PBE-GGA calculated band gaps for 81 A_2BX_6 compounds in the cubic ($Fm\bar{3}m$) structure, with A = K, Rb, Cs; B = Si, Ge, Sn, Pb, Ni, Pd, Pt, Se, Te; and X = Cl, Br, I. The three large blocks respond to Cl, Br, and I compound, respectively. (e) Formation energies for iodine vacancies in Cs_2SnI_6 (teal) and Cs_2TeI_6 (red), under tin/tellurium-poor conditions. Sloped lines indicate the +1 charge state, and the solid dots represent the transitions levels $\epsilon(q/q')$. The dashed lines represent the fundamental band gap of each material. (d) Reproduced with permission from Cai et al., Chem. Mater. 29 (18), 7740-7749 (2017). Copyright 2016 American Chemical Society. (e) Reproduced with permission from Maughan et al., Journal of the American Chemical Society* ***138*** *(27), 8453-8464 (2016). Copyright 2016 American Chemical Society, under a Creative Commons Attribution 4.0 International (CC-BY) License.*[196]

A unique feature of this class of compounds is their isolated octahedra, resulting in quantum confinement, which is potentially beneficial for light emission applications. The photoluminescence of these compounds can be further enhanced by doping, which has been demonstrated to be an effective strategy to control the luminescence and even to induce new functions. However, the rules for selecting the impurity dopant ions still unclear at present. Therefore, further investigations towards structural engineering, pure-phase formation, and theoretical calculations are necessary to assess the optoelectronic properties of this series.

4 PEROVSKITE-DERIVATIVE STRUCTURE:

While there is still dissent on the exact boundaries in the broad perovskite family, we classify the compounds in which metal halide octahedra are connected by edge or face to form octahedral network as perovskite-derivative compounds. Ionic compounds usually adopt a corner-shared network to decrease the Coulombic repulsion as compared to face- or edge-shared network in which intermetal distances are shorter. Hence, ABX_3 compounds, being ionic in nature, usually adopts corner-shared perovskite structure assuming stable structures can be formed, i.e., within tolerance factor limit. However, if the size of *A*-site cation is too large as compared to that of *B*-site cations, the corner-shared octahedral network often collapses and face-shared or edge-shared octahedral network dominates. Additionally, if the binding forces become more covalent in nature (as observed in $[BiI_6]^{3-}$ complex), the Madelung term in the stabilization energy decreases significantly. This leads to greater orbital overlap and often deters the preference for corner-sharing structures, instead favoring higher modes of connectivity such as face-shared octahedral networks. Like perovskites, these compounds can also be classified as 3D, 2D, 1D and 0D structure based on the degree of connectivity (**Figure 1**).

4.1 3D perovskite derivative structure:

Having the stoichiometry of ABX_3, the most common 3D perovskite derivative structures are commonly known as hexagonal-type perovskites. However, unlike conventional perovskite

structure the structural framework is formed by face-sharing [BX_6] octahedra or *A* or *B*-centered trigonal prisms. This structural arrangement results in dimers, trimers, tetramers, or longer fragments of chains and shorter metal-metal distances and smaller metal-halide-metal bond angles as compared to conventional perovskites. These structural variations occur when the ionic radius of the *A*-site cation is much larger than the *B*-site cations, such as the compounds containing monovalent alkali metals in *A*-site and d-transition metals at *B*-site, so as to release the strain caused by the mismatch in the size of the cations. The transformation from conventional cubic perovskite to these hexagonal type perovskites can be visualized by the stacking sequence of [AX_3] layers. If the stacking is entirely cubic in nature (ABA), the structure resembles conventional perovskite structure, whereas hexagonal stacking (ABC) with respect to adjacent layers results in 1D face-shared halo-metalate chains. In between these two extremes, the ratio of cubic to hexagonal stacking determines the length of the one-dimensional chains. **Figure 18** illustrates representative structural evolution of $[MnCl_6]^{4-}$ octahedral networks between conventional corner-shared perovskite structure ($KMnCl_3$) and pristine face-shared 1D chloro-manganese chain (dimethylammonium manganese chloride). Moving from the smallest *A*-site cation (K) towards largest *A*-site cation (dimethylammonium), the ratio between cubic to hexagonal connectivity decreases and the compounds develop more face-shared network. These structures are often represented by Ramsdell notation in which the structure is described by a number which indicates the number of layers, followed by symmetry of unit cell, denoted as R for rhombohedral, H for hexagonal, C for cubic. For example, $CsMnCl_3$ structure can be noted as 9H, which consists of face-shared $[Mn_3Cl_{12}]$ trimers, stacked octahedrally (corner-shared) to form 3D network (**Figure 18c**). A two-dimensional close-packed structure with the chlorine atoms is formed by fitting the cesium cations into holes between the $[Mn_3Cl_{12}]$ trimers. A full structural description of these hexagonal types of oxide perovskites can be found in the article by Tilley[197].

To date, hexagonal type halide perovskites have received much less attention as compared to the perovskite structures, and the reports on their structural and optoelectronic properties

are fairly limited. Except for Cu^{2+}, nearly all the first-row transition metals in their divalent state are known to form hexagonal type perovskite structure with chloride and bromides. However, most of these compounds are moisture sensitive and easily degrade in ambient conditions[149, 198]. Due to presence of magnetic transition metal cations, most of the earlier studies were focused on their magnetic properties[199]. Recently, Daub et al synthesized $ANiX_3$ (A = Gu, FA, MA; X = Cl, Br) and $MAMnBr_3$ via solution processing routes[200]. **Figure 18e** and **f** illustrate that the optical spectra are not influenced by the *A*-site cation, while a noticeable red shift in the charge transfer (CT) and "d-d" transitions for the bromide compounds is observed when compared to the chloride compounds. In addition, the typical "d-d" transitions of Ni^{2+} (d^8 system) surrounded by octahedral geometry are also present. Furthermore, due to the face-shared octahedral network, the bands near the band edges tend to be relatively flat, resulting in larger bandgaps and inferior charge transport properties. Although the hybridization between metal and halides states enables adequate band dispersion along the face-shared chain, the separation of chains in other directions typically leads to flat bands in the corresponding directions and imparts anisotropic properties.

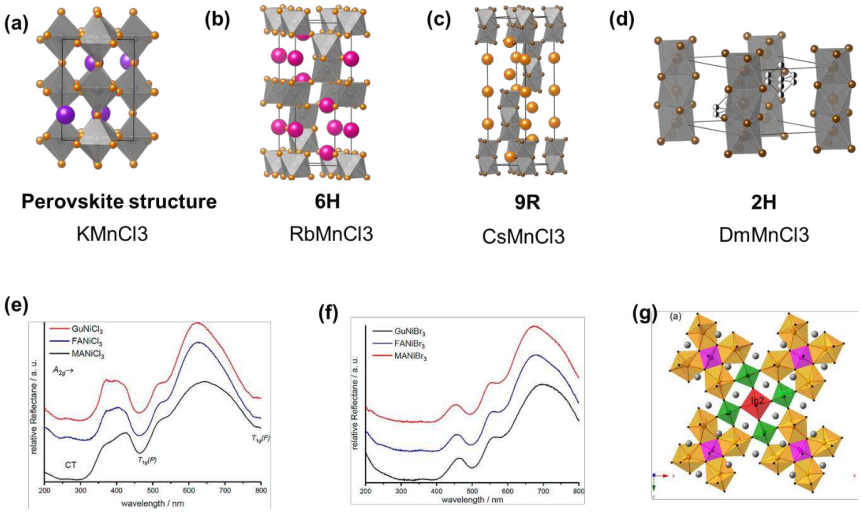

***Figure 18**. (a) − (d) illustrates representative structural evolution of $[MnCl_6]^{4-}$ octahedral networks between conventional corner-shared perovskite structure ($KMnCl_3$) and pristine face-shared 1D chloro-manganese chain. UV-Vis spectra of $ANiX_3$ (A = MA, FA, Gu) (e) X = Cl, (d) X = Br. (g) Crystal structure of $Cs_{1.17}In_{0.81}Cl_3$ with the space group I4/m with xy layer at z = 0. (e)(f) Reproduced with permission from Daub et al., Z. Anorg. Allg. Chem., **644** (5), 280-287 (2018). Copyright 2018 Wiley-VCH GmbH.[200], (g) Reproduced with permission from Tan et al., Chemistry of Materials **31** (6), 1981-1989 (2019). Copyright 2019 American Chemical Society.[201]*

Apart from typical ABX_3 stoichiometry, many different stoichiometric compounds are possible by reacting monovalent alkali halides and transition metal halides, and many of them form 3D octahedral network. For example, the multivalent state of In can provide a unique 3D structural network in $Cs_{1.17}In_{0.81}Cl_3$ where both corner-sharing and edge-sharing $InCl_6$ octahedra and $InCl_7$ pentagonal bipyramids are present[201] (**Figure 18g**). Nevertheless, the predicted large indirect band gap of ~2.27 eV suggests poor photo-absorption properties, and further characterizations are still needed to rule out this unique structure. A similar crystal structure was also reported in $CsMn_4Cl_9$.

4.2 Low-dimensional perovskite-derivative structure:

Like low-dimensional perovskites, perovskite derivative compounds which do not offer 3D octahedral network are grouped here. The first member of this group is the face-shared or edge-shared chains which propagate in one of the crystallographic directions (**Figure 19a, b**). The optoelectronic properties of these 1D structure are highly anisotropic and exhibit high exciton binding energies and large bandgaps. Nevertheless, as the geometric constraints are further reduced, a much wider range of organic cations, including large organic molecules, chromophores, solvated ion cluster, and even transition metal complexes can be incorporated into the 1D perovskite derivative structure. This unique opportunity further extends the excellent tunability of the optoelectronic properties for a wider range of applications such luminescence[202], photochromism[203], ferroelectricity[204], magnetism[205] etc. Low-bandgap

organic molecules can enhance the optical properties of a compound by acting as strong light absorbers through electron or energy transfer processes. One example is $(C_7H_7)BX_4$ (B = Sb, Bi, X = Cl, Br, I), which contains edge-sharing $[BX]_6$ chains separated by π-stacked tropylium ($C_7H_7^+$) cations and photoinduced electrons transfer occurs between inorganic and organic layers[206]. Utilization of polarizable organic cation with inorganic lattice further opens up new avenues to tune the excitonic binding energies of these low-dimensional structure. However, achieving highly ordered and efficient π–π stacked organic semiconductors within the structure can be challenging. Nonetheless, using smaller organic cations could lead to shorter X•••X or X•••C distances between the 1D chains, resulting in larger intermolecular interactions and reduced dielectric confinement[207, 208].

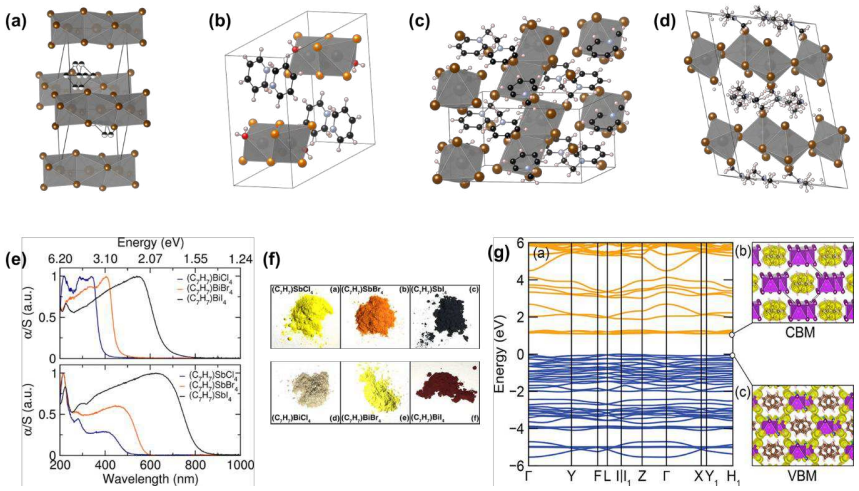

Figure 19. *(e) Kubelka–Munk transformed UV–visible diffuse reflectance showing the absorption edges for each compound across the visible spectrum. (f) Bright-field photographs of ground powders of (C7H7)MX4 (M = Bi3+, Sb3+; X = Cl–, Br–, I–) compounds. (g) and structure of (C7H7)BiI4 across two high-symmetry paths in the Brillouin zone. Band-decomposed charge densities corresponding to the CBM and VBM illustrate the hybrid nature of the frontier states (displayed at the same electronic density isosurface in yellow). (e-g)*

*Reproduced with permission from Oswald et al., Inorganic Chemistry **58** (9), 5818-5826 (2019). Copyright 2019 American Chemical Society.*[206]

The 1D perovskite derivative structure also offers the advantage of facilitating ferroelectric transitions, which is another crucial aspect. This can be achieved by incorporating transition metals and organic cations with potential order-to-disorder (OTD) characteristics at the *B*-site, thereby leading to the formation of various functional 1D perovskite derivative compounds. The flexible alkyl amines, saturated naphthene-based amines, saturated heterocycle-based amines, rigid DABCO (DABCO = 1,4-diazabicyclo[2.2.2]octonium) and their derivatives are typically used as potential OTD cations[209-211]. For instance, (pyrrolidinium)$MnCl_3$ exhibits excellent ferroelectric properties and a high photoluminescence quantum yield[212]. The pyrrolidinium cation is disordered at room temperature, and it undergoes an ordered transition when cooled down to 273 K. This OTD transition of the organic cation enables the crystal structure to undergo a nonpolar to polar phase transition, which is an indication of ferroelectricity. Since the functional groups are A-site cations, ferroelectric properties can be modified by appropriate *A*-site cations. For instance, replacing pyrrolidinium with 3-pyrrolidinium resulted in the formation of a new ferroelectric compound with improved spontaneous electronic polarization, high Curie temperature, high fatigue resistance, and superb luminescence efficiency[213]. Substituting Mn^{2+} with Cd^{2+} at the *B*-site also leads to similar ferroelectric features as they have similar ionic radii and coordination types. [204]. These examples demonstrate that lead-free perovskite derivative compounds can be excellent alternatives for designing multifunctional devices such as ferroelectric photovoltaics, ferroelectric LEDs, and multiferroics.

Additionally, 1D perovskite derivatives often provide much needed stability due to the shielding effect of the large organic cations. For instance, 1D (DAO)Sn_2I_6 (DAO, 1,8-octyldiammonium), which forms 1D edge-shared chains, was found to be stable in water for more than 15 h [214]. The 1D face-shared or edge-shared infinite chain can be transformed into 0D bi-octahedral structure by introducing metal cation defects. These 0D structures are common in trivalent

metal-based ternary halides. For example, a direct substitution of Pb^{2+} with trivalent metal cations (B^{3+}) leads to a general formula of $A_3B_2X_9$ which can be considered as a defect-variant structure of perovskite derivatives. Keeping the metal octahedra ($[B^{3+}X_6]^{3-}$ or $[B^{4+}X_6]^{2-}$) as the core, different organic or inorganic monovalent cations can be incorporated within these structures. For example, if only 2/3 of the *B*-sites are occupied and 1/3 of the *B*-sites remain vacant (at a ratio of 2:1), that can be represented as $A_3B_2\square X_9$, where $\square$ denotes a vacancy. These $A_3B_2X_9$ structures form two polymorphs depending on the size of the *A*-site cations. For larger *A*-site cations and halides, the structure consists of isolated bi-octahedra $[B^{3+}{}_2X_9]^{3-}$, leading to a 0D structure. Furthermore, these isolated bi-octahedra can form via two types of coordination such as face-sharing[215] and edge-sharing octahedron units, with the latter being the most common. Current research efforts are mostly focused on the Sb^{3+} and Bi^{3+} related halide compounds which are phase-stable in ambient environment and their stable valence ns^2 electrons hybridize with halides to form a similar electronic structure as that of Pb-based halide perovskites. Nevertheless, their 0D electronic structure results in flat bands, high effective mass, and large optical bandgaps. For example, polycrystalline films of $A_3Bi_2I_9$ (*A* = MA, Cs) show carrier mobilities less than 1 $cm^2V^{-1}s^{-1}$ at room temperature which is at least an order of magnitude smaller than the mobility of Sn- and Pb-based 3D halide perovskites[216-219]. Similarly, Sb-based 0D compounds also have heavy carrier effective masses and low mobilities at room temperature[157, 220].

5 NON-PEROVSKITE HALIDE COMPOUNDS:

Despite the popularity of perovskite and perovskite-derivative halide structures, several non-perovskite structures also show interesting optoelectronic properties with excellent promise in optoelectronic devices. The stoichiometry of these compounds typically differs from perovskite compositions and may offer tetrahedral metal halide coordination as opposed to purely octahedral coordination in perovskite structures. Nevertheless, due to presence of halides, the chemical nature of these compounds is strikingly similar to that of halide perovskite and perovskite-inspired compounds and can offer rich structural diversity as well. With the heavier

halides (Cl, Br, I), these non-perovskite compounds show excellent solution processability and have the prospects for implementation in device architectures like that of perovskite-based compounds. Among these non-perovskite structures, they can be further classified as 3D structure and low-dimensional structure based on the propagation of metal halide network.

5.1 3D non-perovskite structure:

One of the major challenges for trivalent metal cation-based perovskite and perovskite derivative compounds is their charge transport bottleneck arising from electrostatically bonded *A*-site cations which results in low-dimensional crystal structures. To mitigate that, *A*-site cations can be replaced by transition metal cations that are also capable of hybridization with the halogen orbitals. As opposed to 12-coordinated A-site cations, these transition metals offer octahedral coordination with halides and active participation in the band-edge formation in the final structure. This replacement strategy resulted in a plethora of compounds in which a 3D metal halide network could be preserved via face-shared, or edge-shared, or even corner-shared octahedra. One of the most notable examples from this series is the solid solution of silver iodide and bismuth iodide with the chemical formula of $Ag_aBi_bI_{a+3b}$. These structures closely resemble to O3-type transition metal oxide (e.g., Na_xFeO_2, $x <= 1$) structures in which an alternate layer structure with alkali cation sheets is sandwiched between transition-metal slabs, resulting in a close packing ABCABC pattern (Figure 20a) [221]. However, in contrast to typical O3-type transition metal oxide structure, the cation layers in silver bismuth iodides also comprise vacancies determined by the charge neutrality rule originating from partial occupancy of metal cation sites. Consequently, the determination of the exact crystal structure of silver bismuth iodide series remains difficult and is often ambiguous. For example, the smallest composition of these series, $AgBiI_4$ can be structurally resolved to both $CdCl_2$-type ($R\bar{3}m$) or cubic defect-spinel ($Fd\bar{3}m$) within a similar percentage of error[222]. Nevertheless, the $CdCl_2$-type rhombohedral structure is predominant in silver-rich compositions having Ag/Bi > 1, while the bismuth-rich fraction (Ag/Bi < 1) adopts a cubic defect spinel structure[223]. In the rhombohedral structure, disordered Ag^+ and Bi^{3+} cations occupy every other <111> layer of the space and the halides form a cubic close-packed sub-lattice as a base matrix. The cubic

spinel structure, in contrast, contains more vacant sites in the edge-shared cation octahedral sublattice as compared to the rhombohedral structure. Figure 20 illustrates these crystal structures. It should be noted here that hexagonal rhombohedral structure is sometimes called as ruddorfite, following Turkevych and coworkers' suggestion[224], although a mineral with similar structure was earlier termed as caswellsilverite by Okada and Keil in honor of geologist Dr. Caswell Silver[225]. On the other hand, the O3-type structure is well-known in the field of cathode materials and is also heavily used in scientific literature.

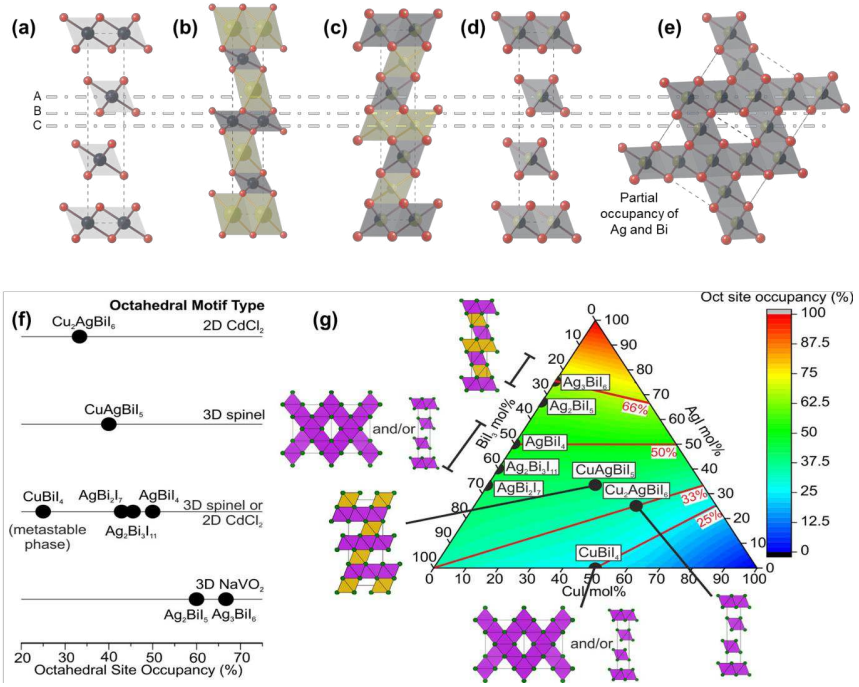

Figure 20. *crystal structure of (a)$CdCl_2$, (b) Na_xFeO_2, (c) Ag_2BiI_5, (d) rhombohedral $AgBiI_4$, (d) cubic spinel $AgBiI_4$, (f) The relationship between occupancy of the octahedral (Oct) sites and type of Oct motif formed, giving chemical control over dimensionality of the Oct network. (g) The same relationship shown in the CuI–AgI–BiI_3 phase space, where the color map and red contour lines represent total Oct site occupancy. (f) (g) Reproduced with permission from*

Sansom et al, Inorganic Chemistry 60 (23), 18154-18167 (2021). Copyright 2021 The Authors, licensed under a Creative Commons Attribution 4.0 International (CC BY 4.0) license. No changes were made.[226]

The substitution of silver with copper leads to analogous compositions of $Cu_aBi_bX_{a+3b}$, although the crystal structure and stability of these series are still under debate. Like silver bismuth iodides, copper bismuth iodides were also reported to crystallize in two compositions, a defect spinel $CuBiI_4$ and a rhombohedral Cu_2BiI_5 with ambiguous structural information[227, 228]. However, as copper has a much smaller ionic radius (0.6 Å) as compared to silver (1.15 Å for Ag^+) and is known to form tetrahedral coordination with halides, it is highly likely that Cu^+ occupies the tetrahedral sites in these structures, thus differing from silver bismuth iodide structures. Recently Sansom et al[226] carried out detailed investigations to resolve the crystal structure of $CuBiI_4$, which also faces similar issues as that of $AgBiI_4$ (possible crystal structure can be both $CdCl_2$-tupe rhombohedral and defect spinel). They also commented that $CuBiI_4$ is most likely a metastable phase as the composition converts to CuI and BiI_3 at room temperature [229]. Recently, a theoretical study predicted 15 possible crystal structures of $CuBiI_4$ with low formation energy, relying on their mechanical and dynamic stability. However, there is currently no experimental evidence to validate these findings[230].

Replacing bismuth with antimony has proven to be an interesting strategy in lead-free halide perovskites. However, very few reports exist of silver antimony halides or copper antimony halide compositions. Recent studies indicate that $AgSbI_4$ and $AgSb_2I_7$ exhibit similar structural features to those of bismuth-based analogues with $AgSb_2I_7$ forming the Ag-deficient *Fd*3*m* cubic crystal structure[231], and $AgSbI_4$ crystallizes into $CdCl_2$-type rhombohedral structure [232]. On the other hand, there is only one report on the possibility of Cu_3SbI_3 compound formation which unfortunately lacks any structural information[233].

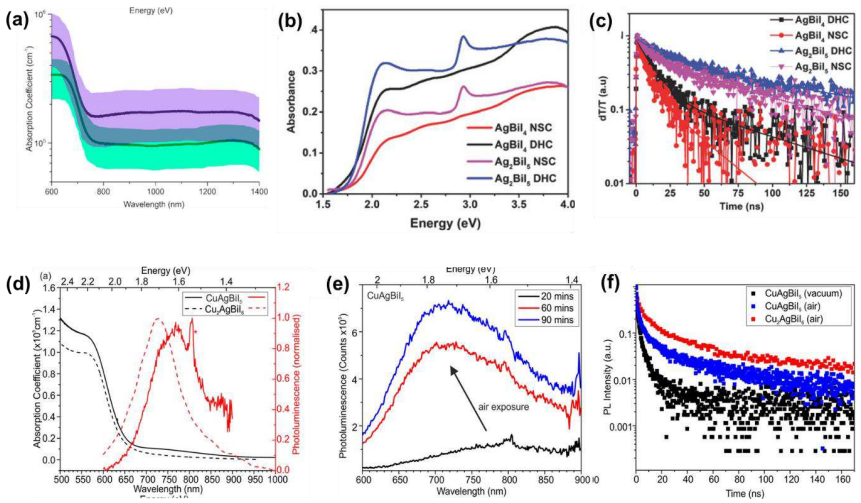

Figure 21. (a) Absorption coefficient of $AgBiI_4$ films. The shaded areas in indicate the error limits, derived from the standard deviations of the measured film thicknesses, (b) UV-Vis absorbance of $AgBiI_4$ and Ag_2BiI_5 under different synthesis process, (c) Transient absorbance lifetime of the same. (d) Absorption coefficient and PL measured on $CuAgBiI_5$ (solid lines) and Cu_2AgBiI_6 (dashed line) thin-films. (e) The shift and increase in the PL signal of $CuAgBiI_5$ thin-films exposed to air. (d) TRPL of $CuAgBiI_5$ thin-films measured in vacuum (black) and air (blue), compared to Cu_2AgBiI_6, measured in air (red). (a) Reproduced with permission from Sansom et al, Chemistry of Materials ***29*** *(4), 1538-1549 (2017). Copyright 2017 American Chemical Society, under a Creative Commons Attribution 4.0 International (CC-BY) License. No changes were made.*[222]*, (b)(c) Reproduced with permission from Ghosh et al, Adv. Energy. Mater.,* ***8*** *(33), 1802051 (2018). Copyright 2018 Wiley-VCH GmbH.*[234]*, (d)-(e) Reproduced with permission from Sansom et al, Inorganic Chemistry 60 (23), 18154-18167 (2021). Copyright 2021 The Authors, licensed under a Creative Commons Attribution 4.0 International (CC BY 4.0) license. No changes were made.* [226]

The optoelectronic properties of these compounds depend heavily on stoichiometry and vary significantly due to cationic disorder and non-stoichiometric composition. The optical

bandgaps of rhombohedral and cubic $Ag_aBi_bI_{a+3b}$ composition series are reported in the range of 1.55–1.82 eV (indirect) and 1.6–1.93 (direct) with cubic structures (Bi-rich) usually exhibiting smaller bandgaps[223, 224, 234-236]. However, all of the compositions of Ag-Bi-I ternary systems, in general, exhibit absorption coefficients in the range of 10^5–10^6 cm^{-1}, which is advantageous for realizing photovoltaic devices. While the photoluminescence from these compounds is poor, the carrier mobility is decent enough to offer good optoelectronic properties. Both the crystal structures exhibit indirect band gaps from DFT calculations. In comparison to the cubic structure, the computed bandstructures demonstrate larger indirect band gaps and shallower valence band maxima in rhombohedral structure. Defects such as the presence of excess Ag in the rhombohedral phase and the deficiency of the octahedral sites in the cubic phase contribute significantly to optoelectronic properties. There are currently several challenges associated with this series in achieving high performance optoelectronic devices such as stability in ambient environment, presence of impurity phases, and cationic disorder in the crystal structure.

5.2 Low-dimensional non-perovskite structure:

Low-dimensional non-perovskite halide compounds are characterized by tetrahedral metal halide coordination as opposed to the octahedral coordination found in perovskite and perovskite-inspired structures. Most of these compounds can be considered as large bandgap semiconductors with the bandgap ranging from 2 eV to 5 eV depending on the tetrahedral network and stoichiometry. Most interestingly, the emission profiles of these compounds are mostly in the visible range.

As mentioned earlier, when the size difference between metal cations and halides is smaller than 0.414, tetrahedral coordination is preferred. The most notable example is the monovalent Cu-based ternary halide compounds. Monovalent Cu usually possesses coordination numbers of two, three and four, resulting in coordination geometries of linear, trigonal, and tetrahedral, respectively. These compounds can be characterized by low-dimensional crystal structures using the general formula of $A_aCu_bX_{a+b}$. They usually crystallize into two different

polymorphs: 0D structures having isolated copper halide tetrahedra, and 1D structures where copper halide tetrahedra are connected via either face-sharing or edge-sharing networks. These structures should not be confused with Cu^{+}-based organic polymeric complexes or coordination complexes which are denoted with the general formula of $Cu_xX_yL_z$ (X= halides, L = N, S or P based organic ligand). While the building blocks in both cases are based on copper halide complexes, there is no charge transfer between organic and inorganic motifs in the former case, while organic ligands actively take part in optoelectronic properties in organic polymeric complexes in the latter. Interested readers can look at an excellent review by Peng and co-workers on Cu-based coordination polymers[237]. Our discussion here is limited to low-dimensional ternary Cu-based halides in which A-site cation has no direct role in determining the optoelectronic properties of the compounds, but rather provides rich structural diversity which indirectly affects the optoelectronic properties. The zero-dimensional $Cs_3Cu_2I_5$ was initially reported by Hosono et al. in 2018, showcasing bright blue emission with a peak at 445 nm, large Stokes shift of about 155 nm, and high PLQYs of 90% and 60% for single crystals and thin films, respectively[238]. Subsequently several ternary Cu-based non-perovskite structures were discovered with 0D and 1D Cu-X tetrahedral network. **Figure 22a** illustrates the different coordination environments of Cu halide and two polymorphs of $A_aCu_bI_{a+b}$ exhibiting 0D structure and 1D Cu halide network. The emission peaks are illustrated in **Figure 22b**. The structural reorganization of excited states caused by the Jahn-Teller distortion can account for the emission mechanism of these compounds.

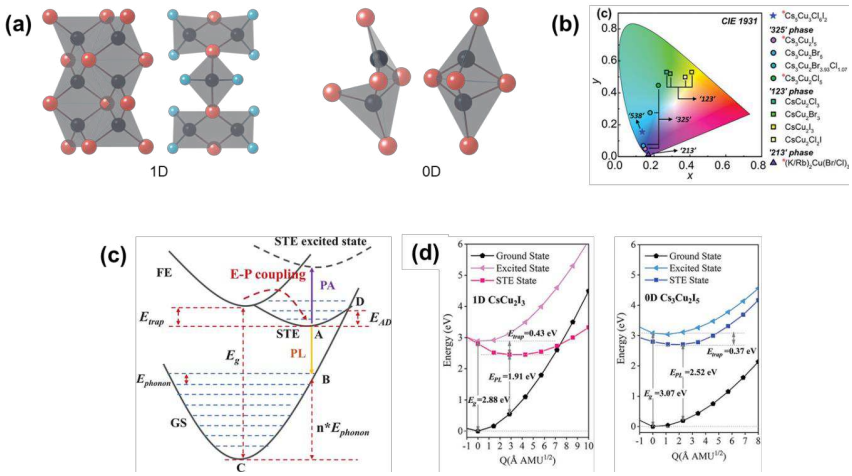

Figure 22. *(a) Polyhedral network of Cu-halide, showing 1D chains, and 0D isolated bi-tetrahedra. (b) A chromaticity coordinate diagram for the alkali copper(I) halide emitters. The red asterisks indicate the structures with over 90% PLQY. (d) Simplified STE emission model at low temperature, (d) Configuration coordinate diagrams of ground, excited, and self-trapped excited (STE) states for 1D $CsCu_2I_3$ and 0D $Cs_3Cu_2I_5$ with indications of the calculated ground and excited-state relaxation energies (E_{trap} is the self-trapping energy, E_g is the bandgap) and emission energies (E_{PL}). (b) Reproduced with permission from Li et al., Adv. Mater., **32** (37), 2002945 (2020). Copyright 2020 Wiley-VCH GmbH.[239], (c), (d) Reproduced with permission from Xing et al, Adv. Funct. Mater., **32** (2022), 2207638. Copyright 2020 Wiley-VCH GmbH.[240]*

Apart from monovalent Cu compounds, several transition metals exhibit tetrahedral coordination with halides such as Zn^{2+}, Mn^{2+}, Ni^{2+}, and Co^{2+}, adopting a general formula of A_2MX_4. Tetrahedral coordination is common for iodide compounds, while chloride and bromides usually form octahedral coordination. Despite their existence for several decades, these compounds have recently gained renewed interest due to their PLQY, narrow spectral emissions, and remarkable stability under ambient conditions. For instance, Mn^{2+} in tetrahedral coordination exhibits green emission, making it a suitable candidate for phosphors.

The high PLQY observed in these 0D structures with tetrahedral coordination can be attributed to the confinement within isolated tetrahedra.

6 OPTOELECTRONIC/ENERGY APPLICATIONS

Lead-free halide compounds have long lived in the shadow of LHPs in the field of optoelectronic devices, due to the lack of an exciting mix between bandgap energy, carrier mobility, and the electron-velocity field, which is highly tunable in LHPs, especially in 3D structures. However, there has been a recent surge in the prominence of lead-free halide semiconductors, as they are now being developed to meet the specific needs of different applications, rather than attempting to optimize a single compound for every application. In this following section, we will briefly review their exciting prospects in optoelectronic applications, highlighting current challenges and potential remedies for future development. By exploring the unique properties of these materials, we may unlock new possibilities for optoelectronic devices that can meet the specific demands of various applications.

6.1 Photovoltaics

According to Shockley–Queisser limit, a semiconductor with a bandgap of about 1.3 eV is ideal for single junction solar cells and a bandgap of about 1.7 eV is ideal for being a top cell with Silicon tandem architecture. While very few lead-free halide compounds satisfy the single junction solar cell requirement, there is a vast compositional space suitable for the top cell in tandem architecture. Aside from the bandgap, charge transport properties and carrier lifetime are other major requirements for high performing photovoltaic devices. In general, low-dimensional structures (2D, 1D, and 0D) offer large excitonic binding energy, and poor charge transport properties which favours charge recombination over charge separation. Consequently, 3D structures remain the most appropriate solution for photovoltaic applications. Since the first report on $MASnI_3$-based lead-free perovskite solar cell[241], significant efforts have been devoted to various lead-free halide semiconductors for photovoltaic applications. The topic remains one of the most active areas of research within the perovskite community. Nevertheless, the great success of LHPs has not yet been

replicated in lead-free halide compounds. In general, an excellent photovoltaic absorber usually possesses broad and strong light absorption (small and direct bandgap), efficient charge carrier generation (small exciton binding energy), long carrier diffusion length (long career lifetime), and tolerance towards native defects. While LHPs offer all of those properties, lead-free compounds usually lack one or two key properties. For example, low-dimensional halide compounds (0D and 1D) usually have inefficient charge carrier generation due to large exciton binding energy and poor hot carrier extraction due to molecular crystal structure. On the other hand, 3D double perovskites which offer better charge transport properties, usually exhibit large and indirect optical bandgaps, making them transparent towards most of the visible solar spectrum.

Among the lead-free halide compounds, THPs have been the most investigated semiconductors for PV applications and are currently the most efficient absorber materials. Unfortunately, Sn-based halide perovskites are prone to self-doping due to easy oxidation of Sn^{2+} to Sn^{4+}, even in mild oxidizing conditions, which results in poor device performance and stability[242]. Approaches to increase stability by preventing Sn^{2+} oxidation, such as optimizing the precursor composition and purity, controlling the synthesis environment, and alloying with reducing agents have had encouraging successes. However, nearly all of these techniques require stringent control over the environment and fabrication procedures. Alarmingly, it has been shown that Sn^{2+} can oxidize even in organic solutions such as DMSO, which warrants better control of the fabrication procedures[243]. Moreover, crystallization kinetics in THPs are extremely rapid; this makes it challenging to control film morphology within a short period of time during spincoating. Hence, it is still a grand challenge to formulate a universal method such that the crystallization dynamics can be controlled and the oxidation of Sn^{2+} can be greatly reduced. A recent study probed into the strong coupling between oxidation rates of Sn^{2+} and solvent chemistry, shedding light on future directions to achieve high performance[244].

Alternatively, the stability of THPs can also be improved by incorporating large organic molecules to transform the 3D structure into a 2D structure. Additionally, the large organic

molecules act as a protective layer on top of the inorganic $[SnI_6]^{4-}$ network from oxidizing environment[47, 245]. Consequently, shelf life and operational stability of Sn-based halide perovskites have improved significantly in the past decade[246]. Further improvement is warranted in the development of low-dimensional compounds as the inorganic octahedral networks tend to crystallize in parallel directions to the substrates which greatly impede the charge transport properties in vertical solar cell architecture. In addition, low-dimensional structures also suffer from larger bandgaps and larger exciton binding energies which are detrimental for high performance solar cells. These challenges can be alleviated by employing mixed 2D/3D crystal structures. A small amount of large organic molecule can promote the formation of low-dimensional structures in a controlled manner, whereas the optoelectronic properties of the compounds are mostly controlled by the 3D structure[247]. Another major breakthrough was achieved by the development of "hollow perovskites" in which 3D Sn-based halide perovskites was converted into mixed-dimensional structure by incorporating diammonium cations[50, 51, 248]. In these structures, the divalent organic cations partially replace both A-site and Sn^{2+} cations, resulting in better morphology, higher stability, and fewer defects in the thin-films[249].

Unlike THPs, Ge-based halide perovskites usually have larger bandgaps, and poor solution-processability, resulting in abysmal performance as PV absorber materials[31, 250] Additionally, Ge-based halide perovskites also suffer a similar fate to that of THPs due to rapid oxidation of Ge^{2+} to Ge^{4+} even in mild oxidizing environments. Surprisingly, this undesirable property was found suitable for the development of mixed Ge/Sn-based halide perovskite systems[31], which was found to be coated with GeO_2 that prevents further degradation. A $CsGe_{0.5}Sn_{0.5}I_3$-based solar cells showed >10% PCE with excellent stability in ambient environment[251]. Mixed Ge/Sn alloys exhibit significant advantages over pure Ge-based perovskites, including narrower bandgaps and enhanced stability, positioning them as superior alternatives to lead-free perovskite solar cells compared to pristine Sn or Ge-based halide perovskites. With further

advancement in germanium and Sn-Ge alloyed materials, they have the potential to outperform the best-performing lead-based halide perovskite devices currently available.

In the past few years, explorations of trivalent Bi^{3+} and Sb^{3+} based ternary iodides have been reinvigorated as non-toxic and stable alternatives to LHPs for PV applications. Compared to Sn/Ge-based halide perovskites, these trivalent metal halides are highly stable under ambient conditions and require less control over solution chemistry to achieve pure phase formation. Unfortunately, the optical bandgaps of these trivalent metal ternary iodides are quite large (~1.9 eV which is smallest amongst different halides) and the single-junction solar cells will be limited by small short-circuit current density. Considering the rapid rise of tandem architecture in PV, an efficiency of ~10% could be a gamechanger in the PV industry and these trivalent metal halides could be an excellent prospect for tandem applications as the top cell along with Si as the bottom cell due to their excellent ambient stability. Early studies on Bi-based ternary iodides showed exciting results with PCE reaching over 1% in mesoporous solar cell architecture[252]. However, optical characterization revealed extremely short carrier lifetimes of below tens of nanoseconds and low PLQY, signifying the adverse role of defects [253]. The prevalent defects in $Cs_3Bi_2I_9$ arise due to iodine vacancies which can be passivated by synthesizing in excess BiI_3 environment[254, 255]. Currently, the best performing Bi-based ternary halide is $Cs_3Bi_2I_9$ which recorded an efficiency of 3.2% by employing a very thin absorber layer which enhances the carrier extraction efficiency[256]. Still, the devices showed large open-circuit voltage loss, which can be attributed to the poor film morphology and splitting of the band edge.

However, the major bottleneck arises from the molecular crystal structure of these trivalent ternary halide compounds which limits efficient charge extraction. Utilizing smaller *A*-site cations could improve the dimensionality of these structures from 0D to 2D as seen for Sb^{3+} based ternary iodides. For example, replacing Cs^+ with NH_4^+ or Rb^+ or I^- with Cl^- can improve the dimensionality of Sb-based ternary iodide from 0D to 2D structure, which subsequently enhances the optoelectronic properties, and eventually PV performance[157, 257]. The best

performing ternary Sb-based halide compounds solar cell with 3.3% efficiency was recorded with 2D $MA_3Sb_2(I/Cl)_9$ as absorber layer[258]. Interestingly, a recent report demonstrated that despite low-dimensional crystal structure, more than 80% EQE was recorded from (N-EtPy)[$SbBr_6$]-based solar cells[259]. The authors suggested that the short Br···Br distance between neighbouring $[SbBr_6]^-$ octahedra is the most likely reason for assisting the charge transport between the inorganic metal octahedral, resulting in better performance compared to Sb^{3+} based ternary halides.

The limitations of charge transport properties due to molecular structure can be eliminated in double perovskite structures which possess the corner-shared octahedral network while exhibiting excellent ambient stability. Several small bandgap halide double perovskites are also predicted theoretically[60, 61]. As of today, only $Cs_2AgBiBr_6$ showed the promise as a PV absorber material with a large carrier lifetime of ~700 ns. However, $Cs_2AgBiBr_6$ has an indirect optical bandgap of 1.95 eV[72] which is a major limitation in achieving higher efficiency in single junction solar cells. In addition, theoretical calculations also revealed its poor tolerance towards intrinsic defects[84]. Hence, most of the focus on the $Cs_2AgBiBr_6$-based solar cells has been devoted towards fabrication of high-quality thin-films to minimize the non-radiative recombination. Currently, the highest efficiency for $Cs_2AgBiBr_6$-based solar cell devices have reached to 1.5% and 2.84% PCE in planar and mesoscopic architecture respectively[260, 261]. This is a significant advancement for lead-free perovskite solar cells considering the low toxicity and excellent stability of over months under ambient conditions.

Among non-perovskite structures, Ag_aBiI_{3+b} system has shown suitable bandgap and decent charge transport properties for PV applications. They have 3D edge-shared octahedral network along with excellent ambient stability. The optical bandgap of the Ag_3BiI_{3+b} system was found to be in the range of 1.75 − 1.9 eV depending upon the ratio of Ag and Bi. Moreover, Ag_3BiI_{3+b} system is highly stable and can be processed in ambient atmosphere which is an added advantage over LHPs. At present, the highest PCE of 4.3% was recorded based on Ag_3BiI_6 composition in a mesoscopic architecture[224]. Nevertheless, reducing bandgap by

doping could be a viable option as experimental results indicate that partial replacement of I^- with S^{2-} could induce notable contractions of the band gaps. Subsequently, 4 wt% S-doped Ag_3BiI_6 solar cells recorded an efficiency of 5.4%, which is the highest among lead-free non-perovskite structures [262].

In summary, the tremendous progress of LHPs made in the field of PV through novel film fabrication techniques and cation transmutation has failed to translate into the progress of lead-free halide compound-based solar cells. Sn-based halide perovskites still have the edge over other lead-free halide perovskites and perovskite-inspired materials, at least in terms of optoelectronic properties and solar cell performance. Hence, despite the poor stability in ambient conditions, THP performances saw a gradual increase over time along with improved stability, although it is still quite far away from that of LHPs. There are at least four fronts which need further investigations and optimizations to fully exploit the optoelectronic properties of THPs such as (1) passivating and reducing agents that can prevent self-doping, (2) better understanding of film formation dynamics, (3) improved device architecture with efficient charge collection and extractions, and (4) modification of crystal structure to stabilize the divalent oxidation state of Sn. On the other hand, other lead-free halide systems, especially low-dimensional structures are quite far away from the desired PV properties due to large optical bandgap, positions of band edges, and poor charge transport properties. Nevertheless, they also offer new possibilities for obtaining stable structures with improved efficiency. Low-dimensional materials are particularly advantageous because they allow for the tunability of multifunctional organic molecules, improving their charge transport characteristics. In addition, several proof-of-concept devices based on novel lead-free halide systems have been proposed. An alternative approach would be modifying the device architecture for lead-free halide systems which remain unexplored. For example, bulk heterojunction devices could overcome the challenge in charge transport properties in low-dimensional structures. In material systems, doping and alloying remain a largely unexplored space to exploit the full potential of lead-free systems. One example is Tl doping which reduces the bandgap of

$Cs_2AgBiBr_6$ from 1.9 eV to 1.6 eV. While Tl is highly toxic, even more so than Pb^{2+}, this indicates that there may be several possibilities for selective alloying. Overall, active research on lead-free systems is still limited, and compared to LHPs there are few investigations into the mechanisms of film formation, doping, and device architecture. Negative results could further aid in efficiently screening lead-free system for PV in an accelerated motion.

6.2 Photodetector

Beyond photovoltaics, the use of lead-free halide compounds in photodetection has gained significant attention in recent times. While traditional semiconductors like silicon and the III-Vs have been effective, the quest for higher efficiencies and lower costs fuels ongoing exploration. The convenient and low-cost solution preparation methods of lead-free metal halide compounds, coupled with their non-toxic nature, make them essential for commercial applications. As a result, the utilization of lead-free metal halide compounds in photodetection is becoming increasingly promising for next-generation technologies.

Many of the lead-free halide compounds exhibit direct bandgaps, high absorption coefficients, and low dark currents which are some of the important parameters for high photoconductivity gain. In addition, the bandgaps of these halide compounds, especially THPs, can be tuned such that a wide range of photon energies such as NIR to UV can be sensed efficiently. At present, 3D Sn-based iodide perovskites exhibit one of the lowest bandgaps among lead-free halide perovskites and subsequently, NIR photodetectors based on these compounds have already been demonstrated. For example, $FASnI_3$-based NIR photodetector, demonstrated by Yan's group[263] delivered a responsivity of 1.1×10^5 A W^{-1} under a driving bias voltage of 0.5 V along with a decent detectivity of 1.9×10^{12} Jones. As the stability of Sn-based 3D halide perovskites remains a challenge, Fan's group[264] grew $CH_3NH_3SnI_3$ nanowire arrays inside the porous alumina which resulted in excellent stability with decent NIR detection performance. Stability can also be improved by employing zero-dimensional perovskite derivative compounds such as $Cs_2SnCl_{6-x}Br_x$ [265]. As a broadband photodetector for visible light detection, 2D $(PEA)_2SnI_4$ -based single crystal devices recorded excellent specific detectivity of

1.92×10^{11} Jones (calculated). Moreover, these low-dimensional compounds exhibit much better stability and lower dark current than their 3D counterparts.

Unfortunately, these layered compounds exhibit anisotropic charge transport which demands vertical growth of crystallites during the fabrication process. The stability of the photodetectors can be further enhanced by employing trivalent metal ternary halides such as Bi^{3+} or Sb^{3+} based compounds. While single crystals showed low performance due to anisotropy, the microcrystalline structure greatly enhances the photon detectivity due to efficient charge collection. One of the highest detectivities among lead-free compounds was obtained with $CsBi_3I_{10}$ thin-film for red light detection[266]. The devices also showed excellent stability over 3 months. The stability and charge transport properties can be simultaneously improved by employing double perovskite structures. $Cs_2AgBiBr_6$-based photodetector demonstrated excellent photo response (~ 17 ns) along with ultralow detection limit[87]. One major shortcoming remains the large bandgap which results in responses only in the range of below 500 nm.

Nevertheless, a large bandgap semiconductor could be useful for UV detection. Recently, Cu^+–based non-perovskites have shown excellent promise as alternatives to the traditional UV detectors based on oxides, such as zinc oxide (ZnO) and tin oxide (SnO_2) which usually suffer from a slow response time and high temperature processing costs. The first report on a $Cs_3Cu_2I_5$-based device showed poor performance, owing to difficulties in uniform thin-film fabrication[267]. Overall, the emerging field of lead-free perovskites and perovskite-inspired halide compounds has demonstrated significant promise, with impressive strides made in the area of photodetector applications. These materials enable broad-spectrum photodetection spanning from near-infrared to ultraviolet light, thereby providing numerous opportunities for practical implementation. However, substantial work remains to enhance their figure-of-merit, and innovative approaches that differ significantly from those developed for LHPs are crucial for improving material quality. Advancements in this area have the potential to transform the field of optoelectronics, enabling a broad range of applications and accelerating progress towards next-generation technologies.

6.3 High-energy detector

At present, the direct detection of high-energy radiation, such as gamma and X-rays, is utilized in various fields, including but not limited to non-destructive material characterization, space exploration, security screening, medical diagnostics, computed tomography (CT), positron emission tomography (PET), and nuclear reactions. In direct detection, high energy radiation is absorbed by the detector which converts radiation into electrical signal, just like photodetection. While the basic requirements remain the same as with photodetection, the semiconductors also need to be stable under high energy radiation and should possess high attenuation coefficients. Perovskite-inspired halide compounds have many desirable properties for low-cost radiation detectors, including high attenuation coefficients, low dark current, excellent stability, and ease of synthesizability. Elements having higher Z-number provide higher interaction volume for the high energy radiation, thus higher attenuation coefficients or better stopping power. This interaction also generates electron-hole pairs which are directly proportional to the sensitivity of the detector. Hence, to increase the sensitivity and energy resolution, a low-bandgap semiconductor is preferred. However, smaller bandgaps also lead to higher dark currents which reduce the signal-to-noise ratio, thus degrading the detector performance. Bandgap values between 1.5 and 3.0 eV were found to be the ideal range to balance these two effects[268].

Furthermore, a radiation detector should also possess a large $\mu\tau$ product to efficiently extract all the charges from the millimetre-scale thick layer, an important device parameter to fully absorb radiation. At present, Bi and I-based compounds are front-runners in achieving high performance radiation detector devices due to their high atomic mass. The first report on lead-free X-ray detector was reported with $Cs_2AgBiBr_6$ single crystals[269]. Due to the long penetration depth of X-rays, single crystals are usually preferred for high energy detectors. The thick single crystals (mm to cm scale) also have a low defect density which increases $\mu\tau$ product, a large value of which is beneficial for high signal-to-noise ratio. The sensitivity of $Cs_2AgBiBr_6$ single crystal detectors for X-rays was found to be comparable to those made from $MAPbBr_3$. Apart from the single crystal detector, flexible X-ray detectors can also be

fabricated using a polymer-$Cs_2AgBiBr_6$ composite with similar performance as those of the single crystals[270].

Low-dimensional structures which offer higher resistance against ionic migration and higher resistivity are expected to perform better than 3D structures and can offer long-term stability. For example, a low detection limit of 55 $nGy_{air}\ s^{-1}$ (in perpendicular direction) is realized in 2D layered $(NH_4)_3Bi_2I_9$ single crystal devices. Moreover, low-dimensional structures exhibit anisotropic charge transport which is beneficial for anisotropic detection required for medical applications[271, 272]. $Rb_3Bi_2I_9$, another analogous structure also showed a record low detection limit of 8.32 $nGy_{air}\ s^{-1}$ along with high resistance to ionic mobility[273]. Ionic mobility can be further reduced by adopting zero-dimensional crystal structures such as $A_3Bi_2I_9$ which also exhibited descent X-ray detection performances[274, 275].

The advancements made in lead-free halide compounds for high energy detection are remarkable, offering a plethora of benefits such as low-cost fabrication, scalability of large area systems, and earth-abundant precursors. However, for these compounds to be practically useful, their figure-of-merit must be improved. The large dark currents exhibited by these halide-based detectors can obscure electronic signals, reduce sensitivity, and increase the lowest limit of detection. The inherent defect and impurity self-doping of Sn-based halide perovskites and the weak ionic bonding in halide compounds lead to increased dark currents and ionic conductivity, making it necessary for more research and effort to fully expand their potential. Reducing dark current and addressing radiation hardness are essential for enhancing the lowest detectable dose and evaluating reliability, long-term use, and disposability. With further investigation and innovation, these lead-free halide compounds can provide unparalleled benefits and revolutionize the field of high energy detection.

6.4 Scintillators

As an indirect detection technique for high energy radiation, scintillation detection requires only the scintillator crystal which absorbs the radiation (usually high frequencies) and emits light in another part of the spectrum (usually longer wavelength). The scintillators can then be

easily integrated with commercial light detection hardware like charge-coupled devices or complementary metal-oxide-semiconductors. Current commercial scintillators are usually bulk crystals and their synthesis usually requires high temperatures (621 °C for CsI:Tl, more than 2000 °C for $Lu_2SiO_5:Ce^{3+}$) which increases the production cost. Therefore, there is a great demand for scintillating materials which can be synthesized easily.

Low-dimensional lead-free halide compounds which exhibit high photoluminescence quantum yields, but suffer from poor charge transport properties, have huge potential as scintillators [276]. Luminescence in these compounds usually originates from self-trapped excitons which also eliminates the self-absorption. Furthermore, these compounds can be easily embedded in a flexible matrix to fabricate a functional composite film. Hence, much of the focus remains on the development of low-dimensional structures by incorporating large organic molecules. A prime example is Mn-based 0D structures with extremely high PLQY in the solid-state. By varying the A-site cations, a wide variety of scintillators has been demonstrated with Mn-based low-dimensional perovskites[277-279], with the most notable being Ethylenebis-triphenylphosphonium manganese bromide ($(C_{38}H_{34}P_2)MnBr_4$) a zero-dimensional Mn-based hybrid exhibiting 95% PLQY, recorded a light yield of ~ 80,000 photons MeV^{-1}, along with a low detection limit of 72.8 nGy s^{-1} [280].

While perovskite structures have dominated the research, non-perovskite structures such as Cu-based ternary halides have emerged as strong contenders due to their strong PLQY and stability. Moreover, their emissions can be easily tuned, enabling the development of scintillators for specific applications. Notably Rb_2CuBr_3 has demonstrated remarkable performance with near-unity photoluminescence quantum yield (98.6%) and a record-breaking light yield of ≈91056 photons per MeV, thanks to its strong carrier confinement and X-ray absorption capability[281]. Even zero-dimensional structures such as $Cs_3Cu_2I_5$ and β-$Cs_3Cu_2Cl_5$ have near-unity PLQY, excellent X-ray absorption, and low detection limits. These compounds also demonstrate remarkable operational stability and radiation hardness, making them suitable for long-term use[279-281]. Moreover, the emissions of these compounds can also be

tuned by doping suitable elements such as Mn^{2+} or rare-earth elements. Large-scale scintillator devices have also been successfully realized using close-space sublimation and nanoscale seed screening strategies, achieving high spatial resolution in X-ray imaging[282]. One of the current challenges is the afterglow (long lifetime) of the luminescence in these compounds which limits their detection limitations. Recent advancements in Ag-based ternary halides and 0D Cs_4EuX_6 have shown promising results in this regard, which bodes well for the future of lead-free halide scintillators. Low-dimensional Rb_2AgCl_3 has recently been reported to have fast scintillation decay time (in ns) which is a key parameter in dynamic X-ray imaging[283]. For gamma ray scintillation, 0D Cs_4EuX_6 showed excellent promise with high scintillation yield, which is even better than that of the commercial scintillator NaI:Tl[284]. However, the challenge of afterglow still persists, limiting their detection sensitivity. Overall, these compounds offer a safer and more efficient alternative to traditional lead-based scintillators and have the potential to revolutionize the field of X-ray imaging.

Double perovskites with lanthanide ions are also promising scintillator compounds considering they exhibit extremely high PLQY and are stable at high temperatures. $Cs_2NaLnCl_6$ (Ln = Tb^{3+} or Eu^{3+}) is an excellent example, showing a light yield even higher than that of commercially available scintillators and lead-based halide perovskites[97]. By utilizing doping and compositional engineering techniques, the optical and electronic properties of double perovskites can be effectively modulated. For instance, $Cs_2AgInCl_6$ doped with Na^+ and Bi^{3+} has been identified as an outstanding scintillator for real-time x-ray imaging[285].

An outstanding scintillator should possess several essential properties such as high PLQY, low self-absorption, fast decay time, and high light extraction efficiency. Unfortunately, many lead-free halide systems that exhibit exceptional figure-of-merit often ignore one critical factor: afterglow. Long afterglow times can cause imaging artifacts, superimposing the signal on the previous exposure. Additionally, defects within the scintillator can lead to nonradiative recombination, reducing the yield. Currently, scintillators-based on 3D structures are limited by their small Stokes shift, but low-dimensional structures with self-trapped excitons show

great promise in increasing this parameter. To overcome this bottleneck, excitonic emission or down-converters with perovskite emitters can be used to simultaneously achieve large Stokes shift and fast response times. Systematic studies on the stability against temperature, humidity, and radiation are also crucial parameters to meet the international standard IEC 60749 requirements.

6.5 Down-converters

The potential of optically pumped LEDs as transformative technology is immense, offering efficient and cost-effective solutions for white-light LEDs and down-converted displays. Their working principle is based on the efficient down-conversion of high-energy photons, which requires materials with high PLQY and negligible self-absorbance. Optically pumped LEDs have opened up exciting opportunities for advanced display technologies as well as for applications in solid-state lighting, and biomedical imaging. The key advantage of these LEDs lies in their simplicity of structure, spectral design flexibility, and high luminous efficiency. Given their immense potential, the development of high-performance down-converter materials remains a crucial area of research in materials science and engineering.

A huge number of down-converting luminescent materials based on lead-free halide compounds have been reported till date, thanks to their high PLQY and broad, large Stokes-shifted emission. These compounds cover nearly the entire visible light spectrum and even extend to near-infrared wavelengths, making them versatile components for efficient down-conversion phosphors. Their excellent stability and color rendering properties make them a perfect candidate for indoor lighting[286-288]. Doping strategies such as Bi and Sb-doping have also been found to increase the PLQY of these compounds, resulting in mixed yellow phosphors that achieve a high CIE coordinate and colour rendering index (CRI)[289, 290].

Apart from perovskite structures, halide compounds with non-perovskite structures have also become a focus of intense research as high-performance down-conversion luminescent materials. Among them, Cu-based ternary halides are particularly noteworthy for their intense and broad photoluminescence spectra, making them desirable for white light-emitting diode

(WLED) applications. These compounds exhibit high thermal and chemical stability, which makes them practical for a range of applications. For example, $Cs_3Cu_2I_5$ and $CsCu_2I_3$ mixtures were used to fabricate a high-performance WLED with a CRI of 88.4[291]. These tetrahedrally bonded compounds offer high chemical and thermal stability and have emerged as a promising non-toxic substitute for inorganic pigments. In another study, $(18\text{-crown-}6)_2Na_2(H_2O)_3Cu_4I_6$ was used to create a WLED with a high luminous efficiency of 156 lm/W and a color rendering index of 89.6[292]. Additionally, indium-antimony (In/Sb) alloyed halide single crystals also have demonstrated near-unity photoluminescence quantum yield and potential for use in high-performance WLEDs[293, 294].

6.6 Light-emitting diodes (LEDs)

LEDs based on solution-processed semiconductors have great application potential in energy-efficient lighting and displays. While lead-based halide perovskites are the front-runners in electroluminescence devices, lead-free perovskites and derivative compounds have the potential as non-toxic alternatives for wearable displays and are currently gaining momentum. The first lead-free perovskite LED based on $MASn(I/Br)_3$ thin-films was demonstrated by Tan and coworkers[295]. In the same year, all-inorganic $CsSnI_3$ was also utilized as an emitting layer to demonstrate near-infrared LED[296] with the maximum EQE of 3.8%. Nevertheless, both devices exhibited poor stability during operating conditions, which led to the development of low-dimensional Sn-based perovskites offering better stability against ionic migration and better confinement of excited carriers. A quasi-2D multiple quantum-well structure based on the composition of $(PEAI)_{3.5}(CsI)_5(SnI_2)_{4.5}$ shows much better stability than 3D counterpart, with LED devices exhibiting EQE up to 3% at 940 nm luminescent peak[297]. Several other low-dimensional Sn-based halide perovskite-based LED devices have also been demonstrated, such as orange emission from $(C_{18}H_{35}NH_3)_2SnBr_4$ [298], red emission from $(PEA)_2SnI_xBr_{4-x}$ [299], 2-thiopheneethyllamine iodide $(TEAI)SnI_4$ [300] to name a few. However, charge transport properties of 2D perovskites is restricted to inorganic layers by insulating organic long chains, resulting in inferior device performance compared to their 3D structures[301]. This drawback prompted researchers to adopt a vertical crystal arrangement in optoelectronic devices, with

inorganic layers oriented perpendicular to the substrate. This strategy promotes efficient transport of charge carriers, circumventing the limitations imposed by organic chains and boosting device performance.

While several Sb or Bi-based perovskite derivative compounds exhibit reasonable PLQY, working devices are scarce at present. Chu's group[302] was the first to demonstrate a functional device based on Sb-based perovskite derivative. However, the performance of these devices fell short due to the relatively low PLQY of the active layer and non-optimal device structure design. Tang's group attempted to improve the situation by using $Cs_2Ag_{0.6}Na_{0.4}InCl_6:Bi^{3+}$ films to fabricate electrically driven WLEDs, but the obtained EQEs were very low, indicating the need for further optimization of the device structure and materials[303].

In recent years, the remarkable photoluminescence and ambient stability of Cu-based low-dimensional structures have garnered significant attention for electrically pumped LEDs. In 2019, Hosono's group achieved a major milestone by successfully demonstrating the first-ever deep-blue LED that utilized $Cs_3Cu_2I_5$ films as the emitter. This LED emitted at a wavelength of 445 nm and exhibited CIE coordinates at (0.16, 0.07), meeting the stringent blue NTSC standard. The devices also displayed descent operation stability, with a half-lifetime (T_{50}) of 108 hours[238]. However, poor thin-film morphology of Cu-based compounds posed a major challenge in reducing the leakage current and improving device performance. Subsequently, the CsCu2I3- composition with yellow emission was also investigated for its potential use in functional LEDs[304]. Poor thin-film morphology of these Cu-based compounds remained a major challenge in reducing the leakage current, and subsequently improving the device performance. Recently, antisolvent treated uniform thin-films of $CsCu_2I_3$-based LEDs demonstrated an EQE of 0.17% and a luminance of 47.5 cd m^{-2}, representing a significant improvement [305]. Another breakthrough was achieved when Liu et al. reported mixed phases of $Cs_3Cu_2I_5$ and $CsCu_2I_3$ through antisolvent treatment, resulting in a WLED with a small onset voltage of 2.9 V and tunable CIE coordinates of (0.327, 0.348)[306]. The two-component strategy is further explored by Shi's group with $CsCu_2I_3@Cs_3Cu_2I_5$, as active layer that exhibited

tunable white light emission by adjusting the ratio of CuI/CsI. The tunable WLEDs also exhibited an excellent operation stability with a long T_{50} of ~238.5 min[307].

7 OUTLOOK

Nearly a decade ago, the first solid-state solar cell comprising lead-based halide perovskites was demonstrated. Since then, research efforts on halide perovskites have picked up considerably and the performance level of lead-based perovskite devices have rapidly improved. Nevertheless, heavy metal toxicity associated with lead remains one of the major environmental concerns for their wide-spread applications. While the research efforts are driven by the search for LHP replacement, lead-free halide compounds itself present a unique opportunity for high-performing, and solution-processable materials platform, which is well-suited for a range of optoelectronic applications. The recent results also showcased decent progress in terms of performance metrics. Nevertheless, a deeper understanding of the crystal structures, optoelectronic properties, and passivation strategies are currently missing, and more efforts are still required to unlock their full potential such that lead-free halide compounds can rival existing semiconductors, including LHPs in terms of optoelectronic device performances.

In this comprehensive review, we have highlighted the vast chemical space of lead-free halide compounds and made a compelling argument for the previously overlooked diversity of structures and properties. These structural tunability and compositional adjustment remains one of the major strengths in lead-free compounds which are neither limited by perovskite structure, nor Goldschmidt's tolerance factor. For example, perovskite-derivative compound $Cs_3Bi_2I_9$ can be easily converted into Ag_xBiI_{3+x} only by replacing Cs^+ with Ag^+ which leads to smaller bandgap, and better charge transport properties, and subsequently superior photovoltaic performances. Similarly, the discovery of hollow Sn-based halide perovskites exhibited much better ambient stability as compared to 3D analogues which can be considered a significant leap towards lead-free perovskite solar cells. These results unequivocally indicate that the crystal structure and composition can be readily manipulated to achieve desired

electronic, optical, and chemical properties. It showcases the immense potential in tuning the semiconducting properties which basically depend on the crystal structure and the chemical composition for targeted optoelectronic devices. However, it remains a challenge to achieve a perfect combination of semiconducting properties. While the exploratory discovery of novel functional materials often carried out by traditional laboratory-scale experimentation, recent progress on high-throughput computational methodologies accelerated the prediction of materials properties from chemical composition and structure manifold. Furthermore, recent advances in accelerated materials development such as in automated robot-assisted chemical space exploration has recently found momentum for lead-free research[308].

However, significant strides must be made in device fabrication to ensure the desired chemical and optoelectronic properties are reliably reproducible. Considering the bottleneck of charge transport properties, the low-dimensional structures could be employed for ultra-thin device architecture in which transport bottleneck can be physically overcome. A notable example is the ultrathin $Cs_3Bi_2I_9$ nanosheets which exhibited remarkable photovoltaic properties[256]. It should also be noted that high-quality solution-processed synthesis routes which have been extremely successful for lead-based halide perovskites, may not be directly translatable for different chemical spaces. Currently, several non-solution phase solid-state synthesis routes have gained interests such as mechano-synthesis, or ball-milling. While these techniques may not be suitable for thin-film device fabrication, they can offer a high-throughput synthesis environment to explore the lead-free halide chemical space. Apart from solid-state synthesis, high vacuum evaporation techniques or close-space sublimation which hold the key to industrial scale perovskite-based solar scale fabrication, have proved to be equally suitable for lead-free halide compounds [282, 309].

Another important characteristic is the defects in these halide compounds that play a crucial role in their macroscopic behavior, and understanding their dynamics is vital for future device development. The concentration, nature, and interactions of defects give rise to complex phenomena that cannot be captured by traditional density functional theory calculations or

simple averages. Therefore, a comprehensive understanding of these materials requires a holistic approach that combines optical and electrical characterizations supported by theoretical calculations. At present, there is no evidence that these compounds cannot be defect tolerant for normal synthesis environment and it is interesting of theoretical research that there is a consensus regarding the defect tolerance of halide perovskites. Experimental studies already indicated that the formation of defects can also be manipulated by the synthesis conditions which warrants further study in terms of synthesis strategies.

Expanding our understanding of highly confined electrons in low-dimensional structures presents exciting opportunities for advanced optoelectronic applications. However, harnessing these unique electronic and optical properties in high-performing devices remains a significant challenge that must be addressed to achieve optimal performance. Recent advancements in 3D non-perovskite structures highlight the vast untapped potential for new material discoveries. By applying external stimuli or replacing constitutive elements, one can finely tune optoelectronic properties, ultimately yielding new and functional materials such as in piezochromism[310] or nanogenerator[311].

Overall, halide compounds offer a vast array of structures and properties that can be tailored for specific optoelectronic applications. One of the major advantages of lead-free halide compounds is the near-infinite chemical space with rich structural diversity that can accommodate a wide range of optoelectronic applications. We expect more lead-free halide compounds will be developed/discovered and promising functional properties can be achieved. There is no doubt that a successful realization of lead-free halide compounds which effectively combine the great photophysical properties of the LHPs with the fascinating solution-processability, ambient stability, and nontoxicity will be a major breakthrough in the field of optoelectronic devices.

Acknowledgements

This research is supported by the National Research Foundation (NRF), Singapore, under its Competitive Research Program (CRP) (NRF-CRP25-2020-0002). BG would like to thank KU Leuven for PDM scholarship (PDMT1/22/011). M.B.J.R. acknowledge financial support from the KU Leuven Research Fund (C14/19/079, iBOF-21-085 PERSIST) and the Research Foundation – Flanders (G098319N, G0A5923N).

Author Declarations

Conflict of Interest

The authors have no conflicts to disclose.

Data Availability

The original data that support the findings of this study are available from the corresponding author upon reasonable request.

References

1. W. Petzold, Zeitschrift f&#65533;r anorganische und allgemeine Chemie **215** (1), 92-102 (1933).
2. A. Gutbier and M. Müller, Z. Anorg. Allg. Chem. **128** (1), 137-152 (1923).
3. R. P. Oertel and R. A. Plane, Inorg. Chem. **6** (11), 1960-1967 (1967).
4. R. G. Dickinson, J. Am. Chem. Soc. **44** (11), 2404-2411 (1922).
5. M. Maćkowiak, N. Weiden and A. Weiss, physica status solidi (a) **119** (1), 77-85 (1990).
6. G. Bator, J. Mróz and R. Jakubas, Physica B: Condensed Matter **240** (4), 362-371 (1997).
7. R. Jakubas and L. Sobczyk, Phase Transitions **20** (3-4), 163-193 (1990).
8. G. Thiele, H. W. Rotter and K. D. Schmidt, Zeitschrift f&#65533;r anorganische und allgemeine Chemie **545** (2), 148-156 (1987).
9. T. V. Sedakova, A. G. Mirochnik and V. E. Karasev, Opt. Spectrosc. **105** (4), 517-523 (2008).
10. N. V. Petrochenkova, T. V. Storozhuk, A. G. Mirochnik and V. E. Karasev, Russian Journal of Coordination Chemistry **28** (7), 468-472 (2002).
11. J. Jeong, M. Kim, J. Seo, H. Lu, P. Ahlawat, A. Mishra, Y. Yang, M. A. Hope, F. T. Eickemeyer, M. Kim, Y. J. Yoon, I. W. Choi, B. P. Darwich, S. J. Choi, Y. Jo, J. H. Lee, B. Walker, S. M. Zakeeruddin, L. Emsley, U. Rothlisberger, A. Hagfeldt, D. S. Kim, M. Grätzel and J. Y. Kim, Nature **592** (7854), 381-385 (2021).
12. A. Al-Ashouri, E. Köhnen, B. Li, A. Magomedov, H. Hempel, P. Caprioglio, J. A. Márquez, A. B. M. Vilches, E. Kasparavicius, J. A. Smith, N. Phung, D. Menzel, M. Grischek, L. Kegelmann, D. Skroblin, C. Gollwitzer, T. Malinauskas, M. Jošt, G. Matič, B. Rech, R. Schlatmann, M. Topič, L. Korte, A. Abate, B. Stannowski, D. Neher, M. Stolterfoht, T. Unold, V. Getautis and S. Albrecht, Science **370** (6522), 1300-1309 (2020).
13. Q. Zhang, F. Hao, J. Li, Y. Zhou, Y. Wei and H. Lin, Science and Technology of Advanced Materials **19** (1), 425-442 (2018).
14. G. Flora, D. Gupta and A. Tiwari, Interdisciplinary toxicology **5** (2), 47-58 (2012).
15. S. Fop, K. S. McCombie, E. J. Wildman, J. M. S. Skakle, J. T. S. Irvine, P. A. Connor, C. Savaniu, C. Ritter and A. C. McLaughlin, Nature Materials **19** (7), 752-757 (2020).
16. C. C. Stoumpos, L. Mao, C. D. Malliakas and M. G. Kanatzidis, Inorg. Chem. **56** (1), 56-73 (2017).
17. M.-H. Jung, New J. Chem. **44** (1), 171-180 (2020).
18. W. D. van Amstel and L. J. de Jongh, Solid State Commun. **11** (10), 1423-1429 (1972).
19. R. E. Brandt, J. R. Poindexter, P. Gorai, R. C. Kurchin, R. L. Z. Hoye, L. Nienhaus, M. W. B. Wilson, J. A. Polizzotti, R. Sereika, R. Žaltauskas, L. C. Lee, J. L. MacManus-Driscoll, M. Bawendi, V. Stevanović and T. Buonassisi, Chem. Mater. **29** (11), 4667-4674 (2017).
20. A. Zakutayev, C. M. Caskey, A. N. Fioretti, D. S. Ginley, J. Vidal, V. Stevanovic, E. Tea and S. Lany, The Journal of Physical Chemistry Letters **5** (7), 1117-1125 (2014).
21. W.-J. Yin, T. Shi and Y. Yan, Appl. Phys. Lett. **104** (6), 063903 (2014).
22. V. M. Goldschmidt, Naturwissenschaften **14** (21), 477-485 (1926).
23. W. Travis, E. N. K. Glover, H. Bronstein, D. O. Scanlon and R. G. Palgrave, Chemical Science **7** (7), 4548-4556 (2016).
24. A. I. Kitaigorodskii and C. Bureau, (1961).
25. E. G. Tulsky and J. R. Long, Chem. Mater. **13** (4), 1149-1166 (2001).
26. C. Zhou, Y. Tian, M. Wang, A. Rose, T. Besara, N. K. Doyle, Z. Yuan, J. C. Wang, R. Clark, Y. Hu, T. Siegrist, S. Lin and B. Ma, Angew. Chem. Int. Ed. Engl. **56** (31), 9018-9022 (2017).

27. L. Mao, C. C. Stoumpos and M. G. Kanatzidis, J. Am. Chem. Soc. **141** (3), 1171-1190 (2019).
28. M. Pitaro, E. K. Tekelenburg, S. Shao and M. A. Loi, Adv. Mater. **34** (1), 2105844 (2022).
29. W. P. D. Wong, J. V. Hanna and A. C. Grimsdale, Acta Crystallographica Section B **77** (3), 408-415 (2021).
30. G. Kieslich, S. Sun and A. K. Cheetham, Chemical Science **6** (6), 3430-3433 (2015).
31. T. Krishnamoorthy, H. Ding, C. Yan, W. L. Leong, T. Baikie, Z. Zhang, M. Sherburne, S. Li, M. Asta, N. Mathews and S. G. Mhaisalkar, Journal of Materials Chemistry A **3** (47), 23829-23832 (2015).
32. N. V. Sidgwick, *The Electronic Theory of Valency*. (Oxford University Press, 1932).
33. G. Thiele and B. R. Serr, Zeitschrift für Kristallographie-Crystalline Materials **210** (1), 64-64 (1995).
34. Y. Koji, F. Shinya, H. Hiromi, M. Takashi, O. Tsutomu and I. Sumio, Chem. Lett. **20** (5), 801-804 (1991).
35. I. Chung, J.-H. Song, J. Im, J. Androulakis, C. D. Malliakas, H. Li, A. J. Freeman, J. T. Kenney and M. G. Kanatzidis, J. Am. Chem. Soc. **134** (20), 8579-8587 (2012).
36. A. G. Kontos, A. Kaltzoglou, M. K. Arfanis, K. M. McCall, C. C. Stoumpos, B. W. Wessels, P. Falaras and M. G. Kanatzidis, The Journal of Physical Chemistry C **122** (46), 26353-26361 (2018).
37. S. Kahmann, O. Nazarenko, S. Shao, O. Hordiichuk, M. Kepenekian, J. Even, M. V. Kovalenko, G. R. Blake and M. A. Loi, ACS Energy Letters **5** (8), 2512-2519 (2020).
38. E. C. Schueller, G. Laurita, D. H. Fabini, C. C. Stoumpos, M. G. Kanatzidis and R. Seshadri, Inorg. Chem. **57** (2), 695-701 (2018).
39. S. Meloni, G. Palermo, N. Ashari-Astani, M. Grätzel and U. Rothlisberger, Journal of Materials Chemistry A **4** (41), 15997-16002 (2016).
40. Y. Takahashi, R. Obara, Z.-Z. Lin, Y. Takahashi, T. Naito, T. Inabe, S. Ishibashi and K. Terakura, Dalton Transactions **40** (20), 5563-5568 (2011).
41. G. Laurita, D. H. Fabini, C. C. Stoumpos, M. G. Kanatzidis and R. Seshadri, Chemical Science **8** (8), 5628-5635 (2017).
42. L. Peedikakkandy and P. Bhargava, RSC Advances **6** (24), 19857-19860 (2016).
43. L. M. Herz, ACS Energy Letters **2** (7), 1539-1548 (2017).
44. T. Liu, X. Zhao, J. Li, Z. Liu, F. Liscio, S. Milita, B. C. Schroeder and O. Fenwick, Nature Communications **10** (1), 5750 (2019).
45. T. Shi, H.-S. Zhang, W. Meng, Q. Teng, M. Liu, X. Yang, Y. Yan, H.-L. Yip and Y.-J. Zhao, Journal of Materials Chemistry A **5** (29), 15124-15129 (2017).
46. D. Ricciarelli, D. Meggiolaro, F. Ambrosio and F. De Angelis, ACS Energy Letters **5** (9), 2787-2795 (2020).
47. C. C. Stoumpos, C. D. Malliakas and M. G. Kanatzidis, Inorg. Chem. **52** (15), 9019-9038 (2013).
48. T.-B. Song, T. Yokoyama, C. C. Stoumpos, J. Logsdon, D. H. Cao, M. R. Wasielewski, S. Aramaki and M. G. Kanatzidis, J. Am. Chem. Soc. **139** (2), 836-842 (2017).
49. M. H. Kumar, S. Dharani, W. L. Leong, P. P. Boix, R. R. Prabhakar, T. Baikie, C. Shi, H. Ding, R. Ramesh, M. Asta, M. Graetzel, S. G. Mhaisalkar and N. Mathews, Adv. Mater. **26** (41), 7122-7127 (2014).
50. W. Ke, C. C. Stoumpos, I. Spanopoulos, M. Chen, M. R. Wasielewski and M. G. Kanatzidis, ACS Energy Letters **3** (7), 1470-1476 (2018).
51. W. Ke, C. C. Stoumpos, I. Spanopoulos, L. Mao, M. Chen, M. R. Wasielewski and M. G. Kanatzidis, J. Am. Chem. Soc. **139** (41), 14800-14806 (2017).
52. C.-M. Tsai, Y.-P. Lin, M. K. Pola, S. Narra, E. Jokar, Y.-W. Yang and E. W.-G. Diau, ACS Energy Letters **3** (9), 2077-2085 (2018).
53. U.-G. Jong, C.-J. Yu, Y.-H. Kye, Y.-G. Choe, W. Hao and S. Li, Inorg. Chem. **58** (7), 4134-4140 (2019).
54. C. C. Stoumpos, L. Frazer, D. J. Clark, Y. S. Kim, S. H. Rhim, A. J. Freeman, J. B. Ketterson, J. I. Jang and M. G. Kanatzidis, J. Am. Chem. Soc. **137** (21), 6804-6819 (2015).

55. G. Walters and E. H. Sargent, The Journal of Physical Chemistry Letters **9** (5), 1018-1027 (2018).
56. Y.-Q. Zhao, B. Liu, Z.-L. Yu, J. Ma, W. Qiang, P.-b. He and M.-Q. Cai, Journal of Materials Chemistry C **5** (22), 5356-5364 (2017).
57. P.-P. Sun, Q.-S. Li, L.-N. Yang and Z.-S. Li, Nanoscale **8** (3), 1503-1512 (2016).
58. W. Ming, H. Shi and M.-H. Du, Journal of Materials Chemistry A **4** (36), 13852-13858 (2016).
59. A. C. Dias, M. P. Lima and J. L. F. Da Silva, The Journal of Physical Chemistry C **125** (35), 19142-19155 (2021).
60. W. Meng, X. Wang, Z. Xiao, J. Wang, D. B. Mitzi and Y. Yan, The Journal of Physical Chemistry Letters **8** (13), 2999-3007 (2017).
61. G. Volonakis, M. R. Filip, A. A. Haghighirad, N. Sakai, B. Wenger, H. J. Snaith and F. Giustino, The Journal of Physical Chemistry Letters **7** (7), 1254-1259 (2016).
62. G. L. McPherson and K. Talluto, Solid State Commun. **43** (5), 331-334 (1982).
63. J. I. Uribe, D. Ramirez, J. M. Osorio-Guillén, J. Osorio and F. Jaramillo, The Journal of Physical Chemistry C **120** (30), 16393-16398 (2016).
64. T. J. Jacobsson, M. Pazoki, A. Hagfeldt and T. Edvinsson, The Journal of Physical Chemistry C **119** (46), 25673-25683 (2015).
65. M. Pazoki, T. J. Jacobsson, A. Hagfeldt, G. Boschloo and T. Edvinsson, Physical Review B **93** (14), 144105 (2016).
66. D. G. Nocera, L. R. Morss and J. A. Fahey, J. Inorg. Nucl. Chem. **42** (1), 55-59 (1980).
67. L. R. Morss, T. Schleid and G. Meyer, Inorg. Chim. Acta **140**, 109-112 (1987).
68. G. Meyer, Naturwissenschaften **65** (5), 258-258 (1978).
69. S. Hesse, J. Zimmermann, H. v. Seggern, H. Ehrenberg, H. Fuess, C. Fasel and R. Riedel, J. Appl. Phys. **100** (8), 083506 (2006).
70. Y. Cai, W. Xie, Y. T. Teng, P. C. Harikesh, B. Ghosh, P. Huck, K. A. Persson, N. Mathews, S. G. Mhaisalkar, M. Sherburne and M. Asta, Chem. Mater. **31** (15), 5392-5401 (2019).
71. M. T. Anderson, K. B. Greenwood, G. A. Taylor and K. R. Poeppelmeier, Prog. Solid State Chem. **22** (3), 197-233 (1993).
72. A. H. Slavney, T. Hu, A. M. Lindenberg and H. I. Karunadasa, J. Am. Chem. Soc. **138** (7), 2138-2141 (2016).
73. E. T. McClure, M. R. Ball, W. Windl and P. M. Woodward, Chem. Mater. **28** (5), 1348-1354 (2016).
74. N. R. Wolf, B. A. Connor, A. H. Slavney and H. I. Karunadasa, Angew. Chem. Int. Ed. Engl. **60** (30), 16264-16278 (2021).
75. J. Yang, P. Zhang and S.-H. Wei, The Journal of Physical Chemistry Letters **9** (1), 31-35 (2018).
76. T. Zhang, Z. Cai and S. Chen, ACS Applied Materials & Interfaces **12** (18), 20680-20690 (2020).
77. I. N. Flerov, M. V. Gorev, K. S. Aleksandrov, A. Tressaud, J. Grannec and M. Couzi, Materials Science and Engineering: R: Reports **24** (3), 81-151 (1998).
78. X.-G. Zhao, J.-H. Yang, Y. Fu, D. Yang, Q. Xu, L. Yu, S.-H. Wei and L. Zhang, J. Am. Chem. Soc. **139** (7), 2630-2638 (2017).
79. Z. Xiao, K.-Z. Du, W. Meng, J. Wang, D. B. Mitzi and Y. Yan, J. Am. Chem. Soc. **139** (17), 6054-6057 (2017).
80. B. Wu, W. Ning, Q. Xu, M. Manjappa, M. Feng, S. Ye, J. Fu, S. Lie, T. Yin, F. Wang, T. W. Goh, P. C. Harikesh, Y. K. E. Tay, Z. X. Shen, F. Huang, R. Singh, G. Zhou, F. Gao and T. C. Sum, Science Advances **7** (8), eabd3160 (2021).
81. A. D. Wright, L. R. V. Buizza, K. J. Savill, G. Longo, H. J. Snaith, M. B. Johnston and L. M. Herz, The Journal of Physical Chemistry Letters **12** (13), 3352-3360 (2021).
82. F. Ji, J. Klarbring, F. Wang, W. Ning, L. Wang, C. Yin, J. S. M. Figueroa, C. K. Christensen, M. Etter, T. Ederth, L. Sun, S. I. Simak, I. A. Abrikosov and F. Gao, Angew. Chem. Int. Ed. Engl. **59** (35), 15191-15194 (2020).

83. Z. Xiao, W. Meng, J. Wang and Y. Yan, ChemSusChem **9** (18), 2628-2633 (2016).
84. T. Li, X. Zhao, D. Yang, M.-H. Du and L. Zhang, Physical Review Applied **10** (4), 041001 (2018).
85. M. Delor, A. H. Slavney, N. R. Wolf, M. R. Filip, J. B. Neaton, H. I. Karunadasa and N. S. Ginsberg, ACS Energy Letters **5** (5), 1337-1345 (2020).
86. J. A. Steele, W. Pan, C. Martin, M. Keshavarz, E. Debroye, H. Yuan, S. Banerjee, E. Fron, D. Jonckheere, C. W. Kim, W. Baekelant, G. Niu, J. Tang, J. Vanacken, M. Van der Auweraer, J. Hofkens and M. B. J. Roeffaers, Adv. Mater. **30** (46), 1804450 (2018).
87. J. Yang, C. Bao, W. Ning, B. Wu, F. Ji, Z. Yan, Y. Tao, J.-M. Liu, T. C. Sum, S. Bai, J. Wang, W. Huang, W. Zhang and F. Gao, Advanced Optical Materials **7** (13), 1801732 (2019).
88. H. L. Wells, **s5-3** (17), 315-326 (1922).
89. N. Elliott and L. Pauling, J. Am. Chem. Soc. **60** (8), 1846-1851 (1938).
90. K. Norimichi, Bull. Chem. Soc. Jpn. **73** (7), 1445-1460 (2000).
91. N. Kojima, M. Hasegawa, H. Kitagawa, T. Kikegawa and O. Shimomura, J. Am. Chem. Soc. **116** (25), 11368-11374 (1994).
92. S. S. Hafner, N. Kojima, J. Stanek and L. Zhang, Phys. Lett. A **192** (5), 385-388 (1994).
93. B. Ghosh, B. Febriansyah, P. C. Harikesh, T. M. Koh, S. Hadke, L. H. Wong, J. England, S. G. Mhaisalkar and N. Mathews, Chem. Mater. **32** (15), 6318-6325 (2020).
94. L. Debbichi, S. Lee, H. Cho, A. M. Rappe, K.-H. Hong, M. S. Jang and H. Kim, Adv. Mater. **30** (12), 1707001 (2018).
95. H. Murasugi, S. Kumagai, H. Iguchi, M. Yamashita and S. Takaishi, Chemistry **25** (42), 9885-9891 (2019).
96. F. P. Doty, X. W. Zhou, P. Yang and M. A. Rodriguez, 2012.
97. Q. Hu, Z. Deng, M. Hu, A. Zhao, Y. Zhang, Z. Tan, G. Niu, H. Wu and J. Tang, Science China Chemistry **61** (12), 1581-1586 (2018).
98. K. Biswas and M.-H. Du, Physical Review B **86** (1), 014102 (2012).
99. B. Wu, M.-L. Yang, Y.-C. Yan, C.-G. Ma, H.-W. Zhang, M. G. Brik, M. D. Dramićanin, U. V. Valiev and M. Piasecki, J. Am. Ceram. Soc. **104** (3), 1489-1500 (2021).
100. J. Jin, M. C. Folgueras, M. Gao, S. Yu, S. Louisia, Y. Zhang, L. N. Quan, C. Chen, R. Zhang, F. Seeler, K. Schierle-Arndt and P. Yang, Nano Lett. **21** (12), 5415-5421 (2021).
101. M.-H. Tremblay, J. Bacsa, B. Zhao, F. Pulvirenti, S. Barlow and S. R. Marder, Chem. Mater. **31** (16), 6145-6153 (2019).
102. J. A. McNulty and P. J. I. Lightfoot, IUCrJ **8** (4), 485-513 (2021).
103. D. B. Mitzi, C. A. Feild, W. T. A. Harrison and A. M. Guloy, Nature **369** (6480), 467-469 (1994).
104. G. C. Papavassiliou, J. B. Koutselas and D. J. Lagouvardos, Zeitschrift für Naturforschung B **48** (7), 1013-1014 (1993).
105. G. C. Papavassiliou, Molecular Crystals and Liquid Crystals Science and Technology. Section A. Molecular Crystals and Liquid Crystals **286** (1), 231-238 (1996).
106. D. B. Mitzi, Chem. Mater. **8** (3), 791-800 (1996).
107. G. C. Papavassiliou, I. B. Koutselas, A. Terzis and M. H. Whangbo, Solid State Commun. **91** (9), 695-698 (1994).
108. J. L. Knutson, J. D. Martin and D. B. Mitzi, Inorg. Chem. **44** (13), 4699-4705 (2005).
109. A. Fraccarollo, L. Canti, L. Marchese and M. Cossi, J. Chem. Phys. **146** (23), 234703 (2017).
110. J.-H. Yang, Q. Yuan and B. I. Yakobson, The Journal of Physical Chemistry C **120** (43), 24682-24687 (2016).
111. A. Bala, A. K. Deb and V. Kumar, The Journal of Physical Chemistry C **122** (13), 7464-7473 (2018).
112. D. H. Cao, C. C. Stoumpos, T. Yokoyama, J. L. Logsdon, T.-B. Song, O. K. Farha, M. R. Wasielewski, J. T. Hupp and M. G. Kanatzidis, ACS Energy Letters **2** (5), 982-990 (2017).
113. S. Narra, C.-Y. Lin, A. Seetharaman, E. Jokar and E. W.-G. Diau, The Journal of Physical Chemistry Letters **12** (51), 12292-12299 (2021).

114. X. Chang, D. Marongiu, V. Sarritzu, N. Sestu, Q. Wang, S. Lai, A. Mattoni, A. Filippetti, F. Congiu, A. G. Lehmann, F. Quochi, M. Saba, A. Mura and G. Bongiovanni, Adv. Funct. Mater. **29** (31), 1903528 (2019).
115. P. Cheng, T. Wu, J. Zhang, Y. Li, J. Liu, L. Jiang, X. Mao, R.-F. Lu, W.-Q. Deng and K. Han, The Journal of Physical Chemistry Letters **8** (18), 4402-4406 (2017).
116. L. Ma, M.-G. Ju, J. Dai and X. C. Zeng, Nanoscale **10** (24), 11314-11319 (2018).
117. P. Cheng, T. Wu, J. Liu, W.-Q. Deng and K. Han, The Journal of Physical Chemistry Letters **9** (10), 2518-2522 (2018).
118. C. M. M. Soe, G. P. Nagabhushana, R. Shivaramaiah, H. Tsai, W. Nie, J.-C. Blancon, F. Melkonyan, D. H. Cao, B. Traoré, L. Pedesseau, M. Kepenekian, C. Katan, J. Even, T. J. Marks, A. Navrotsky, A. D. Mohite, C. C. Stoumpos and M. G. Kanatzidis, Proc Natl Acad Sci U S A **116** (1), 58-66 (2019).
119. N. Zibouche and M. S. Islam, ACS Applied Materials & Interfaces **12** (13), 15328-15337 (2020).
120. Y. Takahashi, R. Obara, K. Nakagawa, M. Nakano, J.-y. Tokita and T. Inabe, Chem. Mater. **19** (25), 6312-6316 (2007).
121. D. B. Mitzi, C. D. Dimitrakopoulos and L. L. Kosbar, Chem. Mater. **13** (10), 3728-3740 (2001).
122. Z. Xu, D. B. Mitzi, C. D. Dimitrakopoulos and K. R. Maxcy, Inorg. Chem. **42** (6), 2031-2039 (2003).
123. Z. Wang, Alex M. Ganose, C. Niu and D. O. Scanlon, Journal of Materials Chemistry A **6** (14), 5652-5660 (2018).
124. D. B. Mitzi, S. Wang, C. A. Feild, C. A. Chess and A. M. Guloy, Science **267** (5203), 1473-1476 (1995).
125. M.-G. Ju, J. Dai, L. Ma, Y. Zhou, W. Liang and X. C. Zeng, Journal of Materials Chemistry A **7** (28), 16742-16747 (2019).
126. T. Nakajima, H. Yamauchi, T. Goto, M. Yoshizawa, T. Suzuki and T. Fujimura, J. Magn. Magn. Mater. **31-34**, 1189-1190 (1983).
127. R. Mokhlisse, M. Couzi, N. B. Chanh, Y. Haget, C. Hauw and A. Meresse, J. Phys. Chem. Solids **46** (2), 187-195 (1985).
128. H. Z. Cummins, Physics Reports **185** (5), 211-409 (1990).
129. R. Geick, (Springer-Verlag Berlin Heidelberg).
130. D. Balz and K. Plieth, **59** (6), 545-551 (1955).
131. C. Brosset, Zeitschrift f**r anorganische und allgemeine Chemie **235** (1-2), 139-147 (1937).
132. S. Gupta, T. Pandey and A. K. Singh, Inorg. Chem. **55** (13), 6817-6824 (2016).
133. J. Han, S. Nishihara, K. Inoue and M. Kurmoo, Inorg. Chem. **54** (6), 2866-2874 (2015).
134. A. O. Polyakov, A. H. Arkenbout, J. Baas, G. R. Blake, A. Meetsma, A. Caretta, P. H. M. van Loosdrecht and T. T. M. Palstra, Chem. Mater. **24** (1), 133-139 (2012).
135. Y. Nakayama, S. Nishihara, K. Inoue, T. Suzuki and M. Kurmoo, Angew. Chem. Int. Ed. Engl. **56** (32), 9367-9370 (2017).
136. B. Kundys, A. Lappas, M. Viret, V. Kapustianyk, V. Rudyk, S. Semak, C. Simon and I. Bakaimi, Physical Review B **81** (22), 224434 (2010).
137. Y. Moritomo and Y. Tokura, The Journal of Chemical Physics **101** (3), 1763-1766 (1994).
138. A. Jaffe, Y. Lin, W. L. Mao and H. I. Karunadasa, J. Am. Chem. Soc. **137** (4), 1673-1678 (2015).
139. B. A. Connor, L. Leppert, M. D. Smith, J. B. Neaton and H. I. Karunadasa, J. Am. Chem. Soc. **140** (15), 5235-5240 (2018).
140. M. K. Jana, S. M. Janke, D. J. Dirkes, S. Dovletgeldi, C. Liu, X. Qin, K. Gundogdu, W. You, V. Blum and D. B. Mitzi, J. Am. Chem. Soc. **141** (19), 7955-7964 (2019).
141. Y. Yao, B. Kou, Y. Peng, Z. Wu, L. Li, S. Wang, X. Zhang, X. Liu and J. Luo, Chem. Commun. **56** (21), 3206-3209 (2020).

142. B. A. Connor, R. W. Smaha, J. Li, A. Gold-Parker, A. J. Heyer, M. F. Toney, Y. S. Lee and H. I. Karunadasa, Chemical Science **12** (25), 8689-8697 (2021).
143. L.-Y. Bi, T.-L. Hu, M.-Q. Li, B.-K. Ling, M. S. Lassoued, Y.-Q. Hu, Z. Wu, G. Zhou and Y.-Z. Zheng, Journal of Materials Chemistry A **8** (15), 7288-7296 (2020).
144. L. Mao, S. M. L. Teicher, C. C. Stoumpos, R. M. Kennard, R. A. DeCrescent, G. Wu, J. A. Schuller, M. L. Chabinyc, A. K. Cheetham and R. Seshadri, J. Am. Chem. Soc. **141** (48), 19099-19109 (2019).
145. E. T. McClure, A. P. McCormick and P. M. Woodward, Inorg. Chem. **59** (9), 6010-6017 (2020).
146. L. M. Castro-Castro and A. M. Guloy, Angew. Chem. Int. Ed. **42** (24), 2771-2774 (2003).
147. B. A. Connor, R.-I. Biega, L. Leppert and H. I. Karunadasa, Chemical Science **11** (29), 7708-7715 (2020).
148. J. Guan, Z. Tang and A. M. Guloy, Chem. Commun. (18), 1833-1834 (1999).
149. M. Daub, C. Haber and H. Hillebrecht, Eur. J. Inorg. Chem. **2017** (7), 1120-1126 (2017).
150. B. Febriansyah, Y. Lekina, J. Kaur, T. J. N. Hooper, P. C. Harikesh, T. Salim, M. H. Lim, T. M. Koh, S. Chakraborty, Z. X. Shen, N. Mathews and J. England, ACS Nano **15** (4), 6395-6409 (2021).
151. S. Wang, D. B. Mitzi, C. A. Feild and A. Guloy, J. Am. Chem. Soc. **117** (19), 5297-5302 (1995).
152. J. A. McNulty and P. Lightfoot, Chem. Commun. **56** (33), 4543-4546 (2020).
153. B. Saparov, F. Hong, J.-P. Sun, H.-S. Duan, W. Meng, S. Cameron, I. G. Hill, Y. Yan and D. B. Mitzi, Chem. Mater. **27** (16), 5622-5632 (2015).
154. J.-H. Chang, T. Doert and M. Ruck, Z. Anorg. Allg. Chem. **642** (13), 736-748 (2016).
155. A. J. Lehner, D. H. Fabini, H. A. Evans, C.-A. Hébert, S. R. Smock, J. Hu, H. Wang, J. W. Zwanziger, M. L. Chabinyc and R. Seshadri, Chem. Mater. **27** (20), 7137-7148 (2015).
156. S. Sun, S. Tominaka, J.-H. Lee, F. Xie, P. D. Bristowe and A. K. Cheetham, APL Materials **4** (3), 031101 (2016).
157. P. C. Harikesh, H. K. Mulmudi, B. Ghosh, T. W. Goh, Y. T. Teng, K. Thirumal, M. Lockrey, K. Weber, T. M. Koh, S. Li, S. Mhaisalkar and N. Mathews, Chem. Mater. **28** (20), 7496-7504 (2016).
158. F. Umar, J. Zhang, Z. Jin, I. Muhammad, X. Yang, H. Deng, K. Jahangeer, Q. Hu, H. Song and J. Tang, Advanced Optical Materials **7** (5), 1801368 (2019).
159. J. Zhang, Y. Yang, H. Deng, U. Farooq, X. Yang, J. Khan, J. Tang and H. Song, ACS Nano **11** (9), 9294-9302 (2017).
160. M. B. Johansson, H. Zhu and E. M. J. Johansson, The Journal of Physical Chemistry Letters **7** (17), 3467-3471 (2016).
161. B. Vargas, E. Ramos, E. Pérez-Gutiérrez, J. C. Alonso and D. Solis-Ibarra, J. Am. Chem. Soc. **139** (27), 9116-9119 (2017).
162. B. Vargas, R. Torres-Cadena, J. Rodríguez-Hernández, M. Gembicky, H. Xie, J. Jiménez-Mier, Y.-S. Liu, E. Menéndez-Proupin, K. R. Dunbar, N. Lopez, P. Olalde-Velasco and D. Solis-Ibarra, Chem. Mater. **30** (15), 5315-5321 (2018).
163. G. Tang, Z. Xiao, H. Hosono, T. Kamiya, D. Fang and J. Hong, The Journal of Physical Chemistry Letters **9** (1), 43-48 (2018).
164. J. Xu, J.-B. Liu, J. Wang, B.-X. Liu and B. Huang, Adv. Funct. Mater. **28** (26), 1800332 (2018).
165. S. Hu, B. Xia, Y.-P. Lin, T. Katase, J. Fujioka, T. Kamiya, H. Hosono, K.-Z. Du and Z. Xiao, Adv. Funct. Mater. **30** (31), 1909906 (2020).
166. Z. Liu, X. Zhao, A. Zunger and L. Zhang, Advanced Electronic Materials **5** (6), 1900234 (2019).
167. D. B. Mitzi, K. Liang and S. Wang, Inorg. Chem. **37** (2), 321-327 (1998).
168. M.-Q. Li, Y.-Q. Hu, L.-Y. Bi, H.-L. Zhang, Y. Wang and Y.-Z. Zheng, Chem. Mater. **29** (13), 5463-5467 (2017).
169. G. C. Allen and R. F. McMeeking, Inorg. Chim. Acta **23**, 185-190 (1977).

170. M. Bujak and J. Zaleski, Acta Crystallographica Section C **55** (11), 1775-1778 (1999).
171. A. Lipka, Z. Anorg. Allg. Chem. **469** (1), 218-228 (1980).
172. F. Cariati, A. Panzanelli, L. Antolini, L. Menabue, G. C. Pellacani and G. Marcotrigiano, J. Chem. Soc., Dalton Trans. (4), 909-913 (1981).
173. K. Tao, Y. Li, C. Ji, X. Liu, Z. Wu, S. Han, Z. Sun and J. Luo, Chem. Mater. **31** (15), 5927-5932 (2019).
174. A. Ouasri, A. Rhandour, M. Saadi and L. El Ammari, Acta Crystallographica Section E **69** (8), m437 (2013).
175. J. Zaleski and A. Pietraszko, J. Mol. Struct. **327** (2), 287-295 (1994).
176. A. Angeloni, P. C. Crawford, A. G. Orpen, T. J. Podesta and B. J. Shore, Chemistry – A European Journal **10** (15), 3783-3791 (2004).
177. J. K. Pious, M. G. Basavarajappa, C. Muthu, N. Krishna, R. Nishikubo, A. Saeki, S. Chakraborty and C. Vijayakumar, The Journal of Physical Chemistry Letters **11** (16), 6757-6762 (2020).
178. A. Biswas, R. Bakthavatsalam, S. R. Shaikh, A. Shinde, A. Lohar, S. Jena, R. G. Gonnade and J. Kundu, Chem. Mater. **31** (7), 2253-2257 (2019).
179. S. W. Eaton, A. Fu, A. B. Wong, C.-Z. Ning and P. Yang, Nature Reviews Materials **1** (6), 16028 (2016).
180. T. Qiu, Y. Hu, F. Xu, Z. Yan, F. Bai, G. Jia and S. Zhang, Nanoscale **10** (45), 20963-20989 (2018).
181. M. Krupski, Physica Status Solidi (a) **78** (2), 751-758 (1983).
182. R. L. Armstrong, Physics Reports **57** (6), 343-396 (1980).
183. A. Burger, E. Rowe, M. Groza, K. M. Figueroa, N. J. Cherepy, P. R. Beck, S. Hunter and S. A. Payne, Appl. Phys. Lett. **107** (14), 143505 (2015).
184. I. D. Brown, Can. J. Chem. **42** (12), 2758-2767 (1964).
185. in *Structure and Chemistry of Crystalline Solids* (Springer New York, New York, NY, 2006), pp. 117-146.
186. W. Abriel, Zeitschrift für Naturforschung B **42** (4), 415-420 (1987).
187. B. Lee, C. C. Stoumpos, N. Zhou, F. Hao, C. Malliakas, C.-Y. Yeh, T. J. Marks, M. G. Kanatzidis and R. P. H. Chang, J. Am. Chem. Soc. **136** (43), 15379-15385 (2014).
188. F. Guo, Z. Lu, D. Mohanty, T. Wang, I. B. Bhat, S. Zhang, S. Shi, M. A. Washington, G.-C. Wang and T.-M. Lu, Materials Research Letters **5** (8), 540-546 (2017).
189. X. Qiu, B. Cao, S. Yuan, X. Chen, Z. Qiu, Y. Jiang, Q. Ye, H. Wang, H. Zeng, J. Liu and M. G. Kanatzidis, Sol. Energy Mater. Sol. Cells **159**, 227-234 (2017).
190. J. C.-R. Ke, D. J. Lewis, A. S. Walton, B. F. Spencer, P. O'Brien, A. G. Thomas and W. R. Flavell, Journal of Materials Chemistry A **6** (24), 11205-11214 (2018).
191. H. Shin, B.-M. Kim, T. Jang, K. M. Kim, D.-H. Roh, J. S. Nam, J. S. Kim, U.-Y. Kim, B. Lee, Y. Pang and T.-H. Kwon, Advanced Energy Materials **9** (3), 1803243 (2019).
192. A. Liu, H. Zhu, Y. Reo, M.-G. Kim, H. Y. Chu, J. H. Lim, H.-J. Kim, W. Ning, S. Bai and Y.-Y. Noh, Cell Reports Physical Science **3** (4), 100812 (2022).
193. G. Wang, D. Wang and X. Shi, AIP Advances **5** (12), 127224 (2015).
194. M.-G. Ju, M. Chen, Y. Zhou, H. F. Garces, J. Dai, L. Ma, N. P. Padture and X. C. Zeng, ACS Energy Letters **3** (2), 297-304 (2018).
195. Z. Xiao, H. Lei, X. Zhang, Y. Zhou, H. Hosono and T. Kamiya, Bulletin of the Chemical Society of Japan **88** (9), 1250-1255 (2015).
196. A. E. Maughan, A. M. Ganose, M. M. Bordelon, E. M. Miller, D. O. Scanlon and J. R. Neilson, J. Am. Chem. Soc. **138** (27), 8453-8464 (2016).
197. R. J. D. Tilley, in *Perovskites* (2016), pp. 79-122.
198. A. D. Raw, J. A. Ibers and K. R. Poeppelmeier, J. Solid State Chem. **192**, 34-37 (2012).
199. H. Tanaka, K. Iio and K. Nagata, J. Magn. Magn. Mater. **104-107**, 829-830 (1992).
200. M. Daub, I. Ketterer and H. Hillebrecht, Z. Anorg. Allg. Chem. **644** (5), 280-287 (2018).

201. X. Tan, P. W. Stephens, M. Hendrickx, J. Hadermann, C. U. Segre, M. Croft, C.-J. Kang, Z. Deng, S. H. Lapidus, S. W. Kim, C. Jin, G. Kotliar and M. Greenblatt, Chem. Mater. **31** (6), 1981-1989 (2019).
202. L. Yao, Z. Zeng, C. Cai, P. Xu, H. Gu, L. Gao, J. Han, X. Zhang, X. Wang, X. Wang, A. Pan, J. Wang, W. Liang, S. Liu, C. Chen and J. Tang, J. Am. Chem. Soc. **143** (39), 16095-16104 (2021).
203. G. Xu, G.-C. Guo, M.-S. Wang, Z.-J. Zhang, W.-T. Chen and J.-S. Huang, Angew. Chem. Int. Ed. Engl. **46** (18), 3249-3251 (2007).
204. W.-Q. Liao, Y.-Y. Tang, P.-F. Li, Y.-M. You and R.-G. Xiong, J. Am. Chem. Soc. **140** (11), 3975-3980 (2018).
205. M. Bourwina, R. Msalmi, S. Walha, M. M. Turnbull, T. Roisnel, F. Costantino, E. Mosconi and H. Naïli, Journal of Materials Chemistry C **9** (18), 5970-5976 (2021).
206. I. W. H. Oswald, E. M. Mozur, I. P. Moseley, H. Ahn and J. R. Neilson, Inorg. Chem. **58** (9), 5818-5826 (2019).
207. T. Li, Y. Hu, C. A. Morrison, W. Wu, H. Han and N. Robertson, Sustainable Energy & Fuels **1** (2), 308-316 (2017).
208. R.-Y. Zhao, G.-N. Liu, Q.-S. Liu, P.-F. Niu, R.-D. Xu, Z.-H. Wang, T.-H. Wei, J. Zhang, Y.-Q. Sun and C. Li, Crystal Growth & Design **20** (2), 1009-1015 (2020).
209. J. A. Zienkiewicz, M. Ptak, D. Drozdowski, K. Fedoruk, M. Stefanski and A. Pikul, The Journal of Physical Chemistry C **126** (37), 15809-15818 (2022).
210. P. S. Ghosh, J. Doherty, S. Lisenkov and I. Ponomareva, The Journal of Physical Chemistry C **125** (29), 16296-16303 (2021).
211. X.-F. Sun, P.-F. Li, W.-Q. Liao, Z. Wang, J. Gao, H.-Y. Ye and Y. Zhang, Inorganic Chemistry **56** (20), 12193-12198 (2017).
212. Y. Zhang, W.-Q. Liao, D.-W. Fu, H.-Y. Ye, Z.-N. Chen and R.-G. Xiong, J. Am. Chem. Soc. **137** (15), 4928-4931 (2015).
213. H.-Y. Ye, Q. Zhou, X. Niu, W.-Q. Liao, D.-W. Fu, Y. Zhang, Y.-M. You, J. Wang, Z.-N. Chen and R.-G. Xiong, Journal of the American Chemical Society **137** (40), 13148-13154 (2015).
214. I. Spanopoulos, I. Hadar, W. Ke, P. Guo, S. Sidhik, M. Kepenekian, J. Even, A. D. Mohite, R. D. Schaller and M. G. Kanatzidis, J. Am. Chem. Soc. **142** (19), 9028-9038 (2020).
215. S. A. Adonin, E. V. Peresypkina, M. N. Sokolov and V. P. Fedin, J. Struct. Chem. **56** (4), 795-799 (2015).
216. W.-G. Li, X.-D. Wang, J.-F. Liao, Y. Jiang and D.-B. Kuang, Adv. Funct. Mater. **30** (12), 1909701 (2020).
217. K. M. McCall, Z. Liu, G. Trimarchi, C. C. Stoumpos, W. Lin, Y. He, I. Hadar, M. G. Kanatzidis and B. W. Wessels, ACS Photonics **5** (9), 3748-3762 (2018).
218. Q. Sun, Y. Xu, H. Zhang, B. Xiao, X. Liu, J. Dong, Y. Cheng, B. Zhang, W. Jie and M. G. Kanatzidis, Journal of Materials Chemistry A **6** (46), 23388-23395 (2018).
219. S. Dong, D. Xin, M. Zhang, S. Tie, B. Cai, Q. Ma and X. Zheng, Journal of Materials Chemistry C **10** (16), 6236-6242 (2022).
220. D. Ju, X. Jiang, H. Xiao, X. Chen, X. Hu and X. Tao, Journal of Materials Chemistry A **6** (42), 20753-20759 (2018).
221. C. Delmas, C. Fouassier and P. Hagenmuller, Physica B+C **99** (1), 81-85 (1980).
222. H. C. Sansom, G. F. S. Whitehead, M. S. Dyer, M. Zanella, T. D. Manning, M. J. Pitcher, T. J. Whittles, V. R. Dhanak, J. Alaria, J. B. Claridge and M. J. Rosseinsky, Chem. Mater. **29** (4), 1538-1549 (2017).
223. A. Koedtruad, M. Goto, M. Amano Patino, Z. Tan, H. Guo, T. Nakamura, T. Handa, W.-T. Chen, Y.-C. Chuang, H.-S. Sheu, T. Saito, D. Kan, Y. Kanemitsu, A. Wakamiya and Y. Shimakawa, Journal of Materials Chemistry A **7** (10), 5583-5588 (2019).
224. I. Turkevych, S. Kazaoui, E. Ito, T. Urano, K. Yamada, H. Tomiyasu, H. Yamagishi, M. Kondo and S. Aramaki, ChemSusChem **10** (19), 3754-3759 (2017).
225. A. Okada and K. Keil, Am. Mineral. **67** (1-2), 132-136 (1982).

226. H. C. Sansom, L. R. V. Buizza, M. Zanella, J. T. Gibbon, M. J. Pitcher, M. S. Dyer, T. D. Manning, V. R. Dhanak, L. M. Herz, H. J. Snaith, J. B. Claridge and M. J. Rosseinsky, Inorg. Chem. **60** (23), 18154-18167 (2021).
227. P. H. Fourcroy, D. Carre, F. Thevet and J. Rivet, Acta Crystallographica Section C **47** (10), 2023-2025 (1991).
228. Z. Bahari, F. Thévet, J. Rivet and J. J. J. J. d. E. d. E. e. P. Dugué, 00020 (2009).
229. H. C. Sansom, G. Longo, A. D. Wright, L. R. V. Buizza, S. Mahesh, B. Wenger, M. Zanella, M. Abdi-Jalebi, M. J. Pitcher, M. S. Dyer, T. D. Manning, R. H. Friend, L. M. Herz, H. J. Snaith, J. B. Claridge and M. J. Rosseinsky, J. Am. Chem. Soc. **143** (10), 3983-3992 (2021).
230. L. Wang, Y. Bao, S. Wang, F. Wang, C. Xie, K. T. Butler and X. Fan, Crystal Growth & Design **21** (5), 2850-2855 (2021).
231. H. Zhu, A. Erbing, H. Wu, G. J. Man, S. Mukherjee, C. Kamal, M. B. Johansson, H. Rensmo, M. Odelius and E. M. J. Johansson, ACS Applied Energy Materials **3** (8), 7372-7382 (2020).
232. M. B. Gray, E. T. McClure, N. P. Holzapfel, F. P. Evaristo, W. Windl and P. M. Woodward, J. Solid State Chem. **297**, 121997 (2021).
233. X. Jia and L. Ding, Science China Materials **62** (1), 54-58 (2019).
234. B. Ghosh, B. Wu, X. Guo, P. C. Harikesh, R. A. John, T. Baikie, Arramel, A. T. S. Wee, C. Guet, T. C. Sum, S. Mhaisalkar and N. Mathews, Advanced Energy Materials **8** (33), 1802051 (2018).
235. Q. Zhang, C. Wu, X. Qi, F. Lv, Z. Zhang, Y. Liu, S. Wang, B. Qu, Z. Chen and L. Xiao, ACS Applied Energy Materials **2** (5), 3651-3656 (2019).
236. M. Khazaee, K. Sardashti, C.-C. Chung, J.-P. Sun, H. Zhou, E. Bergmann, W. A. Dunlap-Shohl, Q. Han, I. G. Hill, Jacob L. Jones, D. C. Lupascu and D. B. Mitzi, Journal of Materials Chemistry A **7** (5), 2095-2105 (2019).
237. R. Peng, M. Li and D. Li, Coord. Chem. Rev. **254** (1), 1-18 (2010).
238. T. Jun, K. Sim, S. Iimura, M. Sasase, H. Kamioka, J. Kim and H. Hosono, Adv. Mater. **30** (43), 1804547 (2018).
239. J. Li, T. Inoshita, T. Ying, A. Ooishi, J. Kim and H. Hosono, Adv. Mater. **32** (37), 2002945 (2020).
240. Z. Xing, Z. Zhou, G. Zhong, C. C. S. Chan, Y. Li, X. Zou, J. E. Halpert, H. Su and K. S. Wong, Adv. Funct. Mater. **n/a** (n/a), 2207638 (2022).
241. N. K. Noel, S. D. Stranks, A. Abate, C. Wehrenfennig, S. Guarnera, A.-A. Haghighirad, A. Sadhanala, G. E. Eperon, S. K. Pathak, M. B. Johnston, A. Petrozza, L. M. Herz and H. J. Snaith, Energy & Environmental Science **7** (9), 3061-3068 (2014).
242. P. Xu, S. Chen, H.-J. Xiang, X.-G. Gong and S.-H. Wei, Chem. Mater. **26** (20), 6068-6072 (2014).
243. J. Pascual, D. Di Girolamo, M. A. Flatken, M. H. Aldamasy, G. Li, M. Li and A. Abate, Chemistry **n/a** (n/a), e202103919 (2022).
244. J. Pascual, M. Flatken, R. Félix, G. Li, S.-H. Turren-Cruz, M. H. Aldamasy, C. Hartmann, M. Li, D. Di Girolamo, G. Nasti, E. Hüsam, R. G. Wilks, A. Dallmann, M. Bär, A. Hoell and A. Abate, Angew. Chem. Int. Ed. Engl. **60** (39), 21583-21591 (2021).
245. L. Ma, F. Hao, C. C. Stoumpos, B. T. Phelan, M. R. Wasielewski and M. G. Kanatzidis, J. Am. Chem. Soc. **138** (44), 14750-14755 (2016).
246. J. Qiu, Y. Xia, Y. Zheng, W. Hui, H. Gu, W. Yuan, H. Yu, L. Chao, T. Niu, Y. Yang, X. Gao, Y. Chen and W. Huang, ACS Energy Letters **4** (7), 1513-1520 (2019).
247. B.-B. Yu, Z. Chen, Y. Zhu, Y. Wang, B. Han, G. Chen, X. Zhang, Z. Du and Z. He, Adv. Mater. **33** (36), 2102055 (2021).
248. I. Spanopoulos, W. Ke, C. C. Stoumpos, E. C. Schueller, O. Y. Kontsevoi, R. Seshadri and M. G. Kanatzidis, J. Am. Chem. Soc. **140** (17), 5728-5742 (2018).
249. W. Ke, C. C. Stoumpos, M. Zhu, L. Mao, I. Spanopoulos, J. Liu, O. Y. Kontsevoi, M. Chen, D. Sarma, Y. Zhang, M. R. Wasielewski and M. G. Kanatzidis, Sci Adv **3** (8), e1701293 (2017).

250. I. Kopacic, B. Friesenbichler, S. F. Hoefler, B. Kunert, H. Plank, T. Rath and G. Trimmel, ACS Applied Energy Materials **1** (2), 343-347 (2018).
251. M. Chen, M.-G. Ju, H. F. Garces, A. D. Carl, L. K. Ono, Z. Hawash, Y. Zhang, T. Shen, Y. Qi, R. L. Grimm, D. Pacifici, X. C. Zeng, Y. Zhou and N. P. Padture, Nature Communications **10** (1), 16 (2019).
252. B.-W. Park, B. Philippe, X. Zhang, H. Rensmo, G. Boschloo and E. M. J. Johansson, Adv. Mater. **27** (43), 6806-6813 (2015).
253. R. L. Z. Hoye, R. E. Brandt, A. Osherov, V. Stevanović, S. D. Stranks, M. W. B. Wilson, H. Kim, A. J. Akey, J. D. Perkins, R. C. Kurchin, J. R. Poindexter, E. N. Wang, M. G. Bawendi, V. Bulović and T. Buonassisi, Chemistry **22** (8), 2605-2610 (2016).
254. B. Ghosh, B. Wu, H. K. Mulmudi, C. Guet, K. Weber, T. C. Sum, S. Mhaisalkar and N. Mathews, ACS Applied Materials & Interfaces **10** (41), 35000-35007 (2018).
255. B. Ghosh, S. Chakraborty, H. Wei, C. Guet, S. Li, S. Mhaisalkar and N. Mathews, The Journal of Physical Chemistry C **121** (32), 17062-17067 (2017).
256. F. Bai, Y. Hu, Y. Hu, T. Qiu, X. Miao and S. Zhang, Sol. Energy Mater. Sol. Cells **184**, 15-21 (2018).
257. P. C. Harikesh, B. Wu, B. Ghosh, R. A. John, S. Lie, K. Thirumal, L. H. Wong, T. C. Sum, S. Mhaisalkar and N. Mathews, Adv. Mater. **30** (34), 1802080 (2018).
258. Y. Yang, C. Liu, M. Cai, Y. Liao, Y. Ding, S. Ma, X. Liu, M. Guli, S. Dai and M. K. Nazeeruddin, ACS Applied Materials & Interfaces **12** (14), 17062-17069 (2020).
259. S. A. Adonin, L. A. Frolova, M. N. Sokolov, G. V. Shilov, D. V. Korchagin, V. P. Fedin, S. M. Aldoshin, K. J. Stevenson and P. A. Troshin, Advanced Energy Materials **8** (6), 1701140 (2018).
260. X. Yang, Y. Chen, P. Liu, H. Xiang, W. Wang, R. Ran, W. Zhou and Z. Shao, Adv. Funct. Mater. **30** (23), 2001557 (2020).
261. W. Ning, F. Wang, B. Wu, J. Lu, Z. Yan, X. Liu, Y. Tao, J.-M. Liu, W. Huang, M. Fahlman, L. Hultman, T. C. Sum and F. Gao, Adv. Mater. **30** (20), 1706246 (2018).
262. N. Pai, J. Lu, T. R. Gengenbach, A. Seeber, A. S. R. Chesman, L. Jiang, D. C. Senevirathna, P. C. Andrews, U. Bach, Y.-B. Cheng and A. N. Simonov, Advanced Energy Materials **9** (5), 1803396 (2019).
263. C.-K. Liu, Q. Tai, N. Wang, G. Tang, H.-L. Loi and F. Yan, Adv Sci (Weinh) **6** (17), 1900751 (2019).
264. A. Waleed, M. M. Tavakoli, L. Gu, Z. Wang, D. Zhang, A. Manikandan, Q. Zhang, R. Zhang, Y.-L. Chueh and Z. Fan, Nano Lett. **17** (1), 523-530 (2017).
265. J. Zhou, J. Luo, X. Rong, P. Wei, M. S. Molokeev, Y. Huang, J. Zhao, Q. Liu, X. Zhang, J. Tang and Z. Xia, Advanced Optical Materials **7** (10), 1900139 (2019).
266. X.-W. Tong, W.-Y. Kong, Y.-Y. Wang, J.-M. Zhu, L.-B. Luo and Z.-H. Wang, ACS Applied Materials & Interfaces **9** (22), 18977-18985 (2017).
267. Z.-X. Zhang, C. Li, Y. Lu, X.-W. Tong, F.-X. Liang, X.-Y. Zhao, D. Wu, C. Xie and L.-B. Luo, The Journal of Physical Chemistry Letters **10** (18), 5343-5350 (2019).
268. Y. He, I. Hadar and M. G. Kanatzidis, Nature Photonics **16** (1), 14-26 (2022).
269. W. Pan, H. Wu, J. Luo, Z. Deng, C. Ge, C. Chen, X. Jiang, W.-J. Yin, G. Niu, L. Zhu, L. Yin, Y. Zhou, Q. Xie, X. Ke, M. Sui and J. Tang, Nature Photonics **11** (11), 726-732 (2017).
270. H. Li, X. Shan, J. N. Neu, T. Geske, M. Davis, P. Mao, K. Xiao, T. Siegrist and Z. Yu, Journal of Materials Chemistry C **6** (44), 11961-11967 (2018).
271. R. Zhuang, X. Wang, W. Ma, Y. Wu, X. Chen, L. Tang, H. Zhu, J. Liu, L. Wu, W. Zhou, X. Liu and Y. Yang, Nature Photonics **13** (9), 602-608 (2019).
272. Z. Xu, X. Liu, Y. Li, X. Liu, T. Yang, C. Ji, S. Han, Y. Xu, J. Luo and Z. Sun, Angew. Chem. Int. Ed. Engl. **58** (44), 15757-15761 (2019).
273. M. Xia, J.-H. Yuan, G. Niu, X. Du, L. Yin, W. Pan, J. Luo, Z. Li, H. Zhao, K.-H. Xue, X. Miao and J. Tang, Adv. Funct. Mater. **30** (24), 1910648 (2020).
274. Y. Zhang, Y. Liu, Z. Xu, H. Ye, Z. Yang, J. You, M. Liu, Y. He, M. G. Kanatzidis and S. Liu, Nature Communications **11** (1), 2304 (2020).

275. Y. Liu, Z. Xu, Z. Yang, Y. Zhang, J. Cui, Y. He, H. Ye, K. Zhao, H. Sun, R. Lu, M. Liu, M. G. Kanatzidis and S. Liu, Matter **3** (1), 180-196 (2020).
276. J. Cao, Z. Guo, S. Zhu, Y. Fu, H. Zhang, Q. Wang and Z. Gu, ACS Applied Materials & Interfaces **12** (17), 19797-19804 (2020).
277. H. Hardhienata, F. Ahmad, Arramel, M. Aminah, D. Onggo, L. J. Diguna, M. D. Birowosuto, M. E. Witkowski, M. Makowski and W. Drozdowski, J. Phys. D: Appl. Phys. **53** (45), 455303 (2020).
278. J.-Y. Li, C.-F. Wang, H. Wu, L. Liu, Q.-L. Xu, S.-Y. Ye, L. Tong, X. Chen, Q. Gao, Y.-L. Hou, F.-M. Wang, J. Tang, L.-Z. Chen and Y. Zhang, Adv. Funct. Mater. **31** (35), 2102848 (2021).
279. T. Jiang, W. Ma, H. Zhang, Y. Tian, G. Lin, W. Xiao, X. Yu, J. Qiu, X. Xu, Y. Yang and D. Ju, Adv. Funct. Mater. **31** (14), 2009973 (2021).
280. L.-J. Xu, X. Lin, Q. He, M. Worku and B. Ma, Nature Communications **11** (1), 4329 (2020).
281. B. Yang, L. Yin, G. Niu, J.-H. Yuan, K.-H. Xue, Z. Tan, X.-S. Miao, M. Niu, X. Du, H. Song, E. Lifshitz and J. Tang, Adv. Mater. **31** (44), 1904711 (2019).
282. M. Zhang, J. Zhu, B. Yang, G. Niu, H. Wu, X. Zhao, L. Yin, T. Jin, X. Liang and J. Tang, Nano Lett. **21** (3), 1392-1399 (2021).
283. Z. Zhang, X. Guo, K. Huang, X. Sun, X. Li, H. Zeng, X. Zhu, Y. Zhang and R. Xie, J. Lumin. **241**, 118500 (2022).
284. Y. Wu, D. Han, B. C. Chakoumakos, H. Shi, S. Chen, M.-H. Du, I. Greeley, M. Loyd, D. J. Rutstrom, L. Stand, M. Koschan and C. L. Melcher, Journal of Materials Chemistry C **6** (25), 6647-6655 (2018).
285. W. Zhu, W. Ma, Y. Su, Z. Chen, X. Chen, Y. Ma, L. Bai, W. Xiao, T. Liu, H. Zhu, X. Liu, H. Liu, X. Liu and Y. Yang, Light: Science & Applications **9** (1), 112 (2020).
286. L. Lian, X. Wang, P. Zhang, J. Zhu, X. Zhang, J. Gao, S. Wang, G. Liang, D. Zhang, L. Gao, H. Song, R. Chen, X. Lan, W. Liang, G. Niu, J. Tang and J. Zhang, The Journal of Physical Chemistry Letters **12** (29), 6919-6926 (2021).
287. Q. Zhou, J. Ren, J. Xiao, L. Lei, F. Liao, H. Di, C. Wang, L. Yang, Q. Chen, X. Yang, Y. Zhao and X. Han, Nanoscale **13** (47), 19894-19902 (2021).
288. S. Cheng, A. Beitlerova, R. Kucerkova, E. Mihokova, M. Nikl, Z. Zhou, G. Ren and Y. Wu, ACS Applied Materials & Interfaces **13** (10), 12198-12202 (2021).
289. Z. Tan, J. Li, C. Zhang, Z. Li, Q. Hu, Z. Xiao, T. Kamiya, H. Hosono, G. Niu, E. Lifshitz, Y. Cheng and J. Tang, Adv. Funct. Mater. **28** (29), 1801131 (2018).
290. J. Li, Z. Tan, M. Hu, C. Chen, J. Luo, S. Li, L. Gao, Z. Xiao, G. Niu and J. Tang, Frontiers of Optoelectronics **12** (4), 352-364 (2019).
291. L.-T. Wang, Z.-Z. Ma, F. Zhang, M. Wang, X. Chen, D. Wu, Y.-T. Tian, X.-J. Li and Z.-F. Shi, Journal of Materials Chemistry C **9** (19), 6151-6159 (2021).
292. J. Huang, B. Su, E. Song, M. S. Molokeev and Z. Xia, Chem. Mater. **33** (12), 4382-4389 (2021).
293. J.-H. Wei, J.-F. Liao, L. Zhou, J.-B. Luo, X.-D. Wang and D.-B. Kuang, Sci Adv **7** (34), eabg3989 (2021).
294. Y. Jing, Y. Liu, X. Jiang, M. S. Molokeev, Z. Lin and Z. Xia, Chem. Mater. **32** (12), 5327-5334 (2020).
295. M. L. Lai, T. Y. S. Tay, A. Sadhanala, S. E. Dutton, G. Li, R. H. Friend and Z.-K. Tan, The Journal of Physical Chemistry Letters **7** (14), 2653-2658 (2016).
296. W.-L. Hong, Y.-C. Huang, C.-Y. Chang, Z.-C. Zhang, H.-R. Tsai, N.-Y. Chang and Y.-C. Chao, Adv. Mater. **28** (36), 8029-8036 (2016).
297. Y. Wang, R. Zou, J. Chang, Z. Fu, Y. Cao, L. Zhang, Y. Wei, D. Kong, W. Zou, K. Wen, N. Fan, N. Wang, W. Huang and J. Wang, The Journal of Physical Chemistry Letters **10** (3), 453-459 (2019).
298. X. Zhang, C. Wang, Y. Zhang, X. Zhang, S. Wang, M. Lu, H. Cui, S. V. Kershaw, W. W. Yu and A. L. Rogach, ACS Energy Letters **4** (1), 242-248 (2019).
299. L. Lanzetta, J. M. Marin-Beloqui, I. Sanchez-Molina, D. Ding and S. A. Haque, ACS Energy Letters **2** (7), 1662-1668 (2017).

300. Z. Wang, F. Wang, B. Zhao, S. Qu, T. Hayat, A. Alsaedi, L. Sui, K. Yuan, J. Zhang, Z. Wei and Z. a. Tan, The Journal of Physical Chemistry Letters **11** (3), 1120-1127 (2020).
301. L. Cheng, T. Jiang, Y. Cao, C. Yi, N. Wang, W. Huang and J. Wang, Adv. Mater. **32** (15), 1904163 (2020).
302. A. Singh, N.-C. Chiu, K. M. Boopathi, Y.-J. Lu, A. Mohapatra, G. Li, Y.-F. Chen, T.-F. Guo and C.-W. Chu, ACS Applied Materials & Interfaces **11** (38), 35088-35094 (2019).
303. J. Luo, X. Wang, S. Li, J. Liu, Y. Guo, G. Niu, L. Yao, Y. Fu, L. Gao, Q. Dong, C. Zhao, M. Leng, F. Ma, W. Liang, L. Wang, S. Jin, J. Han, L. Zhang, J. Etheridge, J. Wang, Y. Yan, E. H. Sargent and J. Tang, Nature **563** (7732), 541-545 (2018).
304. N. Liu, X. Zhao, M. Xia, G. Niu, Q. Guo, L. Gao and J. Tang, Journal of Semiconductors **41** (5), 052204 (2020).
305. Z. Ma, Z. Shi, C. Qin, M. Cui, D. Yang, X. Wang, L. Wang, X. Ji, X. Chen, J. Sun, D. Wu, Y. Zhang, X. J. Li, L. Zhang and C. Shan, ACS Nano **14** (4), 4475-4486 (2020).
306. S. Liu, Y. Yue, X. Zhang, C. Wang, G. Yang and D. Zhu, Journal of Materials Chemistry C **8** (25), 8374-8379 (2020).
307. Z. Ma, Z. Shi, D. Yang, Y. Li, F. Zhang, L. Wang, X. Chen, D. Wu, Y. Tian, Y. Zhang, L. Zhang, X. Li and C. Shan, Adv. Mater. **33** (2), 2001367 (2021).
308. S. Sun, N. T. P. Hartono, Z. D. Ren, F. Oviedo, A. M. Buscemi, M. Layurova, D. X. Chen, T. Ogunfunmi, J. Thapa, S. Ramasamy, C. Settens, B. L. DeCost, A. G. Kusne, Z. Liu, S. I. P. Tian, I. M. Peters, J.-P. Correa-Baena and T. Buonassisi, Joule **3** (6), 1437-1451 (2019).
309. X. Zhou, L. Zhang, Y. Huang, Z. Zhou, W. Xing, J. Zhang, F. Zhou, D. Zhang and F. Zhao, Advanced Optical Materials **9** (20), 2100889 (2021).
310. L. Wang, P. Yao, F. Wang, S. Li, Y. Chen, T. Xia, E. Guo, K. Wang, B. Zou and H. Guo, Adv Sci (Weinh) **7** (6), 1902900 (2020).
311. F. Jiang, X. Zhou, J. Lv, J. Chen, J. Chen, H. Kongcharoen, Y. Zhang and P. S. Lee, Adv. Mater. **34** (17), 2200042 (2022).